Modeling Focal Ratio Degradation, Its Implications for Upcoming Fiber Spectrographs, and the Dynamics of NGC 6822

Thesis by
Brent Roy Belland

In Partial Fulfillment of the Requirements for the
Degree of
Doctor of Philosophy

CALIFORNIA INSTITUTE OF TECHNOLOGY
Pasadena, California

2021
Defended May 20, 2021

Brent Roy Belland
ORCID: 0000-0003-1950-448X

ACKNOWLEDGEMENTS

In grad school, I have come to appreciate the importance of working together in getting major work done. I have seen firsthand some of how the international scientific collaboration made the Subaru Prime Focus Spectrograph come to life. But perhaps even more personally I have come to appreciate how much so many others added, enriched, and contributed to my time and work here. No matter what I try, I cannot do justice to just how much each of you helped me. These acknowledgments only serve as the tip of the iceberg when it comes to everyone who impacted me and the extent of what it means to me.

I want to give my biggest thanks to Evan Kirby and Mike Seiffert, who have had to deal with me the most of anyone during my time here. Both Evan and Mike were the most understanding mentors I could ask for. Conversations with Evan about NGC 6822 were always productive, never failing to uncover ideas on avenues to explore when I got stuck. Reviewing my FRD data with Mike likewise gave a new perspective that was vital in solving some of the biggest questions in my research. They were endlessly patient with me when work was particularly rough, and believed in me more than I sometimes believed in myself. Both Evan and Mike, I am so fortunate that I got to work with you.

I am also thankful for my other committee members Phil Hopkins, Andrew Howard and Chuck Steidel, for their guidance, support, and advice throughout my PhD studies. Their suggestions greatly improved the quality and thoroughness of my work.

I learned so much from the PFS lab at Caltech that it was one of the highlights of my time here. It was a pleasure working with Dan Reiley, whose experience-driven wisdom always shone through whenever I had a question in the lab. Discussions with Mitsuko Roberts always were enjoyable, from chats in Japanese to troubleshooting sessions my test Cobra fiber positioner. Without help from Antonio Cesar de Oliveira and Ligia Souza de Oliveira I do not think I truly would have grasped just how sensitive fibers are and how important focal ratio degradation is. Ligia's fervor for fibers also ignited a passion for my work in the lab, and for that I am very grateful.

I am additionally thankful for those who I worked with in the PFS collaboration. I especially am thankful for some of my Princeton colleagues who I worked closely with on FRD extraction for the 2D-Data Reduction Pipeline: Neven Caplar for

guidance and understanding the pipeline code, Robert Lupton for questions that always seemed to illuminate the heart of the matter, and Jim Gunn for advice that led me to much greater understanding of FRD.

I also want to thank those who supported me through challenging times. Sophia Leon, Ryan Patterson, Lee Coleman, Andrew, Sarah, and Cassandra, thank you so much for your patience with me through my time here. I could not have made it through grad school without your support.

I want to give a special shout-out to my friend Sam Moore, who consistently encouraged me to learn more about why, not just how, things work. Ever since I joined the PFS project to measure fiber FRD, I have thought about our open-ended experiment on measuring Berry phase in a single-mode optical fiber. Back then I did not realise how much more I would be working with fibers in the lab, but our experiment choice then helped give me the confidence to pursue my studies in this field now.

Leo Lin was a pillar of support for me during my time in Pasadena. He supported my research but also reminded me about the big picture, giving me perspective and opening my eyes to the larger community that matters. I'm very grateful for all of the time Leo invested in me, and I hope to pay it forward to others more in the future.

Finally, there is no way I would be where I am without my family. My mother Pam and father Kris have encouraged my studies and passions from the beginning, enabling me to get to this point. Matt, thanks for always showing a deep interest in my work even — and especially —when you didn't understand my explanations, pushing me to improve my own understanding. Mike, your compassion while listening to my venting and in sending me support when you knew I needed it most, was necessary for me to complete my work and my thesis. I'm so blessed you are here.

ABSTRACT

Spectroscopy is a cornerstone of astronomical research, enabling the measurements of abundances and velocities of astronomical objects. Fiber spectroscopy, with its capability to acquire spectra from targets in densely packed fields and position fibers over targets over a large field of view, promises to greatly expand the number of astronomical objects with acquired spectra. Upcoming such projects include the Subaru Prime Focus Spectrograph, which plans to advance cosmology, galactic archaeology, and galactic evolution studies.

However, with the introduction of fibers to the spectrographic optical path also comes the introduction of the issue of focal ratio degradation (FRD). FRD is the scattering of light traveling through a fiber due to effects such as imperfections in the core-clad interface of a fiber, end face preparation, and stresses imposed on the fibers; thus, FRD is inherent to any fiber-based instrument. FRD scatters light to larger angles, resulting in lost light at the spectrograph and redistribution of light in the light's point spread function at the spectrograph detector. These issues are compounded by the fact that each fiber has a unique FRD 'fingerprint' and stresses during telescope operation can vary and induce dynamically changing FRD. It is also difficult to measure precisely.

This thesis focuses on characterization of FRD. It introduces a novel approach to measuring that permits extraction of the effect of angular misalignment and tests this model on fiber mounted to a Cobra fiber positioner, though this method could be utilized for any optical fiber. The effects of FRD on the spectra are simulated and found to affect counts 3-4 pixels from the center of sky lines on the order of 1-2% for changes in FRD at the 3 milliradian level, highlighting the importance of a good understanding of FRD to model sky lines at the level desired for the Subaru prime focus spectrograph.

Multiplexed spectroscopy in NGC 6822 from KECK/DEIMOS is also presented. The ancient red giant population in NGC 6822 is prolately rotating, an unusual configuration that has been used as evidence of merger histories in other dwarf galaxies. The distribution of metallicity as a function of radius shows the oldest, most metal-poor stars are the most dispersion dominated. They also reside at larger radii, possibly pointing to a disruptive star formation history that scattered stars from the center of the galaxy over time. Future results from upcoming spectrographic surveys

such as the Subaru Prime Focus Spectrograph could illuminate what is driving these peculiar features in NGC 6822 among many other scientific discoveries.

PUBLISHED CONTENT AND CONTRIBUTIONS

Belland, Brent, Evan Kirby, et al. (Nov. 2020). "NGC 6822 as a Probe of Dwarf Galactic Evolution". In: *Astrophysical Journal* 903.1, 10, p. 10. DOI: 10.3847/1538-4357/abb5f4. arXiv: 2009.04555 [astro-ph.GA].
Belland participated in the conception of the project, analyzed the stellar kinematic data, and participated in the writing of the manuscript as its primary author.

Belland, Brent, James Gunn, et al. (Jan. 2019). "Focal Ratio Degradation for Fiber Positioner Operation in Astronomical Spectrographs". In: *Journal of Astronomical Instrumentation* 8.3, 1950007, p. 1950007. DOI: 10.1142/S2251171719500077. arXiv: 2006.10902 [astro-ph.IM].
Belland collected the data, analyzed the results to deduce the effect of FRD and angular misalignment in the data, and participated in the writing of the manuscript as its primary author.

TABLE OF CONTENTS

Acknowledgements . . . iii
Abstract . . . v
Published Content and Contributions . . . vii
Table of Contents . . . vii
List of Illustrations . . . ix
List of Tables . . . xvi
Chapter I: Introduction . . . 1
1.1 Spectroscopy . . . 1
1.2 Fibers and FRD . . . 2
1.3 Subaru PFS . . . 6
1.4 Galactic Archaeology . . . 7
1.5 Thesis outline . . . 9
Chapter II: Focal Ratio Degradation in the Prime Focus Spectrograph Fiber Positioner . . . 11
2.1 Introduction . . . 12
2.2 Model . . . 14
2.3 Hardware . . . 17
2.4 Stresses . . . 22
2.5 Angular misalignment . . . 26
2.6 Cobra FRD and Discussion . . . 28
Chapter III: Focal Ratio Degradation, the Point Spread Function, and their effect on sky subtraction in fiber-fed astronomical spectrographs . . . 33
3.1 Introduction . . . 34
3.2 FRD's effect on PSF . . . 36
3.3 Extraction of FRD from PSFs . . . 43
3.4 Conclusion . . . 45
Chapter IV: NGC 6822 as a probe of dwarf galactic evolution . . . 47
4.1 Introduction . . . 48
4.2 Data . . . 50
4.3 Results . . . 52
4.4 Discussion . . . 56
4.5 Summary . . . 62
Acknowledgements . . . 68
Chapter V: Conclusions and Future Work . . . 70
Bibliography . . . 72

LIST OF ILLUSTRATIONS

Number *Page*

2.1 Simulated effect of FRD on a uniform tophat profile. Above, the radial profile of the image when input and output from the fiber is shown. Below is a two dimensional image that demonstrates the effect FRD has on the point spread function has on FRD. Notably, an instrument that could only accept up to the initial tophat would lose throughput due to the FRD-induced increased profile size. Even if the instrument can accept faster inputs, increasing FRD causes increasing illumination of the outer parts of the pupil, which for the fast spectrograph cameras in all the projects discussed in the introduction brings increasing aberrations and degradation of the point spread function. 13

2.2 Dropoff in pixel intensity for the angular misalignment model with uniform input beam of f number 2.8 (numerical aperture of 0.1785). The effect on the profile for the same net width σ_{TOT} = 8.9 mrad are shown for varying angular misalignments, which corresponds to a different gaussian contribution from FRD (large angles are shown to emphasize the effect of angular misalignment). Also shown is the f number of 2.5 corresponding to the spectroscope cutoff. The light lost at the cutoff varies at a given σ_{TOT} for different angular misalignments. 17

2.3 Simple example of an ellipse profile (left) that to first order approximates a tilted circle. A figure demonstrating what a 2D profile with the rotationally averaged profile is shown in the middle panel, with its 1D profile from the center shown on the right. Notably, the dropoff in the 1D profile does not appear to behave like an error function; instead, it is similar to an image convolved with a ring. This suggests how our model could be related to Gloge's power distribution model. 17

2.4 Picture of the main camera and illuminator setup of the experiment, with fiber extending off the right side of the image. Components of the illuminator and camera setup are labeled. 19

2.5 Cutout schematic view from above of the apparatus used in the experiment, with blue rays outlining the optical path through the system. The illuminator is at the top of the figure consisting of the LED through the field lens, while the camera is at the bottom with the achromat and sensor. The fiber in a Cobra fiber positioner was also fitted with a microlens to map a f/2.2 beam to an f/2.8 beam. The illuminator and camera were mounted securely to an optical breadboard and the camera was covered with a shroud during measurement. . . . 20

2.6 Example data analysis image output from 2D image (left) scaled according to counts at the camera to radial profile extracted from the fitted center. The darker spots visible in the image were dust particles and are not intrinsic to the profile, though radially averaging minimizes the effect this has on the data. 21

2.7 A zoomed-in image of the radial profile around the region of interest, the dropoff. A model normal error function calculated from the difference between the 85% and 15% brightness levels (dashed lines) is in good agreement with the observed profile. The width, as indicated in the figure, can be extracted and is proportional to σ_{TOT}. 22

2.8 Measurement with the fiber replaced by a pinhole. This measurement represents the instrumental limit for the low FRD condition. The correlated speckles in the 2D profile are likely due to fabrication variations across the surface of the diffuser. The width of the dropoff in the radial profile is much lower than the dropoff measured from fibers; the nonzero width may indicate a systematic—though small—overestimation of FRD. 23

2.9 FRD as a function of bend curvature, with fiber bent as shown in the inset. No observable change in FRD occurred until a bend radius of 1.3 cm. 24

2.10 Variation of FRD with applied radial pressure to the fiber buffer. FRD appears to grow roughly linearly with applied buffer pressure, although extrapolation to lower pressures may not be accurate. Scatter also increases with applied weight, indicating how small variations in pressure distribution can significantly affect FRD measurements as weight increases. Error bars in this figure indicate the standard deviation of all measurements at a given pressure. 26

2.11 Variation of FRD with geometric angular misalignment from fitted minimum for two fibers. The effect is approximately hyperbolic, fitted for σ_{FRD} (see Section 2.5) and an x-axis offset. The bottom panel shows the residuals, which are subtracted from the fit. The minimum σ_{TOT}, roughly corresponding to the σ_{FRD} of each fiber, varies between the two but is within expected variation. While the fit is good for just effectively fitting to a minimum, there appears to be a nontrivial residual for the fiber of larger σ_{FRD}. 27

2.12 Angular misalignment between the geometric misalignment and the algorithmically calculated misalignment, with errors calculated from σ_{TOT} and the range of angular misalignment with sum of least squares within 5% of the minimum fit. Agreement between the angles is low at lower angular misalignments, possibly due to nonuniform profile effects that dominate misalignment effects for low misalignment, but is good at large angles. This result indicates that the misalignment extraction from the model is reasonable. 28

2.13 Schematic cutaway of a Cobra fiber positioner, with various parts and parameters marked. Figure from the Subaru PFS collaboration's Cobra Fiber Positioner Manufacturing Readiness Review. Also see Fisher et al. (2014) for a Cobra figure and more discussion of the Cobra. 29

2.14 Profile σ_{TOT} of a fiber with microlens throughout the range of motion in both stages of the Cobra positioner. There is a significant variation of σ_{TOT} through stage 1 (θ stage) and stage 2 (ϕ stage) motion. The sinusoidal behaviour across stage 1 indicates an angular misalignment effect. Uncertainties of about ±50 steps in stage 1, corresponding to ±5° angular precision, were also present though not depicted in this figure. 30

2.15 Angular misalignment as calculated from the power distribution model in this paper (section 2.2). The sinusoidal behavior across stage 1 suggests that the σ_{TOT} variation in stage 1 is indeed due to angular misalignment rather than stress, and angular misalignment due to the ϕ stage is also apparent. 31

2.16 FRD extracted from the fiber profiles after considering angular misalignment. The FRD can be well-characterized in a single experimental setup across varying configurations due to this angular misalignment extraction, and is consistent with minimal stress on the fiber during Cobra operation. 32

3.1 Simulated PFS spectrum for an star with $i = 18AB$ (Lupton, 2021). The total spectrum is shaded in blue. The portion attributable to sky emission is shaded in blue. In the 1000-1200 nm range, the number and strength of sky lines are very large relative to the target spectrum. Even a fraction of a percent error in the modeling of these lines would significantly affect the final sky-subtracted spectrum. 36

3.2 Left: Simulated value of a pupil image from a fiber at the center of the spectrograph. The pupil is obscured by the spectrograph detector and the "spider" that supports it. Right: The in-focus PSF simulated from the pupil image on the left. This pupil image can be used to easily identify FRD variations while PSFs from the 2D-DRP allow for FRD's effect on spectra to be better understood. 38

3.3 This figure demonstrates the pupil image of input light in the left column, the central 20×20 pixels of the in-focus image in the top of the right column, and 2d residuals between in-focus images at adjacent rows' FRD values in the rest of the right column in steps of 6 mrad. The residuals display how increasing FRD adjusts the PSF in the spectrograph, with a maximum fractional change of 9% a few pixels from the center at the 6-12 mrad FRD transition. The dipole-like residuals indicate a possible centroid shift. 39

3.4 Residual generated by subtracting the in-focus spectrograph image from the center of the spectrograph with 6mrad FRD by the same image except offset by one pixel vertically. The residual output generates a dipole structure similar to that as seen in Figure 3.3 . . . 40

3.5 This figure demonstrates the same data as Figure 3.3 except that each image is aligned to have the same centroid. The residuals display how increasing FRD adjusts the PSF in the spectrograph, on the order of 100 counts in a pixel. More notably, aligning centroids also removes the dipole-like structure of the residuals, though the low-FRD residuals are complex regardless. High-FRD residuals tend to be simpler with a decrease in flux at the center of the PSF and increase in flux toward the wings. 41

3.6 Result of a 1D boxcar extraction in the wavelength direction of an example 2D PSF (solid black line) and residuals when FRD is changed (colored solid lines). Numbers along the bottom of the image indicate the counts in the residual between 21 mrad and 24 mrad FRD (yellow) and corresponding percent variation in that pixel from the full boxcar extraction of the lower FRD spectrum (21 mrad). Additionally, noise level for Poisson noise (black) and read noise (cyan) are shown in dash-dotted lines. Read noise assumes the value of the read noise and scattered light (variance of 40 $counts^2$) measured from test LAM data. This measurement is an upper limit for each spatial pixel. . . . 42

3.7 Example chi squared per pixel value calculated from the FRD residual minimization algorithm in its current state as a function of the "guess FRD" input into the algorithm (input FRD of 0.023 radians). The dotted horizontal blue line is the minimum chi square in the solution plus one. 44

3.8 Uncertainty in FRD extraction at varying locations (and thus varying wavefronts) across the detector. Uncertainties grow largest towards the edges of the detector but approach 2 mrad toward the center. . . . 45

4.1 Distribution of stars (orange) from Kirby, Cohen, et al. (2013) in color–magnitude space plotted with photometry (blue) from Massey, Olsen, et al. (2007). 51

4.2 Distribution of stars from Kirby, Cohen, et al. (2013), color-coded by heliocentric velocity, with dark blue corresponding to least rapidly approaching and light yellow corresponding to most rapidly approaching. The dotted black line indicates an approximate position angle of the major axis of RGB stars estimated from the RGB isophotes in Figure 8 of Cannon et al. (2012) (18 degrees), while the green line indicates the approximate position angle of the major axis of H Idisk from Weldrake, de Blok, and Walter (2003) (110 degrees). The velocity gradient apparent from west to east indicates rotation, prolate in the sense of the RGB stars and oblate in the sense of the H Idisk. Coordinates are in units of arcmin relative to the center of NGC 6822 (McConnachie, 2012). The angular size of 1 kpc is shown in the bottom left for reference; NGC 6822 extends 5 kpc in either direction along the H Imajor axis and about 1 kpc in either direction along the RGB isophote major axis. 53

4.3 Metallicity versus rotation support (rotational velocity divided by velocity dispersion) for stars in NGC 6822 separated into five equal-number bins. The errors bars represent 68% confidence intervals. The upward trend in rotation support with metallicity indicates that younger stars are more rotationally supported in NGC 6822. This information is included in the summary of Table 4.1. 57

4.4 Top: Rotation velocity vs. metallicity. Bottom: Velocity dispersion vs. metallicity. Taken together, the rotation velocity and velocity dispersion are the components of Figure 4.3. The velocity dispersion change is more significant than the rotation velocity. The errors bars represent 68% confidence intervals. The upward trend in rotation support with metallicity indicates that more metal-rich, presumably younger stars are more rotationally supported in NGC 6822. This information is included in the summary of Table 4.1. 63

4.5 Kinetic energy in dispersion per unit mass of stars in each metallicity bin. The kinetic energy trends in the same way as the dispersion (see Figure 4.4) because dispersion dominates over rotation. The variable n quantifies uncertainty in anisotropy (see text). Notably, kinetic energy is not constant with metallicity. This information is included in the summary of Table 4.1. 64

4.6 Top: Approximate velocity versus radius from the B24 minimum disk model of Weldrake, de Blok, and Walter (2003). The dotted orange line indicates the radial limit of the Weldrake, de Blok, and Walter (2003) data, with an extension from the pseudo-isothermal model in velocity beyond this value. Bottom: Conversion to enclosed mass divided by radius as a function of radius (i.e., Equation 4.3 where $\sigma_k = 0$). 65

4.7 Radius vs. Metallicity, combining the enclosed mass vs. metallicity relation (Figure 4.5) with the velocity data of Weldrake, de Blok, and Walter (2003, Fig. 4.6), assuming the stellar dispersion is purely radial. Note that this is not the same as the metallicity gradient (see text). This information is included in the summary of Table 4.1. . . . 66

4.8 Same as figure 4.7 except assuming the stellar dispersion is isotropic. The decreasing velocity curve in H Iindicates much further radial distances for metal-poor populations in this case. This information is included in the summary of Table 4.1. 67

LIST OF TABLES

Number *Page*

4.1 Table summarizing the stellar binned data in Figures 4.3, 4.4, 4.5, 4.7, and 4.8. 69

Chapter 1

INTRODUCTION

1.1 Spectroscopy

Spectroscopy is fundamental to astronomy. All astronomical spectrographs operate under the same principles as the first experimentation with spectroscopy by Newton: take a focused, directed source of light and pass it through a disperser to split it into its component wavelengths, and analyze the result (Massey and Hanson, 2013). Typically, light is focused through a slit and collimated, passed through a dispersion grating (rather than a prism, as Newton used), and imaged on a camera.

Fraunhofer (1817) connected spectroscopy to astronomy by identifying specific, replicable lines in the solar spectrum, pointing to something fundamental about the Sun. Bunsen and Kirchhoff (1863) determined that Fraunhofer's absorbed lines of light matched known chemical spectral signatures, like sodium, from laboratory testing on Earth, pointing to elements in the Sun's atmosphere absorbing its light. The power of spectroscopy to determine chemical compositions of stars far away in astronomical analysis was made abundantly clear. Combined with the Doppler shift that moved the wavelengths of these known elemental spectral lines based on the relative velocity of the star and observer, spectroscopy opened up kinematic and compositional dimensions to astronomical study. This information is vital to modern astronomical research; we would not have learned about dark matter (Zwicky, 1933; Rubin and Ford, 1970), the expansion of the universe (E. Hubble, 1929) or the acceleration of the universe (Perlmutter et al., 1999; Schmidt et al., 1998).

Many new technologies are being developed and enhanced to advance the field. The most obvious improvement is the increase in the largest telescopes' sizes, which have grown over an order of magnitude from Mount Wilson's record-setting 2.5 meter aperture in 1918 (Racine, 2004). Larger aperture allows for more light collection, which allows for fainter, older objects to be studied with more signal-to-noise. Detector technology has progressed to CCDs that continue to have their quantum efficiencies, read noise, wavelength ranges, and sizes optimized for astronomical research (Lesser, 2015), allowing for larger field-of-view and depth that can be studied with these instruments.

However, improvements in spectroscopy have been driven mostly by conceptual,

rather than technological, advancements. While many early spectrographs used a slit to collect light from an object of interest, slits are not strictly required for a spectrograph. While slits confer many advantages in spectroscopy, there are some drawbacks as well. Slits cannot be arbitrarily close to each other, since each image of the slit is split up along the dispersion axis of the detector. If multiple slits were placed along the direction of light dispersion, their spectra would overlap, complicating spectral extraction. In order to avoid this, in practice the number and orientation of slits are restricted. Nonetheless, astronomical objects of interest can be closely packed together on the sky, making slit-based spectroscopy less efficient. Instead, if a point-sized slit were positioned at each desired target, no matter how densely packed in the field, and the light were rearranged at the detector to not overlap other spectra, more spectra in crowded fields could be taken in one measurement resulting in more efficient observations. Fibers allow for such a mode of operation. Furthermore, fibers can be used to select targets over larger fields-of-view, since only the light from each fiber needs to be projected onto the spectrograph detector rather than potentially the whole field with most of the light masked out by the slits. Fibers even mix light, which reduces angular/spatial variation in the spectral light projected in the detector, thereby mitigating systematic errors in the spectra. Combined with the improvements in fiber and detector technology, the advantages of higher multiplex and larger field-of-view motivated development of fiber-fed astronomical spectrographs (Hill, 1988).

1.2 Fibers and FRD

However, just as slits have drawbacks relative to fibers, fibers have their own drawbacks relative to slits. While fibers act as point-size slits on targets of interest, light must travel through the length of the fiber. Unlike a slit, fibers are not perfectly lossless. Introducing fibers to the optical path can diminish the quality of spectra in two ways. First, it can cause light loss, ultimately reducing the signal-to-noise ratio of the spectrum. Second, it can alter the point spread function, which can reduce the effectiveness of sky subtraction. This section will review how this occurs in fibers, as well as how it is quantified and addressed.

Every component of a fiber introduces some potential source of loss. Rough end faces where the light enters or exit the fiber may cause scattering of light and decreased efficiency. “Macro” bends in a fiber in its routing from its input (such as the focal plane of a telescope) to its output (such as the spectrograph’s camera) can shift the angle of incidence of light at the core/clad boundary, causing scattering.

Small physical imperfections in the core/clad interface due to manufacturing can introduce a similar effect known as "microbending," causing scattering of light in a fiber and light loss. Stresses on a fiber likewise can deform a core/clad interface resulting in light dispersing. While modern fibers have high efficiencies, there will always be some amount of this scatter inherent in the fiber.

Over the length of a significantly long fiber the input light is azimuthally well-mixed, but radially it is scattered due to those many effects such as end face preparation, microbends, and stresses. The accumulation of all of these effects is called focal ratio degradation (FRD), as the scattering of light from these effects causes the focal ratio of light to decrease. Each fiber in a fiber spectrograph has a unique "fingerprint" on the light traveling through it due to their different physical characteristics and thus have unique FRD. FRD behaves as a convolution on the input light, and should be well understood to correct for the effects fibers introduce to the optical path of any fiber spectrograph.

Because FRD can reduce spectral quality, it is important to attempt to mitigate it or at least to quantify its effect on the final spectrum. This is the focus of a major portion of this thesis. Before discussing that work, it is important to understand the basic theory of FRD.

Basic mathematical model of FRD

This subsection is adapted from Belland et al. (2019).

FRD manifests as a convolution of the fiber input that results in the fiber output. While many contributions to FRD exist, modal diffusion due to imperfect fiber core/clad interfaces or changes in core index can dominate FRD, and this contribution manifests itself as a Gaussian blurring of the input with size σ.

To verify the initial premise of this model, namely that scattering from FRD can be quantified with a value for σ, previous work on FRD must be considered. FRD due to scattering of light causing light coupling to higher modes within the fiber has been analyzed by Gloge (1972), who developed a model to describe the power distribution P of light from a fiber of length L due to microbending, as a function of light's angle from normal incidence θ:

$$\frac{\partial P}{\partial L} = -A\theta^2 P + \frac{D}{\theta}\frac{\partial}{\partial \theta}\left(\theta \frac{\partial P}{\partial \theta}\right) \tag{1.1}$$

with A and D corresponding to absorption and coupling coefficients respectively.

The $-A\theta^2 P$ term describes how light is absorbed or otherwise lost due to properties of the fiber, whereas the $\frac{D}{\theta}\frac{\partial}{\partial\theta}\left(\theta\frac{\partial P}{\partial\theta}\right)$ term describes how light traveling down one mode of the fiber may diffuse to adjacent modes, which physically manifests itself as a redistribution of light to different angles — FRD.

This power distribution PDE was solved by Gambling, Payne, and Matsumura (1975) for a plane wave input to the fiber at an angle of incidence θ_i:

$$P(\theta) \simeq \frac{1}{bL}\exp\left(-\frac{\theta^2+\theta_i^2}{4DL}\right) I_0\left(\frac{\theta\theta_i}{2DL}\right) \tag{1.2}$$

for $b = 4\sqrt{AD}$ and I_0 representing a Bessel function of zeroth order, for $bL \ll 1$. Notably, this expression asymptotically approaches Gaussian behavior in the limits $(\frac{\theta\theta_i}{2DL}) \ll 1$ and $(\frac{\theta\theta_i}{2DL}) \gg 1$, both with standard deviation

$$\sigma = \sqrt{2DL}. \tag{1.3}$$

Relevant to Chapter 2 of the thesis, we can relate the results of Gambling, Payne, and Matsumura (1975) to the cone test of FRD, where the fiber input is light that is uniformly angularly distributed up to some angle θ_i. Due to the simple nature of the plane wave, it is possible to integrate to create an input profile for a cone of light; integrating over an input profile $G(\theta, \theta_i)$ yields an output power F of

$$F(\theta) = \int_0^{2\pi}\int_0^{\pi} G(\theta', \phi')P(\theta, \theta')\sin(\theta')d\theta' d\phi'. \tag{1.4}$$

Assuming a uniform cone-like beam with rotational symmetry about the fiber axis, the overall output power F from the fiber then becomes

$$F(\theta) \propto 2\pi\int_0^{\theta_i} P(\theta, \theta')\sin(\theta')d\theta'. \tag{1.5}$$

This integral approximates a normal error function with the same σ as the one corresponding to that of the ring test.

Thus, the FRD model aligns well with a σ_{FRD} characterizing its output, just as utilized in this model.

History of FRD in spectrographs

Characterization of FRD is often concerned with loss minimization in older spectrographs. Angel et al. (1977), in one of the first papers advocating for fiber use in

astronomical spectrographs, heuristically estimated FRD and measured FRD in test fibers to quantify this light loss. They found an estimated 15% of the input light would be scattered outside their spectrograph's acceptance angle due to FRD in their instrument design. However, especially at that time, this loss was low enough to consider fiber spectroscopy feasible. The first astronomical fiber spectrograph, MEDUSA (Hill et al., 1980) was motivated in part by these results in development. Despite its larger FRD resulting in up to 40% losses, MEDUSA encouraged future developments in the field. The large FRD in MEDUSA was due to some "unsophisticated" material preparations (such as fiber end face polishing) and not inherent to fiber spectroscopy. While FRD was a major consideration for the earliest fiber spectrographs, even modern spectrographs must plan around this light loss caused by FRD. For just one example C. Poppett et al. (2018) highlighted the importance of FRD in the Dark Energy Spectroscopic Instrument's (DESI's) fiber system, where the average light transmission after FRD must be at least 90% and each individual fiber's light transmission after FRD must be at least 80% to meet their system specifications.

Now, in a push to maximize the scientific output of new instruments, understanding FRD has taken on new importance. FRD does not only scatter light outside of the acceptance angle for the spectrograph but also redistributes the light angularly. While in principle all light is focused to one point which should remove the angular dependence in the spectrograph camera, in practice varying wavefronts and imperfect optics can result in more complicated effects on the light at the detector. The effect of FRD on the point spread function in the detector is considered in more detail in Chapter 3. Furthermore, simply accommodating for FRD by making a spectrograph accept a faster input can introduce systematic errors in spectra. Barden (1998) noted in fiber testing that decreasing the focal ratio of a spectrograph would reduce light loss from FRD but also decrease the radial mixing of the light from the fibers. Hunter and Lawrence W. Ramsey (1992) argue that incomplete radial mixing results in time-varying shifts on the image in the detector, resulting in radial velocity errors that can affect the precision of spectrographs. FRD can result in redistribution of light that manifests itself systematically in spectra, which must be corrected for in order to maximize the science these instruments can complete.

Despite the importance of FRD, measurements are notably nonstandardized. Beyond two separate measurements in the form of cone and ring tests, the parameters used to measure FRD vary from normalized throughput (enclosed energy) (e.g., Oliveira,

de Oliveira, and dos Santos, 2005) to increase in focal ratio for a given amount of illumination (e.g., Barden, 1998), to the D dispersion coefficient in the Gloge model (Hayne et al.) or the width of the illumination drop-off (e.g., Belland et al., 2019, which is the formulation used in this thesis). In part, this is due to varying project requirements; some projects utilize multiple separate quantities such as Claire L. Poppett et al. (e.g., 2014) who use full-width half-maximum from the ring test, enclosed energy from the cone test, and near field 2D imaging to address requirements from DESI specifications, geometric and stress variations in transmittance due to FRD, and FRD effects that manifest in detector point spread function variations respectively. The variance in FRD quantification parameters makes comparisons between measurements from different projects particularly challenging.

While this subsection focuses on the potential challenges that fibers introduce in spectroscopy, due in no small part to FRD, methods including those discussed in this thesis can mitigate these drawbacks.

1.3 Subaru PFS

Fiber-fed multi-object spectroscopy has experienced a boom in in-development projects within the last few years, with the upcoming Subaru Prime Focus Spectrograph (PFS) (Sugai et al., 2015), DESI (Flaugher and Bebek, 2014), MOONS (Cirasuolo et al., 2011), 4MOST (de Jong et al., 2012), and WEAVE (Dalton et al., 2012) being among the new projects either going on-sky or finishing development. DESI promises to push forward cosmology using spectra of stars over 11 billion light years to map out the expansion history of the universe. MOONS can leverage the large 8.2 meter aperture of the Very Large Telescope and near infrared spectral coverage to reach the spectral lines needed to analyze the evolutionary history of $z \sim 1$ galaxies. 4MOST promises to follow up on the the higher magnitude targets of Gaia and eROSITA to give more complete information about astronomical objects with precise astrometic distances and X-ray targets of interest. WEAVE can utilize its integral field unit capabilities to follow up on H I measurements of Apertif in addition to follow up on Gaia and radio LOFAR measurements.

In particular focus in this thesis, the upcoming Subaru PFS is a promising next-generation fiber-fed multi-object spectrograph. Similarly to MOONS, PFS boasts a large 8.2 meter aperture telescope, enabling faster observations and fainter-object spectroscopy from the higher photon collecting capabilities of these larger telescopes. Unlike MOONS, however, PFS can take more advantage of the Subaru

Telescope's large field of view —over 1.3 square degrees, nearly ten times the field-of-view of MOONS's telescope's, VLT, which is approximately 0.14 square degrees. This larger field of view enables PFS to conduct large surveys of point sources over wide swaths of sky as well as target individual galaxies extended over larger areas of sky (e.g., M31 or NGC 6822).

The PFS has a strong complement with the Subaru telescope's complementary imager Hyper Suprime-Cam (HSC) (Miyazaki et al., 2012), which serves as an upgrade to the Subaru Telescope's previous imager Suprime-Cam with a 1.5 square degree field of view and high resolution with 0.168 arcsecond pixel scale. HSC is undergoing a survey of 1400 square degrees over the sky up to magnitude 26 and two separate deeper surveys of 26 and 3.5 square degrees up to 27th and 28th magnitude respectively. The complementarity between the photometry of HSC and spectroscopy of PFS already allows for detailed target selection for follow-up, which many fiber-fed spectrographs aim to capitalize on with various instruments. For example, WEAVE and 4MOST plan to follow up on Gaia photometry. But uniquely for the PFS, both HSC and PFS are made for the same telescope, so instrumental effects between HSC and PFS observations should be similar and reduce errors in correlating data from each instrument.

Combining the strengths of the Subaru Telescope, HSC, and the instrument design of the PFS, there are three primary science pillars for the survey: galactic archaeology, galactic evolution, and cosmology. This thesis will focus on the galactic archaeology component of the PFS's survey plan.

1.4 Galactic Archaeology

Galactic archaeology is the science of reconstructing a galaxy's past formation and evolution history using its current-day kinematics and composition — a field that greatly depends on spectroscopy to gather the necessary data. Galactic archaeology aims to understand how galaxies evolved to their current form and to address the gaps between theoretical predictions and observed realities of galaxy formation. For instance, cosmological simulations of dark matter predict that galaxies should form with a steep power law in their density distribution ("cuspy") (Navarro, Frenk, and White, 1997), but dwarf galaxies were observed with less steep distributions at their centers ("cored"). Galactic archaeology offers a method to bridge the gap between simulations and our cosmic neighborhood.

Abundance information can be used to learn about the history of a galaxy over

time. Starting from an overwhelmingly hydrogen- and helium-dominated universe (Burbidge et al., 1957), stars have synthesized heavier elements ("metals") during their lifetimes. These chemicals are ejected into the intergalactic medium with even heavier elements formed in massive stars' supernovae. This material enriches the environment that new stars form in, increasing the metallicity of future generations of stars, and the process repeats. Thus, the abundances elements in a star contain a history of its progenitors, with the most metal-poor stars originating in earlier generations of star formation. More substantial analysis can be done when comparing these abundances to models of stellar formation in a galaxy to determine if the resulting chemical distribution in the galaxy matches the model. Kirby, Lanfranchi, et al. (2011) compared the metallicities of eight dwarf spheroidal galaxies against three distinct models of galactic evolution, finding that gas inflows made for models that better described the majority of the dwarfs studied and highlighted the importance of metallicity loss to gas outflows in the less massive galaxies of their sample.

In galactic archaeology, kinematic data are instructive because they enable us to map the potential of a galaxy, informing us about its structure. Kinemetics also let us theoretically "trace back" the stars to a formation origin to learn about their histories. The combination of kinematic and abundance data is even more powerful than either component alone. Walker and Peñarrubia (2011) were able to identify chemically and kinematically distinct subpopulations within Fornax that could independently serve as probes of the galaxy's gravitational potential. Unique to this work, the distribution of mass was extracted independent of any assumed dark matter distribution model, using the mass enclosed within the half-light radius of each subpopulation's orbit. This work revealed that the distribution of mass in Fornax is flatter toward its center than the standard cuspy dark matter profile (Navarro, Frenk, and White, 1997) would predict, raising questions about why these dark matter dominated galaxies deviate from their expected distribution.

Dwarf galaxies are a particularly informative class of galaxy to study. As small laboratories of galaxy formation, dwarfs serve as manageable populations to test formation models. But as dwarfs are the building blocks of more massive galaxies, information we learn about their formation histories also contributes to our understanding of how more massive galaxies evolved.

NGC 6822, also known as Barnard's Galaxy, is one such dwarf galaxy. Due to its large mass (relative to most other Local Group dwarf galaxies) and proximity to the

Milky Way, NGC 6822 was the first dwarf irregular galaxy beyond the Magellanic Clouds to be discovered. Cepheid variable stars in the galaxy contributed to it being one of the first galaxies determined to be outside of the Milky Way (E. Hubble, 1929). NGC 6822's size and large extent on the sky still makes it a promising target to study today. It is a target of the PFS's galactic archaeology survey, so PFS will illuminate more about NGC 6822's structure and dynamics through its efficient pointing. It is the only dwarf irregular galaxy in the PFS's galactic archaeology survey, so it will serve as a unique probe of dwarf galaxy evolution within the PFS's sample. Understanding this promising target is the focus of Chapter 4 of this thesis.

1.5 Thesis outline

The purpose of this thesis is to review FRD due to fiber positioning and the corresponding stresses, FRD's effect on the acquired spectra via sky subtraction, as well as consider an application of multi-object spectroscopy in the dwarf irregular galaxy NGC 6822.

In the second chapter of the thesis, FRD for a fiber in a fiber positioner is measured. Repositioning a fiber can bend it in a different way compared to its previous configuration, and moving a fiber may induce additional stresses on it. Thus, fiber positioning can affect the FRD of the fiber dynamically depending on fiber/target positioning. The purpose of this chapter is to reliably quantify FRD. Additionally, the method used to measure FRD is also able to distinguish the convolution effect of FRD due to the fiber from a effective modification to the input light due to angular misalignment between the light source and the fiber, permitting for a more convenient and robust FRD test.

The third chapter of this thesis aims to address the effect of FRD on the potential science of the Subaru PFS. Since many of the objects the PFS plans to study are much fainter than the sky, the bright sky lines due to chemicals such as OH in the atmosphere must be very accurately modeled. FRD redistributes the light from the sky and thus must be well understood to precisely subtract out the sky, especially to reach the 0.5% continuum sky subtraction goal for the PFS.

The fourth chapter of the thesis considers the dwarf irregular galaxy NGC 6822, which will be included in PFS's planned galactic archaeology survey. We utilize Keck/DEIMOS spectroscopy to gather velocity and abundance information for many ancient red giant branch stars in this galaxy. The evolution of velocity as a function of metallicity indicates a time-evolving dispersive effect driving the dynamics of

stars in this galaxy, and the project in this chapter is one of the countless possible projects enabled by spectroscopy that could be advanced further by the upcoming PFS.

The fifth chapter of the thesis reviews the main takeaways from each of the previous chapters and discusses how the PFS can benefit from the FRD modeling and how PFS could advance the dwarf galaxy study considered in chapter 4.

Chapter 2

FOCAL RATIO DEGRADATION IN THE PRIME FOCUS SPECTROGRAPH FIBER POSITIONER

Belland, Brent et al. (Jan. 2019). "Focal Ratio Degradation for Fiber Positioner Operation in Astronomical Spectrographs". In: *Journal of Astronomical Instrumentation* 8.3, 1950007, p. 1950007. DOI: 10.1142/S2251171719500077. arXiv: 2006.10902 [astro-ph.IM].

Abstract

Focal ratio degradation (FRD), the decrease of light's focal ratio between the input into an optical fiber and the output, is important to characterize for astronomical spectrographs due to its effects on throughput and the point spread function. However, while FRD is a function of many fiber properties such as stresses, microbending, and surface imperfections, angular misalignments between the incoming light and the face of the fiber also affect the light profile and complicate this measurement. A compact experimental setup and a model separating FRD from angular misalignment was applied to a fiber subjected to varying stresses or angular misalignments to determine the magnitude of these effects. The FRD was then determined for a fiber in a fiber positioner that will be used in the Subaru Prime Focus Spectrograph (PFS). The analysis we carried out for the PFS positioner suggests that effects of angular misalignment dominate and no significant FRD increase due to stress should occur.

2.1 Introduction

Optical fibers serve an important role in modern astronomical instrumentation. They are a key element in a number of current multi-object spectrographs (e.g., Smee et al. (2013) and Lewis et al. (2002)), where they relay light from astronomical objects at the telescope focal surface to a remotely located spectrograph. Optical fibers will find continued use in essentially all next-generation massively-multiplexed astronomical spectrographs. Projects under development include the Subaru Prime Focus Spectrograph (PFS) (Sugai et al., 2015), DESI (Flaugher and Bebek, 2014), MOONS (Cirasuolo et al., 2011), 4MOST (de Jong et al., 2012), and WEAVE (Dalton et al., 2012), among others. This paper is motivated by focal ratio degradation (FRD) testing for the Subaru PFS, utilizing the same fiber and fiber positioning system that will be used in the PFS.

FRD is the decrease of the focal ratio of a beam traversing a fiber (L. W. Ramsey, 1988). The light power distribution thus varies due to FRD after transmission through a fiber, causing issues for subtracting night sky lines in fiber-fed spectrographs in astronomical implementations (Clayton, 1989; Bolton and Schlegel, 2010). These issues must be addressed in order to limit the sky subtraction residuals to less than 0.5% of the sky continuum, as is the goal for the PFS (Tamura et al., 2016). The FRD of the fiber is a function of many components, potentially varying as the fiber experiences different stresses during positioning and telescope operation. FRD in the PFS has a dynamically changing effect on the point spread function, as will be discussed below. Furthermore, FRD can cause a decrease in throughput if it causes some light to scatter to a focal ratio that is smaller than the acceptance focal ratio of the spectrograph. An example of how FRD can affect a beam is demonstrated schematically in Figure 2.1.

The causes of FRD include any effect that can scatter the light, including polishing irregularities at the fiber surface, microbending introducing irregularities to the core/clad interface, diffraction, bending, twisting, and squeezing among other causes (Clayton, 1989; Oliveira, de Oliveira, and dos Santos, 2005). It should therefore be minimized to diminish the throughput loss and quantified to understand its effect on the light's point spread function.

However, the key to precise atmospheric background subtraction for PFS is the accurate modeling of the point spread function, not just knowledge of the FRD. This in turn requires an accurate model of the intensity as a function of angle when light exits the fiber and enters the spectrograph. In particular, any change with

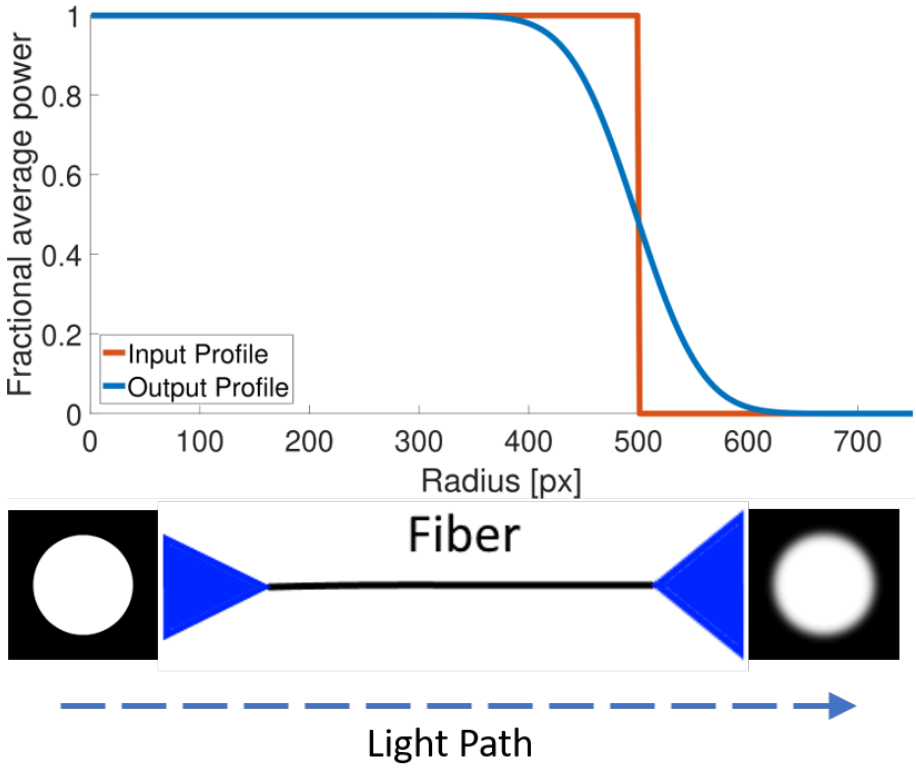

Figure 2.1 Simulated effect of FRD on a uniform tophat profile. Above, the radial profile of the image when input and output from the fiber is shown. Below is a two dimensional image that demonstrates the effect FRD has on the point spread function has on FRD. Notably, an instrument that could only accept up to the initial tophat would lose throughput due to the FRD-induced increased profile size. Even if the instrument can accept faster inputs, increasing FRD causes increasing illumination of the outer parts of the pupil, which for the fast spectrograph cameras in all the projects discussed in the introduction brings increasing aberrations and degradation of the point spread function.

the instrument configuration, such as the position in the focal plane or the position of individual fibers within their patrol region that affects the PSF will need to be determined. With this in mind, we conducted a series of experiments to evaluate changes in FRD in a fiber due specifically to its fiber positioning hardware which we call a Cobra. For these purposes, we wish to know not only the net effect, but also the components due to applied fiber stress (that is, the bending and twisting inside the Cobra due to its motion), angular misalignments (both static and dynamic). The repeatability and predictability of the FRD is also of foremost importance.

There are two primary methods to measure FRD: a cone test, also known as a solid angle test, and a ring test, also known as a collimated beam test (Haynes et al.,

2011; Yan et al., 2018). The cone test involves a uniform beam of known solid angle that fills a fiber. The output profile is measured and typically the enclosed energy at varying f-ratios is found (Oliveira, de Oliveira, and dos Santos, 2005; dos Santos et al., 2014); relative enclosed energies are compared to determine FRD. The cone test is able to probe the whole input cone of the fiber, but it is sensitive to misalignments. In contrast, the ring test involves a beam input at a known angle into a fiber, quantifying FRD by the FWHM of the resulting ring output (J. Allington-Smith et al., 2013; Finstad et al., 2016). While ring FRD can be quantified by its angular size, it is restricted to a small range about the input f number and characterize the light power distribution over the entire fiber outside of this range. Comparison of results between these two tests is complicated by the fact that the measurement outputs are different.

In this paper, a method of determining absolute FRD from the cone test is proposed. Such a system would be able to probe the whole input range of a measured fiber, being sensitive to input profile variations in a single test, while still quantifying the FRD in a way comparable to the ring test. In particular, the misalignment component of the cone profile can be extracted, yielding both fiber FRD and angular misalignment at the same time.

This paper is structured to discuss the FRD extraction model considered here in Section 2.2 and then hardware setup in Section 2.3. Afterward, various forms of stress (bending, squeezing, and twisting), and thus potentially of FRD, are measured in a Polymicro fiber in Section 2.4, and angular misalignment in a fiber is interpreted using the cone test in Section 2.5 to compare to the angular component of the model. Finally, each of these components is considered in the fiber positioning system, the Cobra, which will be used in the Subaru PFS, to determine the relative magnitude and contributions of stress vs. angle in Section 2.6.

2.2 Model

FRD is the effective smearing of light due to imperfections of the fiber core/clad interface from fabrication and from stresses such as from bending, as well as from fiber end face preparation. Assuming these defects are scatterers of a random angle and over the length of the fiber many such defects are encountered, by the Central Limit Theorem, the angle scattered should roughly be describable by a Gaussian distribution with standard deviation σ. In practice, Haynes et al. (2011) found using the ring test that modal diffusion due to effects such as microbending behaved in a

Gaussian way, aperture diffraction could be approximated as a Gaussian, and end face surface roughness could be modeled by a Gaussian or Lorentzian profile with Lorentzian component decreasing with smoother fiber surface. In this paper, the Gaussian effects are assumed to dominate FRD.

To first order we wish to characterize FRD by the σ of a Gaussian that, when convolved with a tophat input light distribution, yields the observed output profile. (Justification of this Gaussian model is provided in Chapter 1 of this thesis.) Without any other outside influences, this σ would characterize FRD, but angular misalignments can confound this analysis. Let the σ value due to FRD be σ_{FRD} whereas σ_{TOT} will be used to characterize the σ that would create an equivalent width of the entire dropoff of power over angle. We can find σ_{TOT} directly from analyzing a fiber's output profile, but σ_{FRD} can also be extracted due to the different effects FRD and angular misalignment have on the profile. In the case of no angular misalignment, $\sigma_{TOT} = \sigma_{FRD}$.

However, in general, there is more than FRD affecting the profile; $\sigma_{TOT} > \sigma_{FRD}$ due to angular misalignments. If the chief ray is not normal to the fiber face, a tophat input does not appear to be a tophat at the fiber. Instead, the optical system is at a nonzero angle relative to the fiber axis.

This has the effect of convolving each point in the tophat with a ring of size corresponding to its angular misalignment. That is, the effect of angular misalignment is not to convolve the profile with a Gaussian as microbends do; by analyzing the shape of a profile dropoff, the effect of angular misalignment can be separated from that of microbend FRD. In 2D, such an angularly misaligned profile from rings is difficult to calculate analytically; however, in 1D, the convolution kernel of a profile with an angular misalignment a would behave as

$$k(\theta) \propto \frac{1}{\sqrt{1 - (\frac{\theta}{a})^2}}. \tag{2.1}$$

Note how this convolution kernel is bimodal at $\theta = \pm a$, yielding a dropoff distinct from a gaussian convolution. Such behavior has a distinct effect on the point spread function compared to FRD and must be considered independently.

To first order, the net width of the dropoff, σ_{TOT}, is then the sum of the rms angular misalignment kernel width (of $\frac{a}{\sqrt{2}}$) and the Gaussian kernel width (independent of

misalignment, called σ_{FRD}). That is, $\sigma_{TOT}^2 \approx \sigma_{FRD}^2 + \frac{a^2}{2}$. A more thorough analysis of the convolved functions approximates an analytic FRD σ_{TOT} of

$$\sigma_{\mathrm{TOT}}^2 \approx \sigma_{\mathrm{FRD}}^2 \left(1 + \frac{1 + A^2}{2 + 1.5A^2} A^2\right), \tag{2.2}$$

where $A = \frac{a}{\sigma_{\mathrm{FRD}}}$. This estimate of σ_{TOT} varies by $< 1\%$ from the numerical integration result for angular misalignments $A \leq 6$.

Figure 2.2 visualizes how angular misalignment may affect the profile of the dropoff using a model of a uniform input profile, for a given σ_{TOT}. Notably, the error function dropoff from a purely Gaussian convolution becomes bimodal with large angular misalignments, and the effective width of the profile for a given FRD increases with angular misalignment. Note that holding σ_{TOT} constant for a range of angular misalignments allows for a comparison of angular misalignments, but for a fixed σ_{FRD} angular misalignments increase the width of the dropoff.

Also from Figure 2.2, note that from the model of a uniform beam with f number 2.8 (that is, numerical aperture, or NA, of 0.1785), the amount of light cutoff at f number 2.5 (NA of 0.2) can also be seen and the light cutoff can be determined. At 8.9 mrad of σ_{TOT} and no angular misalignment, only 0.03% of the light is cut off, whereas for comparison, at 20 mrad of σ_{TOT} and no angular misalignment, about 1.9% of the light is blocked.

Again, this model should be related back to Gloge's modal diffusion theory; angular misalignments can be factored in with an appropriate choice of $G(\theta', \phi')$ using equation (1.4). Detailed analysis is left for future work; however, the feasibility of this paper's model can be tested using a simple $G(\theta', \phi')$. A circle in a plane tilted at an angle with respect to a viewer appears to be an ellipse. Thus, consider the profile of an ellipse for $G(\theta', \phi')$. Because only G depends on ϕ' in Equation (1.4), we can substitute it with a rotationally averaged over ϕ' function of $\bar{G}(\theta')$; the 1D profile of a rotationally averaged ellipse has an approximately bimodal distribution similar to a step function convolved with the kernel in equation (2.1). An example of such a convolution is shown in figure 2.3. Overall, the simplified model is consistent with FRD results in the literature and allows for a simple quantification of angular misalignment that is not unreasonable.

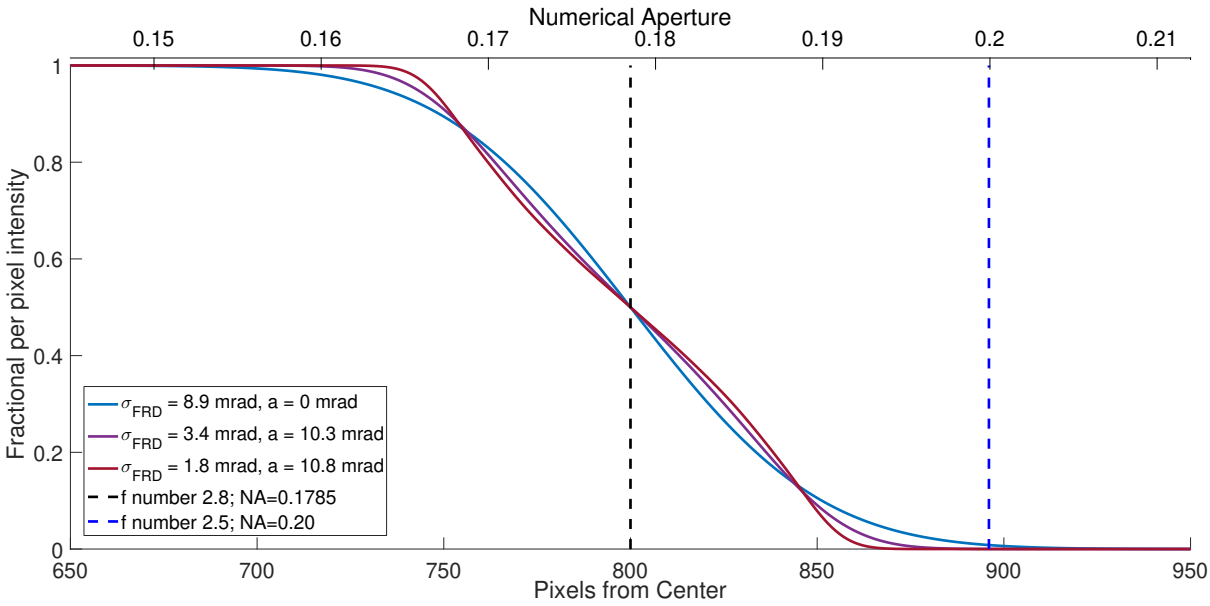

Figure 2.2 Dropoff in pixel intensity for the angular misalignment model with uniform input beam of f number 2.8 (numerical aperture of 0.1785). The effect on the profile for the same net width σ_{TOT} = 8.9 mrad are shown for varying angular misalignments, which corresponds to a different gaussian contribution from FRD (large angles are shown to emphasize the effect of angular misalignment). Also shown is the f number of 2.5 corresponding to the spectroscope cutoff. The light lost at the cutoff varies at a given σ_{TOT} for different angular misalignments.

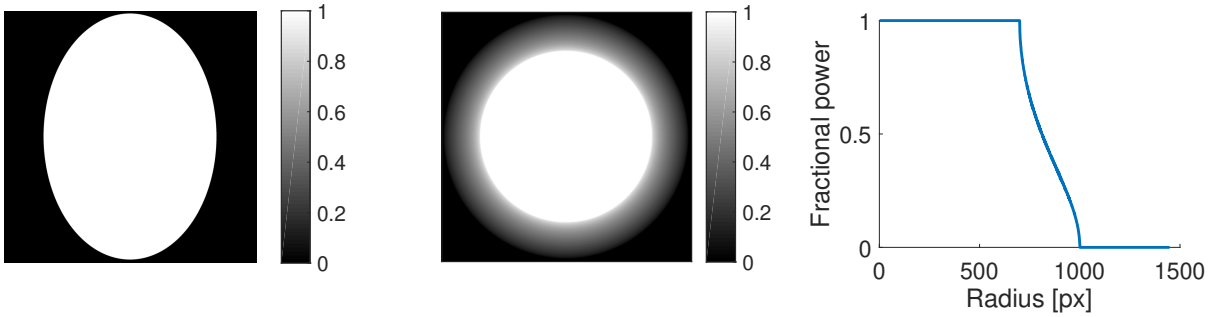

Figure 2.3 Simple example of an ellipse profile (left) that to first order approximates a tilted circle. A figure demonstrating what a 2D profile with the rotationally averaged profile is shown in the middle panel, with its 1D profile from the center shown on the right. Notably, the dropoff in the 1D profile does not appear to behave like an error function; instead, it is similar to an image convolved with a ring. This suggests how our model could be related to Gloge's power distribution model.

2.3 Hardware

In order to measure FRD well, the input illumination into the fiber must be well-characterized, and the camera must have enough precision to determine small vari-

ations in the output profile. This experiment is designed to compactly measure FRD variations in a fiber illuminated with uniform intensity up to a given numerical aperture. Furthermore, the experiment is designed so that the illumination is uniform over a spot of a $\gtrsim$ 9.5mm size, putting a less strict requirement on fiber and illuminator alignment. But the primary purpose of this design is to enable FRD measurement of a fiber throughout its range of motion in a Subaru fiber positioner without constant realignment; as stated in Section 2.6, the fiber positioner patrol region size is 9.5mm and fits within the illumination spot size.

The illuminator system generates a 10mm diameter telecentric image with uniform pupil illumination. Light from a 450nm LED source is collimated by a 100mm focal length, 50mm diameter planoconvex lens. An aperture stop is formed by an EDC-15-08160-A engineered diffuser from RPC Photonics, which uniformly distributes the collimated beam into a 15° cone. At the aperture stop, an 18-vane adjustable iris provides a round aperture of adjustable diameter. Light is focused to the image plane with a 100mm focal length, 50mm diameter doublet, located near the aperture stop. A 100mm focal length, 15mm diameter plano-convex singlet is used as a field lens, ensuring the illumination is across the image plane. All optics were mounted into an off-the-shelf cage system, and baffling was used to shield the illuminator from external light. The experimental illuminator and camera are shown in Figure 2.4 and in a Zemax schematic in Figure 2.5.

The illumination color was chosen to be approximately monochromatic to avoid concerns about FRD variations with wavelength, because there is literature indicating that FRD effects increase with increasing wavelength. In particular, Gloge's coupling coefficient D (see Section 2.2) is proportional to λ^2, causing the predicted FRD of his model (equation (1.3)) to be proportional to wavelength, and there are groups that have experimentally found such a dependence (e.g., C. L. Poppett and J. R. Allington-Smith (2007)). As a result, FRD in the red to near infrared bands measured in the PFS may be larger than the values calculated here. Wavelength dependence with FRD is not fully established, however; for instance, see also Murphy et al. (2008).

The light from the illuminator is incident upon a Polymicro fiber with model number FBP127165190 (part number 1068020148) indicating a FBP fiber with a 127 μm core diameter, 165 μm clad diameter, and 190 μm buffer diameter; the same type of fiber as will be used in the PFS. FBP fiber is a low hydroxyl (-OH) fiber well-suited for astronomy, designed to accept broadband illumination from near infrared

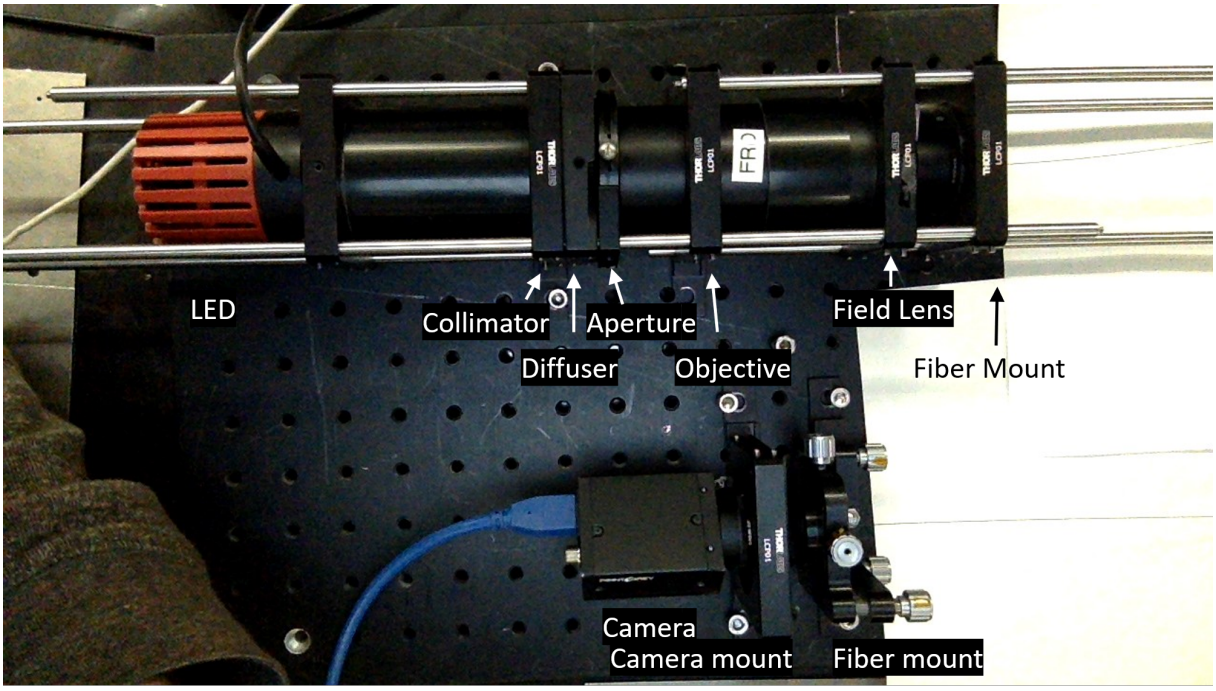

Figure 2.4 Picture of the main camera and illuminator setup of the experiment, with fiber extending off the right side of the image. Components of the illuminator and camera setup are labeled.

to ultraviolet; additional measurements on wavelength-dependent throughput and FRD of this fiber are in dos Santos et al. (2014). The fiber end is terminated and either fitted with a zirconium ferrule or, when in a Cobra fiber positioner, fitted with a microlens in the Cobra fiber arm (See section 2.6). The microlens takes an f/2.2 beam at the edge of the acceptance range in the fiber and increases its f number to f/2.8. The f/2.8 beam is slow enough to be comfortably accepted by the f/2.5 acceptance cone of the spectrograph in the final system, minimizing throughput losses. While the microlens may have its own effect on FRD affecting the final image, this was not observed in our tests.

The image from the fiber is projected onto a CMOS camera system, with a 15mm diameter, 25mm focal length achromatic lens to focus the fiber light onto the camera sensor. Although the camera was mounted onto an optical breadboard, it was not aligned with the fiber end by cage system. Alignment was completed visually with a Newport LPV-1 5-axis mount that held the fiber end (terminated with a zirconium ferrule) based on the output image from the camera. During operation the camera mount was covered with a black shroud to prevent stray light from entering the camera.

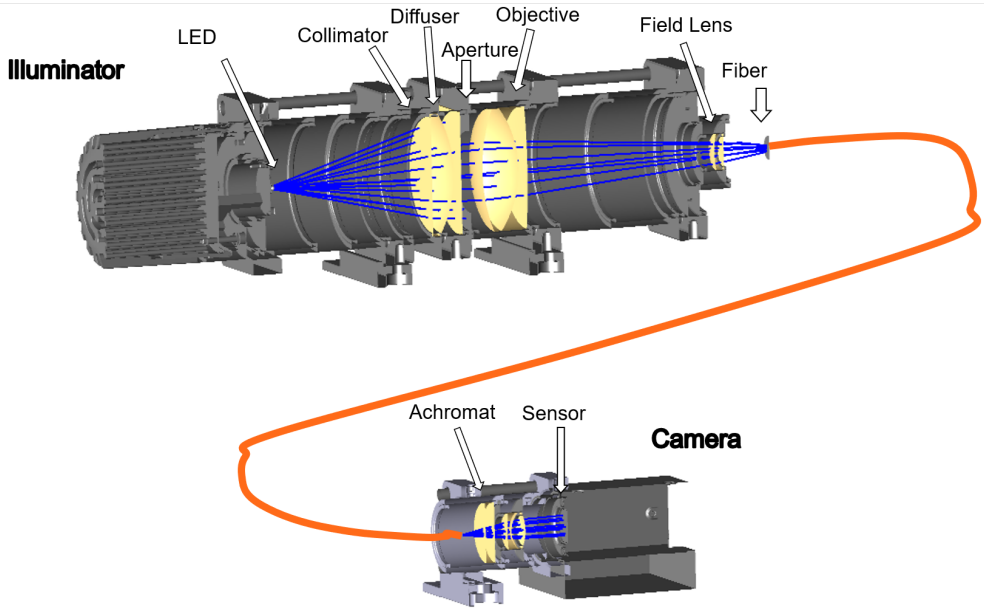

Figure 2.5 Cutout schematic view from above of the apparatus used in the experiment, with blue rays outlining the optical path through the system. The illuminator is at the top of the figure consisting of the LED through the field lens, while the camera is at the bottom with the achromat and sensor. The fiber in a Cobra fiber positioner was also fitted with a microlens to map a f/2.2 beam to an f/2.8 beam. The illuminator and camera were mounted securely to an optical breadboard and the camera was covered with a shroud during measurement.

Image data was analyzed via a Matlab program interfacing with the camera. The center of the profile was determined after fitting for its center after subtracting out a background to remove scattered light and detector offset. Additionally, flats were taken for the camera pointed at a white background. While analysis was done without the flat correction initially, a later flat was used to determine the camera response and vignetting. This correction had a minimal effect (on the order of 0.1 mrad) on the calculation of σ_{TOT}. The center of the circle was found by calculating "white" and "dark" values by fitting Gaussians to histograms of number of instances for each brightness occurrence, then finding all points with 30%, 50% and 70% of the "white" minus "dark" values, fitting each contour to the equation for a circle. Afterward, the azimuthal average of points at the same distance rounded to the nearest pixel from the center was taken and combined into a 1D profile, from which the FRD was analyzed. Small shifts on the order of a pixel could affect FRD measurements by 0.1 mrad, a nontrivial variation, so center finding was analyzed

carefully. To verify that the center was indeed found, in initial images the center was tested by shifting the center within a 5px x 5px square, with the effects on the 1D profile (and in particular, σ_{TOT}) analyzed.

To characterize the dropoff of the profile due to FRD, we found the width (σ_{TOT}) of a 2D Gaussian that, when convolved with a uniform tophat profile, was the same width as the observed dropoff (section 2.2). An example of this procedure is demonstrated in Figure 2.6, which shows the 2D profile and radial profile, and fit for σ_{TOT} depicted in Figure 2.7. In practice, the width of the dropoff (from 85% of max brightness to 15% of max brightness) was calculated and scaled to σ_{TOT}. Fitting for the 85% and 15% allows for a fit that is less biased from small deviations from a normal at large angles due to scattered light, such as due to the small bump at large radius visible in Figure 2.6. Furthermore, this fitting method is more meaningful when angular misalignment is more prominent; each profile for a variety of angular misalignments is normalized to the width of the dropoff between the 85% and 15% brightness levels, as described in more detail in section 2.5.

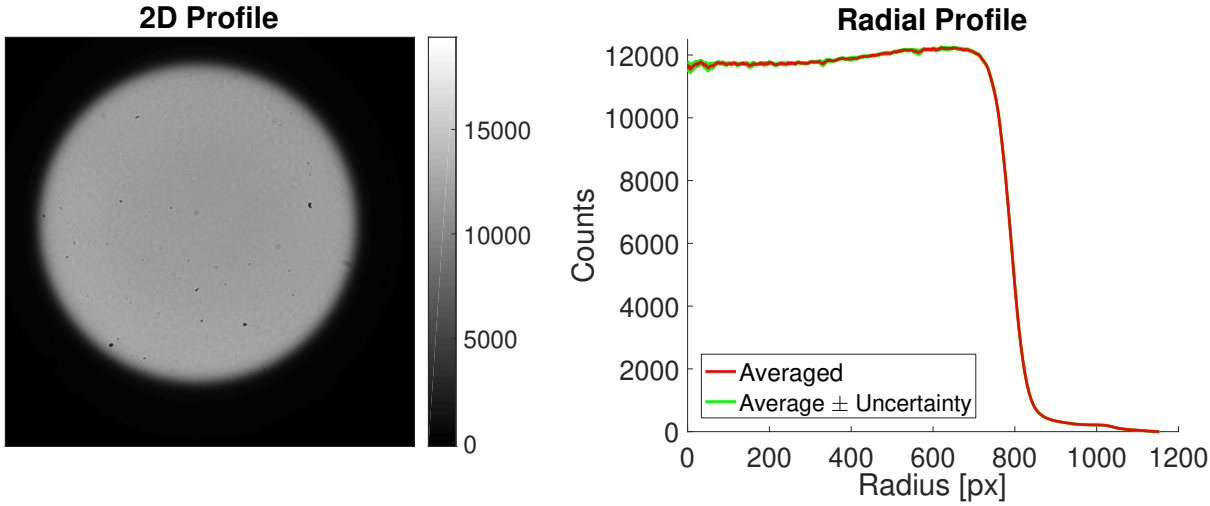

Figure 2.6 Example data analysis image output from 2D image (left) scaled according to counts at the camera to radial profile extracted from the fitted center. The darker spots visible in the image were dust particles and are not intrinsic to the profile, though radially averaging minimizes the effect this has on the data.

Measurement of the widths of the profile dropoffs are made in pixels and then converted into equivalent angular size. However, this means that measurement precision is dictated by pixel size; in practice a pixel corresponded to approximately 0.1 mrad. Multiple images from the same experimental state had dropoff width varying with ±1 pixel, corresponding to a ±0.1 mrad uncertainty from width calculation.

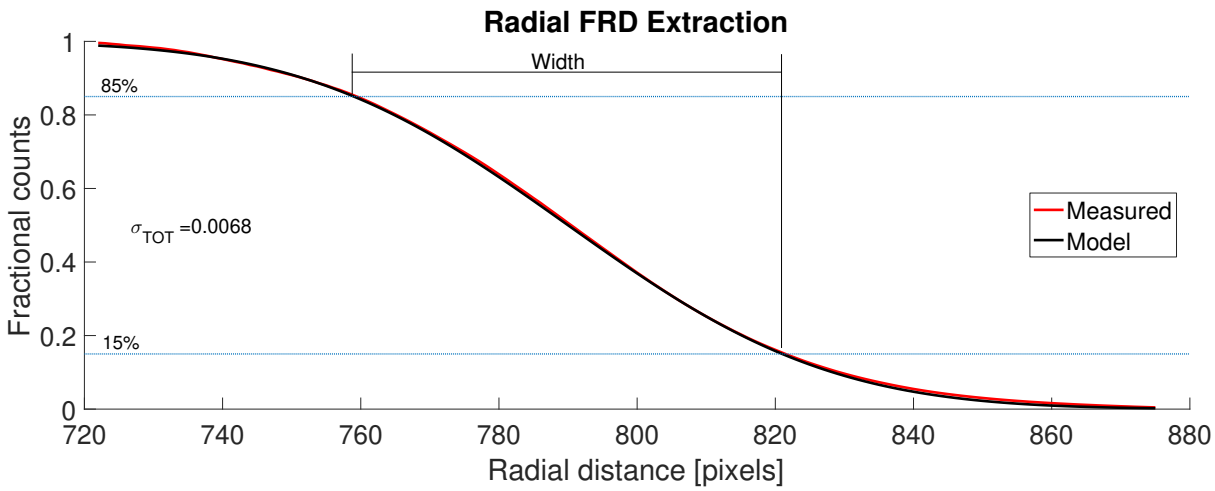

Figure 2.7 A zoomed-in image of the radial profile around the region of interest, the dropoff. A model normal error function calculated from the difference between the 85% and 15% brightness levels (dashed lines) is in good agreement with the observed profile. The width, as indicated in the figure, can be extracted and is proportional to σ_{TOT}.

An uncertainty in the calculation in this method was caused by the calculation of the 85% and 15% brightness radial locations. In particular, the uncertainty for these points was taken to be half the range of radii with the 85% and 15% values within one standard deviation of the average value (scaled for counting statistics with number of uncorrelated data points, respectively; see section 1.2.1).

The basic data analysis was verified with a 100 μm pinhole replacing the fiber to visualize the input to the fiber. The resulting image is shown in Figure 2.8. Notably, the pinhole behaves like a zero length fiber, so it should have a sharp dropoff, whereas there is a nonzero width dropoff actually observed. This effect is expected to add in quadrature with the FRD to give a final width, but the sharpness of the profile was such that this effect was assumed to be negligible. Also, the irregularities seen in the 2D pinhole image demonstrate a pattern with characteristic size of about 20 pixels; in the calculation of the uncertainty of the 85% and 15% brightness levels, the standard deviation of the mean was calculated by dividing the calculated standard deviation at a given radius by the square root of the effective number of uncorrelated pixels at that radius (that is, number of pixels at that radius divided by 20).

2.4 Stresses

It is informative to examine potential sources of FRD due to the fiber itself. Ideally, a perfect fiber would transmit the exact same signal out as was input, but imperfections

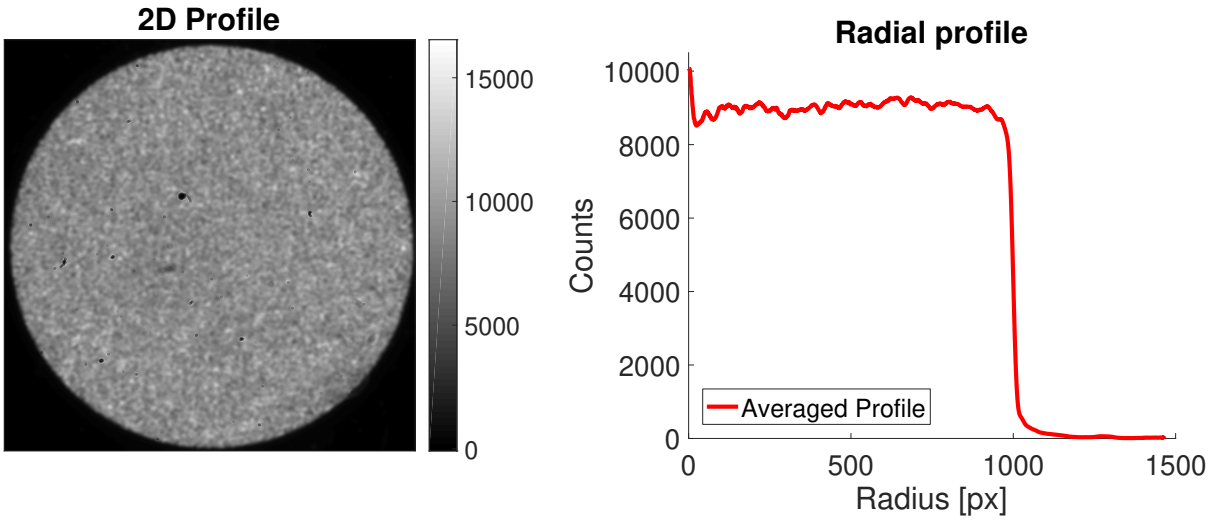

Figure 2.8 Measurement with the fiber replaced by a pinhole. This measurement represents the instrumental limit for the low FRD condition. The correlated speckles in the 2D profile are likely due to fabrication variations across the surface of the diffuser. The width of the dropoff in the radial profile is much lower than the dropoff measured from fibers; the nonzero width may indicate a systematic—though small—overestimation of FRD.

in the fiber geometry can induce coupling to higher-order modes and "spread out" the input light causing FRD. In this subsection, we investigate three sources of stress on a fiber and their effect on FRD using an effective f/2.8 beam. Effects from bending, twisting, and squeezing are presented and related by calculating stress σ on the fiber, with subscripts differentiating stress and FRD. However, only a perfunctory attempt has been made in this work to model FRD as a function of stress, because length over which stress is applied, degree of imperfections in the core/clad interface, fiber cladding Young's modulus, direction of stress applied, and many other factors complicate such an analysis.

We first examined stress due to bending. A Polymicro fiber was subject to a loop of a measured, decreasing radius while measuring FRD, with FRD results in Figure 2.9 and example loop inset. As the literature indicates (Clayton, 1989), large-scale bending (with respect to the $127\mu m$ core of the fiber) does not significantly contribute to the FRD of this system. In particular, no FRD change was found until a bend radius of about 1.25 cm, where it increased by 1 mrad.

The stress due to a loop of radius R and a fiber with fiberglass core/clad of core radius r_{core} depends linearly on its Young's modulus E, as shown in Equation (2.3). Note that the Young's modulus for fiberglass used is large relative to other materials

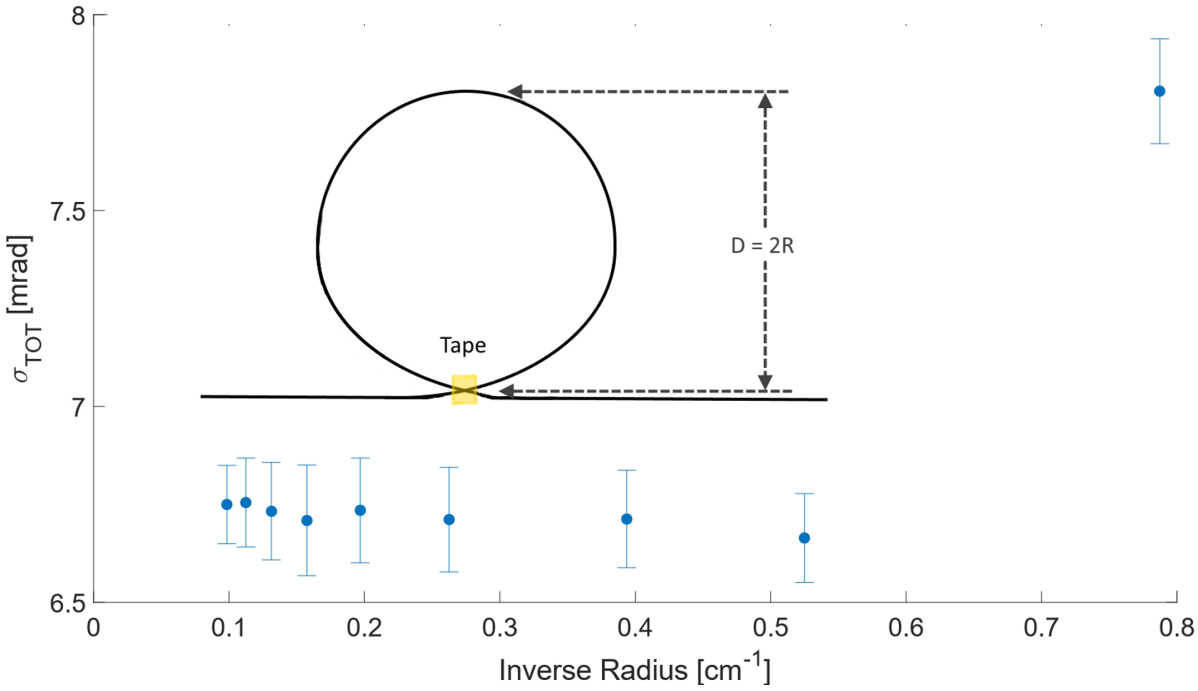

Figure 2.9 FRD as a function of bend curvature, with fiber bent as shown in the inset. No observable change in FRD occurred until a bend radius of 1.3 cm.

but standard for optical fibers, while fiber radius (with buffer included) is taken to be small relative to loop radius.

$$\sigma_{bend} \approx E r_{core} \frac{1}{R}, \tag{2.3}$$

(Hefferon, 1987) where σ_{bend} corresponds to the induced stress on the fiber. In particular, in this fiber the stress where FRD notably increased would be about 500 MPa as a result.

It is worth considering twist as a potential contribution to FRD in comparison to bending, because twisting is expected to be present in the Cobra fiber positioner system up to a full 360° range of motion. It would be informative to determine the stress on the fiber due to twist to predict if there will be an observable effect on FRD. With shear modulus G of clad radius r_{clad}, Equation (2.4) applies for twist of angle $\theta = \pi$

$$\sigma_{twist} = G r_{clad} \frac{\theta}{L} \tag{2.4}$$

(Hefferon, 1987) over length L dictated by the Cobra system, notably similar to the bending stress equation (Equation (2.3)). In this experiment, the fiber is held in place with epoxy at the fiber arm (see Figure 2.13) at the end of the fiber positioner on one side (see Section 2.6), but is not otherwise significantly constrained (allowing L to be on the order of a meter). Thus, the fiber is able to twist over the order of the length of the fiber, and the twist stress is proportionally orders of magnitude lower than that considered in the bend test above. It is expected that twist will not have a significant effect on FRD in this system. In the PFS, the distance between the fiber arm and a segmented tube over which twisting occurs is shorter at about 28 cm, so twist will contribute a larger stress than that from an unconstrained fiber but still significantly smaller than the maximum bending stress tested in this paper.

Beyond bending and twisting that may be induced in fibers during operation of the Subaru telescope, pinching is another possible additional sources of stress. There are strain relief boxes to alleviate this kind of issue, but it is still expected that some amount of applied stress will change during system operation.

To test the effect of pinching on a fiber, a Polymicro fiber was subject to an increasing weight on an aluminum base over a $L = 1.5$ cm length of fiber, up to a few kilograms. The weight can be converted to an average pressure after calculating the effect of compression of the fiber itself due to the weight. In particular, the half-width b of the fiber due to the compression is given by

$$b = \sqrt{\frac{4F\left(\frac{1-\nu_1^2}{E_1} + \frac{1-\nu_2^2}{E_2}\right)}{\pi L\left(\frac{1}{R_1} + \frac{1}{R_2}\right)}}, \tag{2.5}$$

(Bamberg, 2006) where F is the force applied to the fiber, ν is the Poisson's ratio for the two interfacing objects, denoted by the subscripts (let object 1 be the aluminum base and object 2 be the polyimide buffer of the fiber), E is Young's modulus, and R is the radius of each object.

Average pressure P on the buffer thus is proportional to $\sqrt{F}$. A plot demonstrating the σ_{TOT} dependence on P is shown in Figure 2.10. There is an approximately linear relationship between pressure on the buffer and σ_{TOT}. However, light propagates through the core and depends on the core/clad interface, so the buffer pressure alone may not characterize the physical nature of this FRD increase.

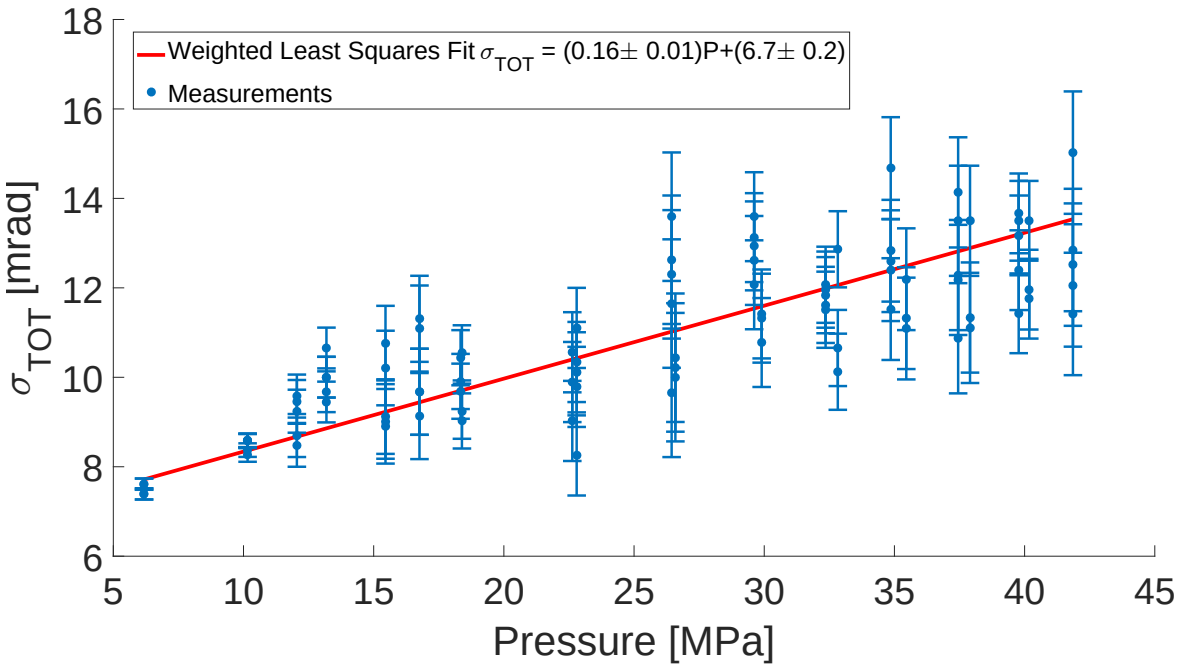

Figure 2.10 Variation of FRD with applied radial pressure to the fiber buffer. FRD appears to grow roughly linearly with applied buffer pressure, although extrapolation to lower pressures may not be accurate. Scatter also increases with applied weight, indicating how small variations in pressure distribution can significantly affect FRD measurements as weight increases. Error bars in this figure indicate the standard deviation of all measurements at a given pressure.

2.5 Angular misalignment

Angular misalignment is known to contribute to the power distribution fiber output. Due to this, measurements of FRD often rely on optical systems that are carefully aligned. This holds especially true for the cone test. While ideally in practice every fiber would be coaxial with a uniform beam, in practice, a fiber in a Cobra fiber positioner will move through a range of angular misalignments during operation due to impossibility of perfect angular alignment. Furthermore, due to the design of fibers throughout the focal plane, some fibers necessarily receive a non rotationally symmetric profile, violating the simplification that permits σ_{FRD} to characterize the point spread function without additional parameters. Thus, angular misalignments' effects on FRD must be well understood to correct for foreground sky signal throughout telescope operation for any fiber positioning.

A test was performed with a f/2.8 beam using two Polymicro fibers (with ferrules on both ends) to determine the effect of angular misalignment on the measurement

of FRD. To investigate the effects of angular misalignment, the FRD from each fiber (taken individually) was minimized with respect to the two angular degrees of freedom in a Newport LPV-1 mount. The minimum was taken to correspond to the least angular misalignment. Then, adjustments to this position were taken in $\approx \frac{1}{8}$ mm steps in the screws holding the mount's angular position (corresponding to about 3 milliradian angular adjustments) with FRD measured at each stop. The angular misalignment was determined from the geometry of the mount relative to its calculated minimum. The results from this test as well as fits to equation (2.2)'s prediction are shown in Figure 2.11.

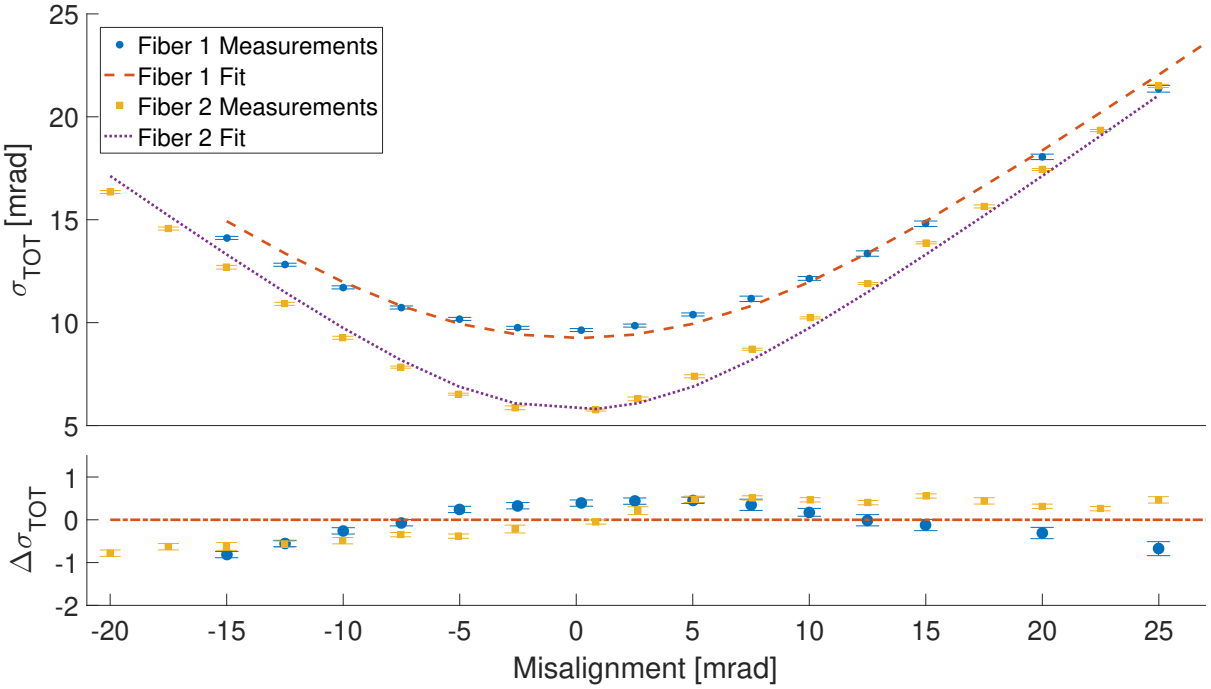

Figure 2.11 Variation of FRD with geometric angular misalignment from fitted minimum for two fibers. The effect is approximately hyperbolic, fitted for σ_{FRD} (see Section 2.5) and an x-axis offset. The bottom panel shows the residuals, which are subtracted from the fit. The minimum σ_{TOT}, roughly corresponding to the σ_{FRD} of each fiber, varies between the two but is within expected variation. While the fit is good for just effectively fitting to a minimum, there appears to be a nontrivial residual for the fiber of larger σ_{FRD}.

However, angular misalignment can also be determined directly from the profile. By taking the width between the 85% and 15% brightness positions, a family of 1D profiles with angular misalignment ratios A from 0 to 6 were calculated with 0.1 step increments (See section 2.5 for details about A) and fitted to the profile, with the final value of A selected from the best fit. Because both A and σ_{TOT} are calculated

from this model, using equation (2.2), σ_{FRD} and thus angular misalignment a can also be found. The geometric angle can be compared to the angle predicted from the model to determine the model's efficacy, as shown in Figure 2.12

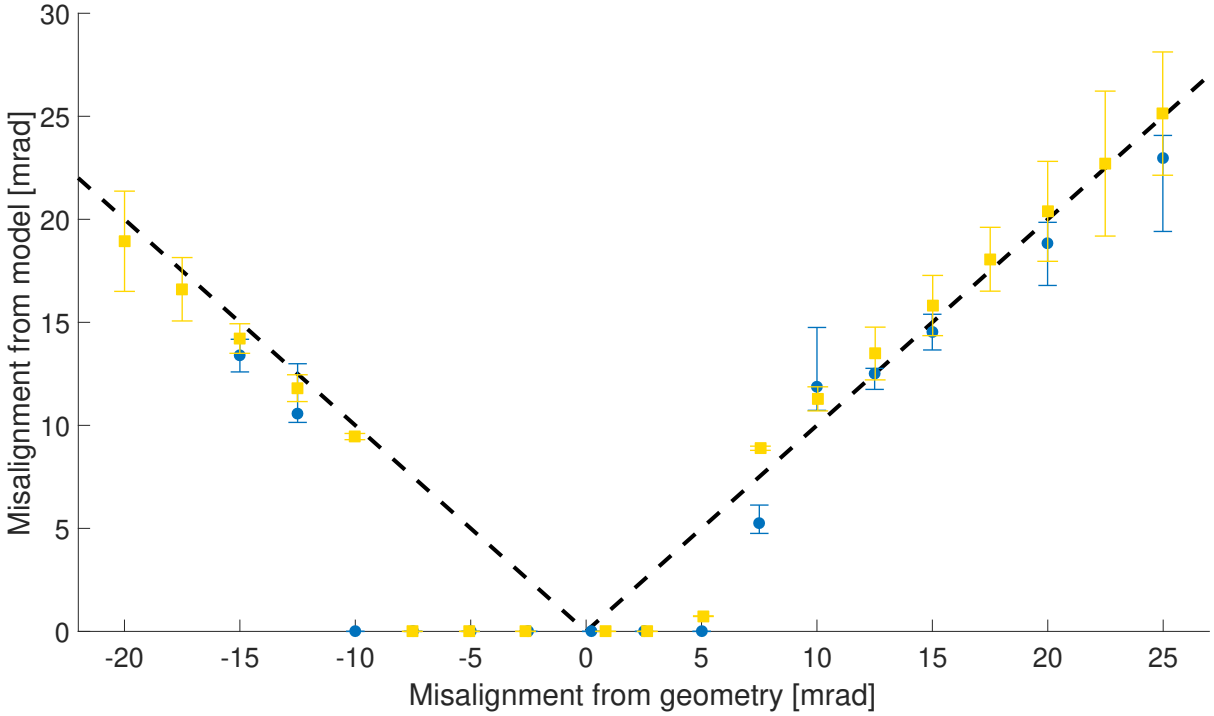

Figure 2.12 Angular misalignment between the geometric misalignment and the algorithmically calculated misalignment, with errors calculated from σ_{TOT} and the range of angular misalignment with sum of least squares within 5% of the minimum fit. Agreement between the angles is low at lower angular misalignments, possibly due to nonuniform profile effects that dominate misalignment effects for low misalignment, but is good at large angles. This result indicates that the misalignment extraction from the model is reasonable.

Verification of the angular misalignment effect on FRD with angle is particularly valuable when interpreting the FRD with Cobra fiber position, because an imperfectly aligned Cobra will traverse a range of angular misalignments that can noticeably affect FRD measurements.

2.6 Cobra FRD and Discussion

The Cobra Fiber Positioner is a θ-ϕ eccentric-axis fiber positioner that permits a fiber to be located anywhere within a 9.5mm patrol region. The Cobra units were constructed by New Scale Technologies, and the positioning of a Cobra was controlled using New Scale Technology's Pathway program with pulses of specified number of steps and length. However, mapping from steps to angular position

is not perfectly accurate which does cause an uncertainty in position that is not calibrated for. To minimize angular error, the Cobra fiber positioner was mounted to a machined Thorlabs LCP01 piece to be aligned using the Thorlabs cage system. Figure 2.13 depicts a Cobra used in the conducted experiment.

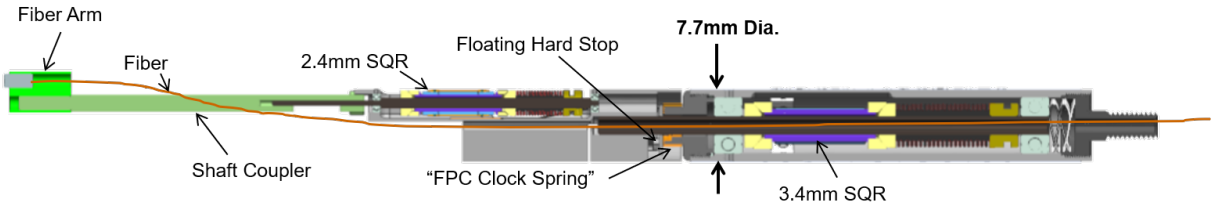

Figure 2.13 Schematic cutaway of a Cobra fiber positioner, with various parts and parameters marked. Figure from the Subaru PFS collaboration's Cobra Fiber Positioner Manufacturing Readiness Review. Also see Fisher et al. (2014) for a Cobra figure and more discussion of the Cobra.

The FRD of a fiber fitted in a Cobra fiber positioner with a microlens was measured throughout the range of the positioner's motion in both stages with a f/2.2 beam, which becomes f/2.8 after the microlens. Due to the nature of the Cobra mount used, angular alignment could not be adjusted to be minimized. The FRD was measured in steps of 500 steps from 0 to 3500 in stage 1 and back again to determine hysteresis. The measured FRD is shown in Figure 2.14.

The FRD through the positionings in stage 1 (θ stage) appears to increase and then decrease, completing a cycle in the 360° range of stage 1. Furthermore, while FRD varies across stage 1 motion, there is no noticeable systematic increase in FRD after the full 360° twist is imposed on the fiber, which would increase twist while minimizing net angular misalignment change. Thus, twist appears to not contribute noticeably to FRD as was expected due to its low imposed stress (see Section 2.4). Thus, FRD variations across stage 1 appear to be due to angular misalignment.

Across positions in stage 2, there is a more significant increase in σ_{TOT}. However, the amplitude of the variations across stage 1 also increase, indicating a larger angular misalignment. This complicates the analysis of bend stress vs. angular misalignment as the primary cause of the FRD increase.

The expected bend stress induced due to the Cobra fiber positioner can be calculated from Equation (2.3). By substituting in $R = 3.12$ cm, the minimum inverse curvature of the fiber in a Cobra after approximating its path as a helix, the resulting stress is lower than the stress in the bending test where σ_{TOT} notably increased.

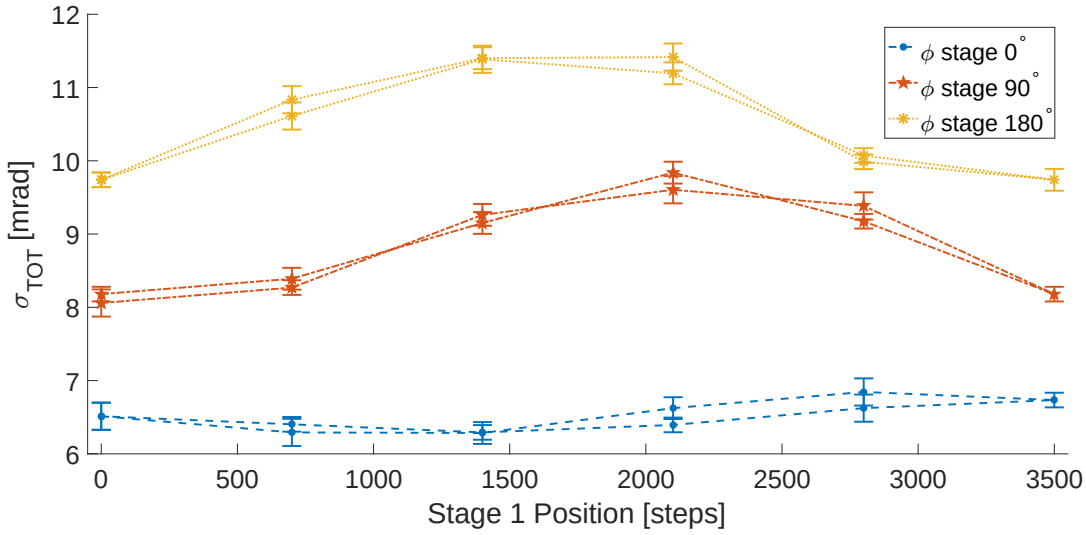

Figure 2.14 Profile σ_{TOT} of a fiber with microlens throughout the range of motion in both stages of the Cobra positioner. There is a significant variation of σ_{TOT} through stage 1 (θ stage) and stage 2 (ϕ stage) motion. The sinusoidal behaviour across stage 1 indicates an angular misalignment effect. Uncertainties of about ±50 steps in stage 1, corresponding to ±5° angular precision, were also present though not depicted in this figure.

The angular misalignment can be measured by applying Equation (2.2) to the range of FRDs through stage 1 or stage 2 motion and calculating the variation of angular misalignments required to generate the resulting plot. This angular misalignment measurement can help give insight about the possible effect on FRD during Cobra operation. The extracted angular data agrees with the above predictions, as seen in Figure 2.15.

The angular misalignment extracted from the profiles thus allows for σ_{FRD} to be extracted directly from the profiles in this system, as shown in Figure 2.16. These values of σ_{FRD} are broadly consistent with a constant σ_{FRD} of about 6.5 mrad throughout all fiber positions, indicating that the stresses during operation did not significantly increase FRD. From the values of σ_{TOT} alone, it would be impossible to determine the source of profile broadening.

In conclusion, a model of fiber profile due to FRD and angular misalignment

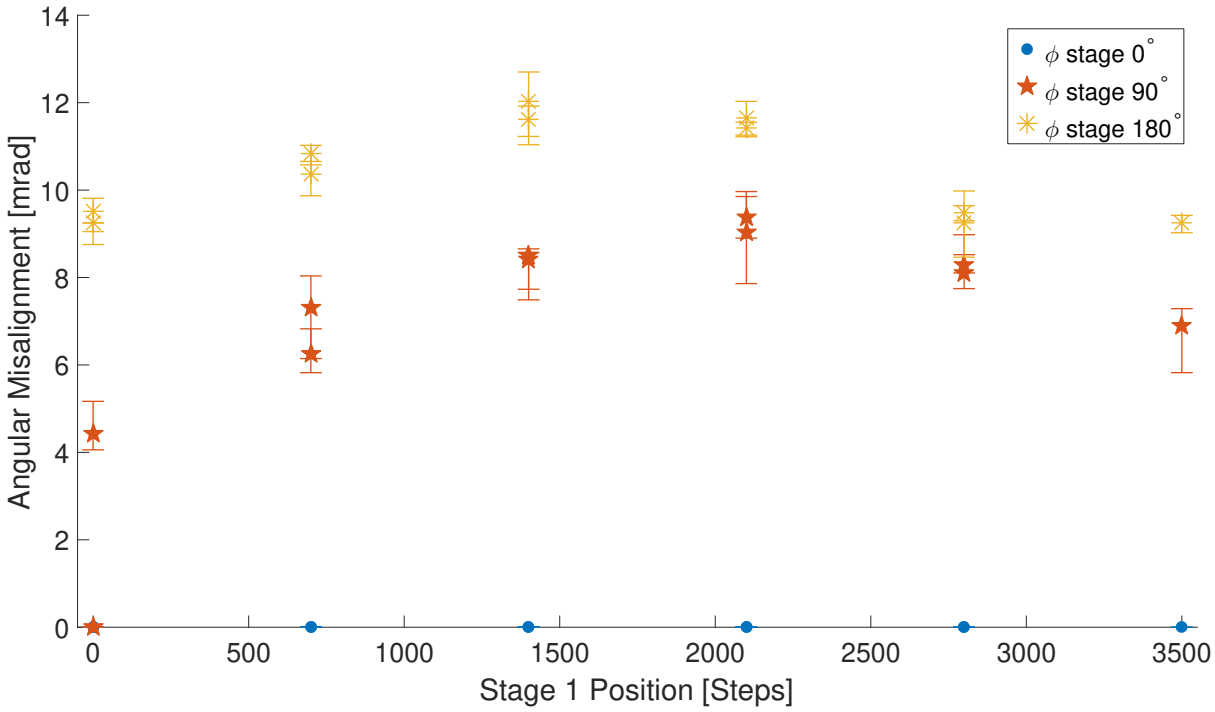

Figure 2.15 Angular misalignment as calculated from the power distribution model in this paper (section 2.2). The sinusoidal behavior across stage 1 suggests that the σ_{TOT} variation in stage 1 is indeed due to angular misalignment rather than stress, and angular misalignment due to the ϕ stage is also apparent.

was presented and used to analyze cone profiles of a fiber under stress or angular misalignment. While high stresses were found to increase FRD, FRD did not significantly increase for low stress. Angular misalignment was found to have a significant effect on the profile width, which was fitted by the model considered. The FRD component of the model is represented as a Gaussian as seen in previous literature results (e.g. Haynes et al. (2011)), whereas the angular misalignment component of the profile is simplified into one parameter. Some stresses that would be present in the Subaru PFS's Cobra fiber positioner system are considered and expected to be low during operation. The angular misalignment from the presented model is compared to a test with angular misalignment calculated geometrically and found to be consistent for angular misalignments larger than about 5 milliradians. Thus, the model could then be applied to the Cobra fiber positioner throughout its range of motion, indicating minimal FRD increase, if any, that would have otherwise been obscured by the angular misalignment present in the system. An experimental setup such as used in this paper combined with the model used should simplify analysis of FRD in dynamic systems without the need to realign for each

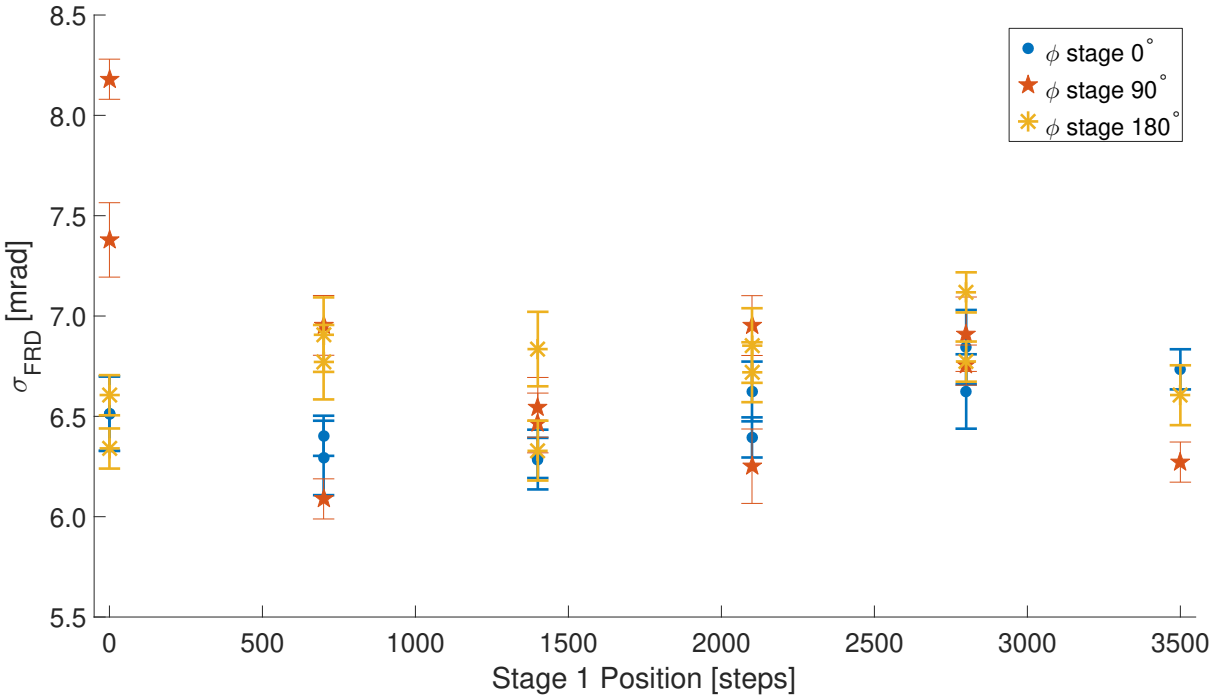

Figure 2.16 FRD extracted from the fiber profiles after considering angular misalignment. The FRD can be well-characterized in a single experimental setup across varying configurations due to this angular misalignment extraction, and is consistent with minimal stress on the fiber during Cobra operation.

configuration to be tested.

Acknowledgments

We are grateful to the Kavli Institute for the Physics and Mathematics of the Universe, the National Astronomical Observatory of Japan, and the Subaru PFS collaboration for their feedback and recommendations throughout this project. We would especially like to thank Naoyuki Tamura and Yuki Moritani for discussions and direction for this project, as well as Leandro dos Santos for fiber preparation. This material is based upon work supported by the National Science Foundation under MSIP grant no. 1636426.

This research has made use of NASA's Astrophysics Data System.

Chapter 3

FOCAL RATIO DEGRADATION, THE POINT SPREAD FUNCTION, AND THEIR EFFECT ON SKY SUBTRACTION IN FIBER-FED ASTRONOMICAL SPECTROGRAPHS

Abstract

Multi-fiber astronomical spectrographs target many objects in a single field, each with their own spectra. However, their sky subtraction is complicated relative to slit spectrographs due in part to focal ratio degradation (FRD), the broadening of light traveling through the fiber due to physical imperfections in the fiber. While the effect of FRD on light is well studied, how the FRD from the fiber translates to change in the spectrum is not as well understood. Using the Subaru Prime Focus Spectrograph's 2D-Data reduction pipeline, the effect of FRD on point spread functions is studied. The largest effect on the point spread function (PSF) due to changing FRD relative to the detector was a dipole-like component due to a shifting centroid. Even when centroid is fixed, we find that FRD on the order of 3 milliradians affects PSFs on the order of 1-2% at a distance of 4-5 pixels from their centers. We were able to extract FRD from simulated PSFs with an uncertainty of 2 milliradians toward the center of the spectrograph detector, falling off toward the edges. Our results indicate that proper FRD modeling can improve sky subtraction near sky lines.

3.1 Introduction

Spectroscopy is a powerful tool to determine the composition and kinematics of astronomical objects, up to the limits imposed by the instrument. In order to increase the precision of spectroscopy or observe fainter objects' spectra, light from the source must by maximized and effects from other sources must be minimized. In particular, the surface brightnesses of many astronomical objects of interest are fainter than the sky. As a result, highly precise sky subtraction is necessary to obtain scientifically useful spectra. The precision of the sky subtraction translates into fainter limiting magnitudes.

Traditionally, spectrographs used slits to acquire spectra, but recently massively multiplexed fiber optic spectrographs have been gaining traction, such as the Subaru Prime Focus Spectrograph (PFS) (Sugai et al., 2015), DESI (Flaugher and Bebek, 2014), MOONS (Cirasuolo et al., 2011), 4MOST (de Jong et al., 2012), and WEAVE (Dalton et al., 2012). Multi-fiber spectrographs provide an advantage over standard slit spectrographs due to their ability to target many objects in a single field, each with their own spectra (Barden, 1994), accessing even closely clustered targets within a wide field of view which allows for more efficient spectroscopy surveying.

However, unlike with standard slit spectroscopy, where some of the slit is filled with only sky light, fibers may be entirely filled with the object spectrum. As a result, sky subtraction cannot be done from just the object fiber. Sky is typically measured by allotting some fraction of fibers, spatially distributed across the field, to just the sky; the light from these fibers is spatially distributed, averaged, and then taken to be the sky signal. This signal is then subtracted from spectra of fibers pointed at targets (Lissandrini, Cristiani, and La Franca, 1994).

While such a sky subtraction procedure can be effective, in practice there are many complications that must be accounted for to maintain a high precision of sky subtraction. Sky light is not uniform across a field. While averaging the results from many fibers can give a mean sky value, this introduces errors for each individual fiber if sky fluctuation is large and not accounted for. Furthermore, each fiber is unique, imposing separate instrumental effects for each fiber spectrum. While averaging sky fiber spectra also averages these instrumental effects for an approximate mean fiber behavior, it again introduces error since each fiber is not unique.

Theoretically, if the point spread function (PSF) through a fiber was constant, it could be measured and characterized in advance to model each fiber's spectrum accurately. However, in practice, the fiber's PSF does dynamically change during

telescope operation due to focal ratio degradation (FRD).

The purpose of this paper is to quantify effect of FRD on sky subtraction. This paper focuses on work being done for the upcoming Subaru PFS, but approaches the subject in a way that is applicable to any fiber spectrograph.

Focal Ratio Degradation and its qualitative effect on sky subtraction

FRD is the scattering of light traveling through a fiber due to its imperfections, such as stresses, imperfect core/clad interface, or in its end face preparation (Clayton, 1989; Oliveira, de Oliveira, and dos Santos, 2005). This results in an increase in the focal ratio of light through the fiber, blurring the input. This change between the input and output light from fibers due to FRD has been well characterized in various systems (Gloge, 1972; Haynes et al., 2011). It behaves similarly to a Gaussian convolution on the input.

During telescope operation, the stress on the fiber can vary due to differing telescope pointing resulting in different gravity vectors on the fibers, fibers directly stressed by positioners, or other factors. Thus, FRD can vary during telescope activity, and it must be well modeled.

In (Belland et al., 2019) the FRD imposed by the fiber positioner system on a test fiber was examined. We found that small angular misalignments may also be present in the optical path, but those can to first order be modeled as an additional component to FRD. While angular misalignments can broaden fiber outputs, we utilized the unique signature of angular misalignment to extract FRD as a function of positioning. We found that the FRD did not change throughout the patrol region of the fiber, though angular misalignment did increase broadening the fiber output. While the constant FRD is a promising result, we still need to understand how it translates to the detector and how it can affect the PFS's spectra.

Particularly, the light at the spectrograph's detector is not simply the output of the fiber; instead it is focused to a point at the spectrograph camera). Thus, the effect of FRD on spectra is more complicated to understand, and is the focus of this paper.

But if FRD has a small effect on lines/PSFs, then does it actually matter for sky subtraction? As seen in Figure 3.1, small variations in each sky line over the many OH sky lines expected in the Subaru PFS data would result in a significant overall effect on the quality of reduced spectra. In particular, the upcoming Subaru PFS is aiming to reach a sky subtraction level of 0.5% of the continuum for its science goals (Takada et al., 2014). If FRD affects a few pixels around each sky line above

this level, as we show in this paper, then FRD must be incorporated into the model for each fiber to achieve the PFS sky subtraction requirement.

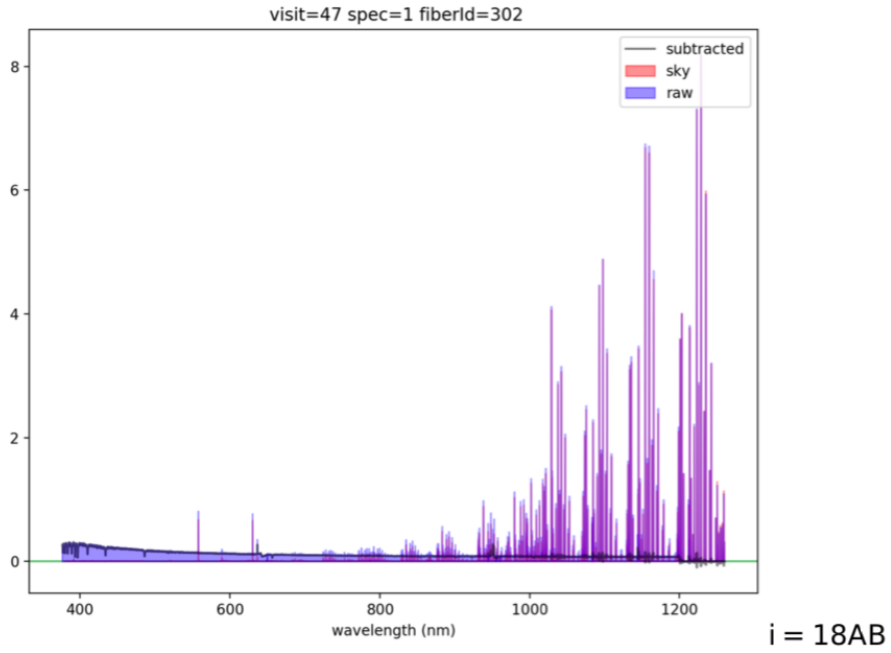

Figure 3.1 Simulated PFS spectrum for an star with $i = 18AB$ (Lupton, 2021). The total spectrum is shaded in blue. The portion attributable to sky emission is shaded in blue. In the 1000-1200 nm range, the number and strength of sky lines are very large relative to the target spectrum. Even a fraction of a percent error in the modeling of these lines would significantly affect the final sky-subtracted spectrum.

We discuss how FRD affects the point spread function for Subaru/PFS in Section 3.2 through simulations using the PFS's 2D-Data Reduction Pipeline developed by Neven Caplar. Next, we discuss extraction of FRD from PSFs and how well this extraction does in Section 3.3. Finally, we review the results and describe our future work in Section 3.4.

3.2 FRD's effect on PSF

First, as alluded to in the Section 3.1, we must address how FRD affects the point spread function in order to understand what effects we would expect to see in sky lines. The effect of FRD on light traveling through the fiber can be modeled as a convolution of an azimuthally averaged input light distribution with a Gaussian (Gambling, Payne, and Matsumura, 1975; Haynes et al., 2011; Belland et al., 2019), causing flux from a tophat distribution to increase at lower f-ratios (i.e. larger angles) and decrease at higher f-ratios.

In addition, the light path from the fiber to the detector in the spectrograph may also encounter obscuration from parts of the spectrograph that lie in the optical path. Furthermore, diffraction may affect the distribution of light around these obscured areas in the optical path to the detector.

To translate the light from the fibers (pupil image) to an image focused in the camera's detector (in-focus image), the wavefronts of light must also be properly modeled in order to accurately interfere light through that optical path. We can perform a Fourier analysis on the wavefronts to determine the in-focus PSF as seen from Equation 3.1 reproduced from (Meyers, 2018)

$$I(x;\theta) \propto \left| \mathfrak{F}\left[P(u;\theta) \exp\left(\frac{-2\pi i}{\lambda} W(u;\theta) \right) \right] \right|^2 , \tag{3.1}$$

where $I(x;\theta)$ represents the point spread function from light originating at angle θ in the sky at focal plane position x, $P(u;\theta)$ is the pupil obscuration function at position u in the pupil plane from angle θ, and $W(u;\theta)$ represents the wavefront at u from sky angle θ. Effectively, the wavefront $W(u;\theta)$ changes with FRD, but its effect on the PSF is modeled by a Fourier transform.

2D variation

In order to simulate the image out-of-focus, a more complex process can be used; these methods are also incorporated in the 2D-DRP. The code, developed by Neven Caplar, is available at https://github.com/Subaru-PFS/dev_2ddrp

In order to generate images at the spectrograph, pupil images were simulated using the PFS's 2D-DRP simulator (in development) and focused to create camera images to analyze. The pupil images and wavefronts were analyzed during testing of the Subaru PFS at Laboratoire d'Astrophysique de Marseille on December 4, 2019, using the HgAr calibration lamp. Parameters describing the wavefronts in Zernike components and pupil images were used to simulate the in-focus images. Figure 3.2 shows a simulated pupil image and its corresponding image on the spectrograph.

With the ability to generate pupil images and in-focus images in the spectrograph, we can generate images at different FRD values while keeping other parameters describing the pupil image constant, to isolate the effect of FRD on the final spectrograph image. Each image is scaled to 50000 counts in the brightest pixel, that is, near saturation but still within the linear regime for the PFS camera.

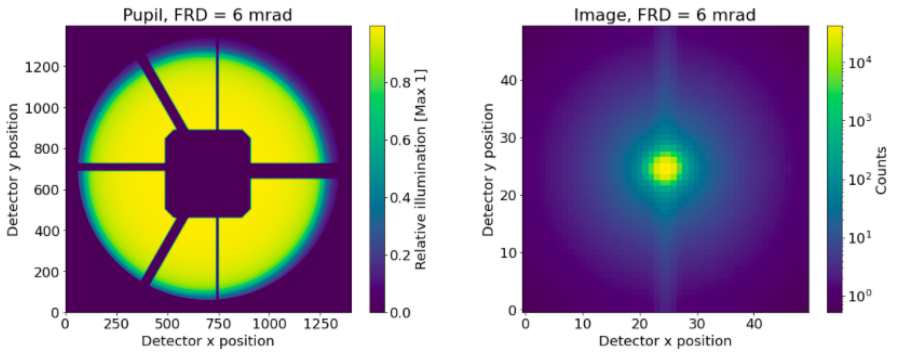

Figure 3.2 Left: Simulated value of a pupil image from a fiber at the center of the spectrograph. The pupil is obscured by the spectrograph detector and the "spider" that supports it. Right: The in-focus PSF simulated from the pupil image on the left. This pupil image can be used to easily identify FRD variations while PSFs from the 2D-DRP allow for FRD's effect on spectra to be better understood.

We first investigated the variation of the 2D point spread function with variations of FRD. This work extends to FRDs (20-30 mrad) expected to be representative of of the expected entire light path from the prime focus to spectrograph. We imaged the pupil, where FRD effects are manifested as light dropoff around the edge of the image, and the corresponding PSFs calculated from the 2D PSF code for increasing values of FRD (6-30 mrad in steps of 6 mrad). Each image was from the PSF centered on the simulated detector position (1992, 1314) in (x, y) ordering. That is, each PSF was modeled about the same origin. Then, we took the differences between PSFs with incrementally increasing FRD values to determine how the FRD change affected the PSF. This work is compiled together and example figures displaying the FRD-induced variation in a PSF are shown in Figure 3.3.

The effective variations in PSFs were largest at lower FRD values and decreased at higher FRDs. One of the most notable trends in these residual data was the dipole-like structure of the residuals, especially between low FRD images. The dipole structure indicated the possibility of a shifting centroid. One of the dominant effects of changing FRD, as a result, is effectively shifting the centroid of the PSF in the direction of the positive residual. Indeed, figure 3.4 demonstrates that centroid offsets generate the same kind of residual as observed in figure 3.3. However, one would expect pure FRD to impose a Gaussian convolution on the light profile. A simple Gaussian convolution incurs no centroid shift, yet we observe a shift in the test images. This illustrates some of the complexity between mapping FRD from the fiber/pupil and the PSF.

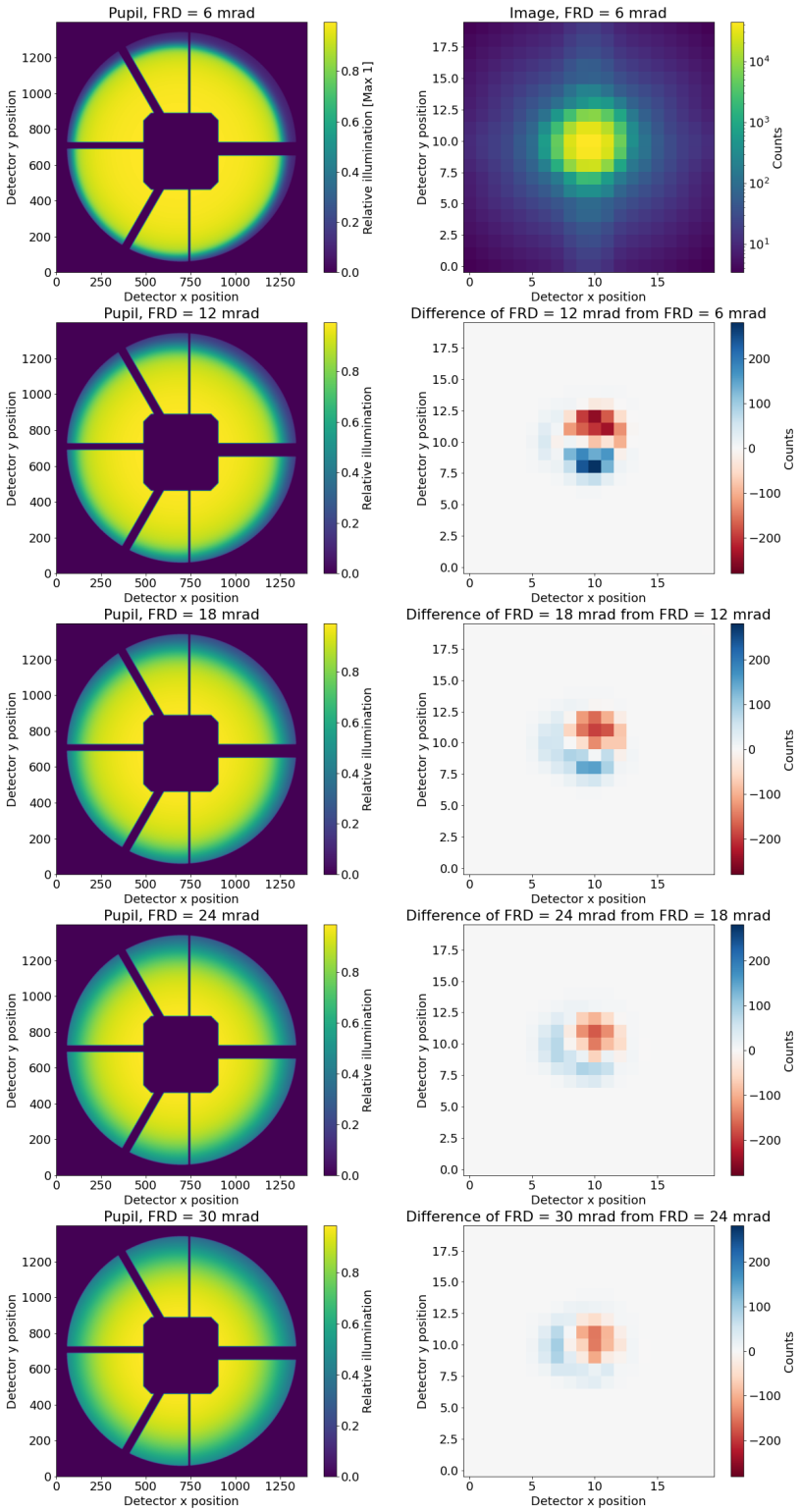

Figure 3.3 This figure demonstrates the pupil image of input light in the left column, the central 20×20 pixels of the in-focus image in the top of the right column, and 2d residuals between in-focus images at adjacent rows' FRD values in the rest of the right column in steps of 6 mrad. The residuals display how increasing FRD adjusts the PSF in the spectrograph, with a maximum fractional change of 9% a few pixels from the center at the 6-12 mrad FRD transition. The dipole-like residuals indicate a possible centroid shift.

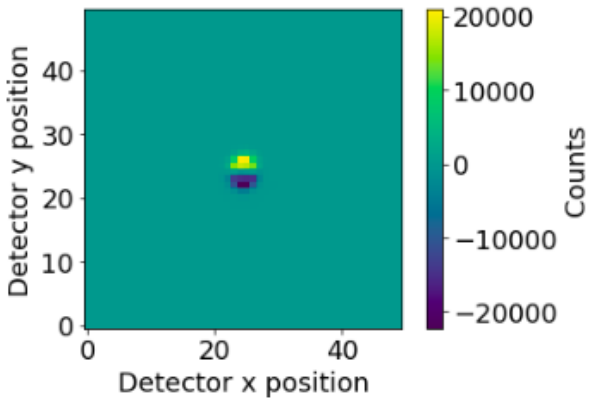

Figure 3.4 Residual generated by subtracting the in-focus spectrograph image from the center of the spectrograph with 6mrad FRD by the same image except offset by one pixel vertically. The residual output generates a dipole structure similar to that as seen in Figure 3.3

However, since the direction of the dipole differs depending on the fiber considered (that is, the FRD effect was not strictly along any specific direction), only the magnitude of the shift in the centroid could be compared to this result. Since other instrumental effects may cause variations in the centering of the image as well, this metric was not found to be satisfactory in extracting out the actual FRD. In particular, line modeling will be done relative to each line's centroid rather than a specific location in the detector. Therefore, a similar analysis was conducted while holding centroid constant. Thus, we reevaluated the effect of FRD when PSFs were adjusted to have the same centroid to determine the relative changes FRD caused in the PSF. Figure 3.5 demonstrates how realigned images respond to changing values of FRD. The absolute magnitude of the residuals decrease (from 14 counts to 4 per few hundred in the maximum amplitude pixels), especially for low values of FRD. This result proves that centroid shifting dominated the FRD residual. At larger FRD, the residual decreases at the center of the PSF and increases in the wings, similar to the way FRD redistributes flux in the pupil image.

Two primary takeaways from the 2D analysis are 1) the dominant effect of FRD on PSF is centroid shift, especially at lower FRD, and 2) the magnitude of FRD variation after correcting for centroid shift is relatively constant (2-4 per few hundred counts) with increasing FRD but becomes more structured at higher FRD.

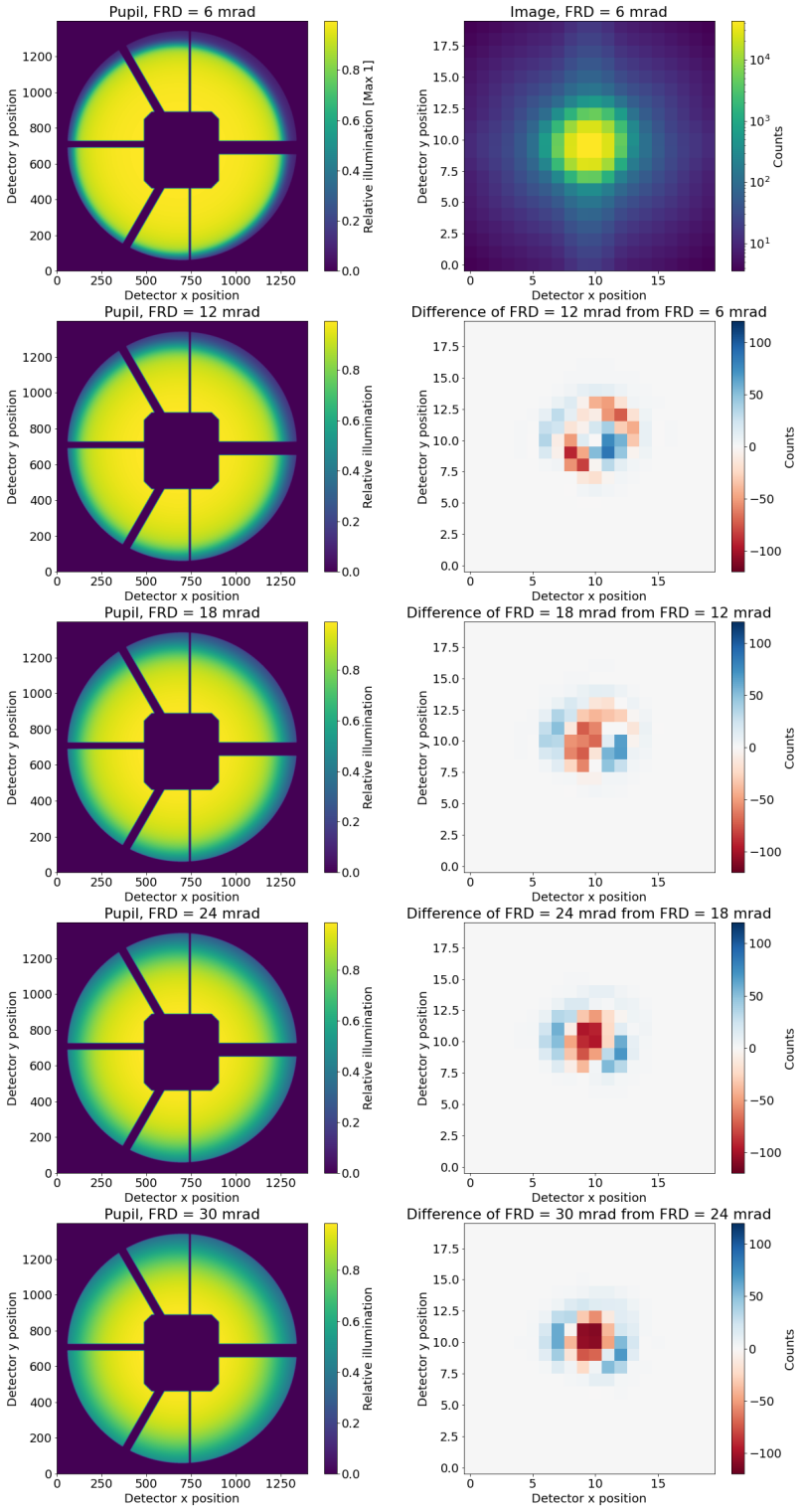

Figure 3.5 This figure demonstrates the same data as Figure 3.3 except that each image is aligned to have the same centroid. The residuals display how increasing FRD adjusts the PSF in the spectrograph, on the order of 100 counts in a pixel. More notably, aligning centroids also removes the dipole-like structure of the residuals, though the low-FRD residuals are complex regardless. High-FRD residuals tend to be simpler with a decrease in flux at the center of the PSF and increase in flux toward the wings.

1D variation

After determining the effects that FRD has on the 2D PSF, we measured how the FRD increases manifested as differences in their corresponding PSFs' boxcar extractions. Each boxcar extraction was taken with 6 pixels in the horizontal direction about the centroid of the PSF, summing up the counts in each row, and then plotted across vertical direction. The difference between two boxcars taken at two separate FRD values is taken to be the effect FRD has on the 1D extraction. Figure 3.6 displays the boxcar extraction for the 2D PSF from the previous section (centroid-aligned) along with residuals between the boxcar extractions.

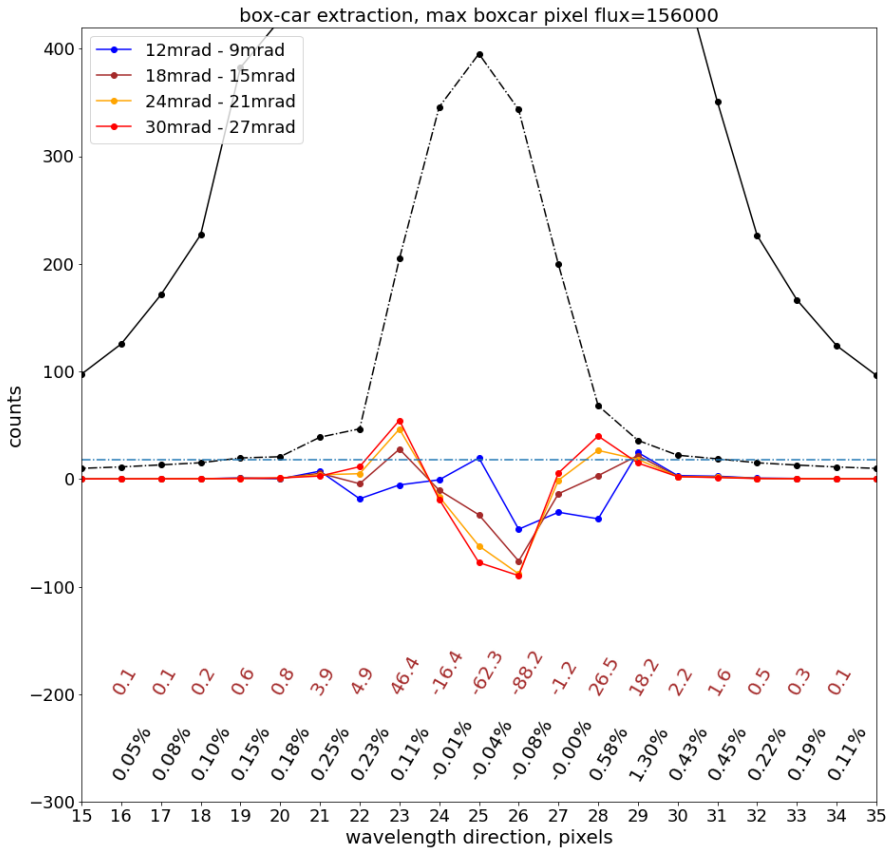

Figure 3.6 Result of a 1D boxcar extraction in the wavelength direction of an example 2D PSF (solid black line) and residuals when FRD is changed (colored solid lines). Numbers along the bottom of the image indicate the counts in the residual between 21 mrad and 24 mrad FRD (yellow) and corresponding percent variation in that pixel from the full boxcar extraction of the lower FRD spectrum (21 mrad). Additionally, noise level for Poisson noise (black) and read noise (cyan) are shown in dash-dotted lines. Read noise assumes the value of the read noise and scattered light (variance of 40 $counts^2$) measured from test LAM data. This measurement is an upper limit for each spatial pixel.

Two primary features are apparent when observing the 1D boxcar: 1) residuals at low FRD are complicated in structure but have low amplitude on average, whereas the residuals at higher FRD decrease at the center while increasing at the wings (which is expected from the 2D PSFs as in Figure 3.5), and 2) while the largest absolute residual is in the center of the line, the maximum percent variation is not large there due to the large number of counts. The largest percent variation in a pixel in figure 3.6 is 1.30% at a distance of 4 pixels away from the center of the line, towards the wings of the PSF. Thus, the largest effect of FRD would be expected to be in the wings of the 1D boxcar extraction rather than the center. Because FRD in this region is greater than the 0.5% sky subtraction goal for the PFS, it must be accounted for in modeling the PSFs. We aim to measure FRD in the next section 3.3.

3.3 Extraction of FRD from PSFs

Given the structural effects of FRD on the point spread function, we would like to properly fit for FRD when fitting a model to the PSF. Conceptually, this simply involves reversing the process of the previous section. However, effects from FRD such as centroid shift may occur due to other instrumental effects such as change in temperature.

However, even with a fixed centroid, noise complicates proper extraction. The purpose of this section is to describe the algorithm used to extract FRD. The algorithm used to approach this extraction process is available at `https://github.com/bbelland/FRDtesting`, but is heuristically explained below.

The algorithm takes as inputs a set of template PSFs with known FRDs, an array of the FRDs corresponding to those images, and the image to solve for FRD. The general approach to this algorithm is simple: minimize the residuals between model images generated at different known FRDs and the image with unknown FRD.

In practice, fitting a PSF to another PSF is not ideal because FRD reaches Poisson noise levels and that the brightness of the PSF falls off sharply. Instead, this algorithm weights residuals according to a ring around the center of the PSFs. The purpose of this weighting is to increase net signal by avoiding the center where the Poisson noise greatly dominates the FRD residuals and instead focusing on the area where the ring-like residual manifests in centroid-focused PSFs as seen in the previous section (as in Figure 3.5).

Weighted residuals with a χ^2 value less than 2 are kept as the uncertainty range for the resulting FRD, where the noise in the focused region is on the order of the

FRD-like residual.

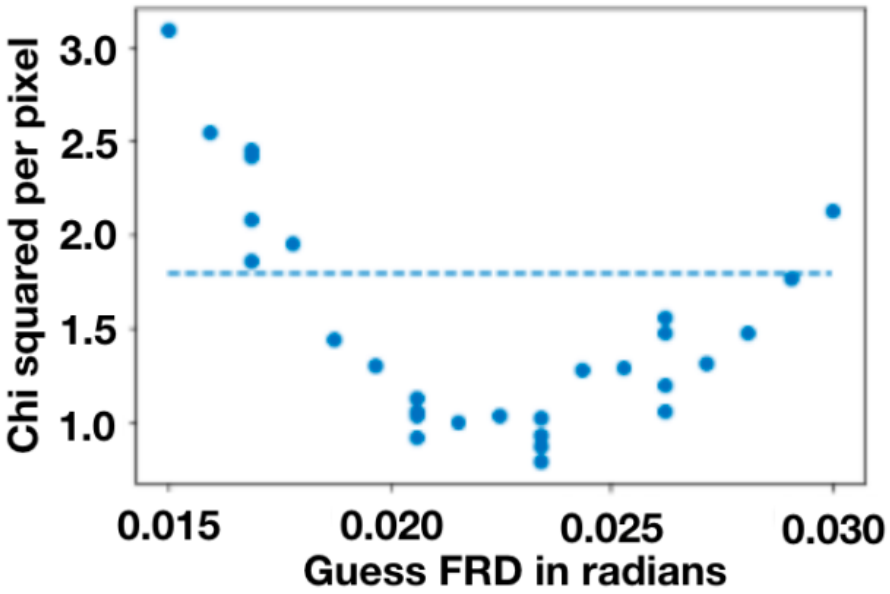

Figure 3.7 Example chi squared per pixel value calculated from the FRD residual minimization algorithm in its current state as a function of the "guess FRD" input into the algorithm (input FRD of 0.023 radians). The dotted horizontal blue line is the minimum chi square in the solution plus one.

The structure of PSFs across the detectors has a strong dependence on position in the detector due to differing wavefronts. Thus, while each point can have an FRD extracted from it, the uncertainties for each extraction depends on location on the detector, as shown in Figure 3.8. Notably, there are low ~ 2 mrad uncertainties toward the center of the detector, where the PSF structure is most circularly symmetric, and larger uncertainties toward the edges of the detectors.

Discussion

While the large uncertainties at the edges of the detectors may be concerning at first, note that all PSFs at a given x coordinate (that is, along the same column) are from the same fiber. In practice, each PSF from the same fiber has the same FRD, so these points can be used to reduce the uncertainty in the FRD extraction when fit for simultaneously. Thus, the overall FRD uncertainty can be reduced from the values seen from one-PSF fits.

Currently the code is dependent on the user inputting a smart spacing for the code to interpolate and solve for a minimum. While there are checks incorporated to make sure that the output minimum is reasonable, incorporation of a method to

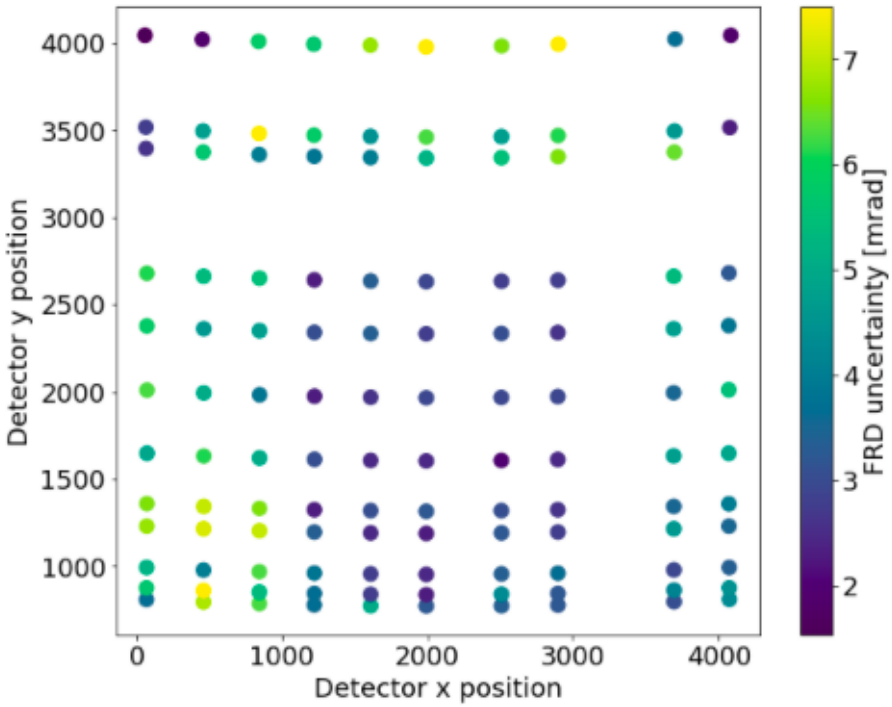

Figure 3.8 Uncertainty in FRD extraction at varying locations (and thus varying wavefronts) across the detector. Uncertainties grow largest towards the edges of the detector but approach 2 mrad toward the center.

measure the gradient toward the minimum would help to determine if sampling is good enough to resolve the minima properly.

3.4 Conclusion

Focal ratio degradation, the broadening of light traveling through a fiber due to its imperfections, is one of the complications that must be dealt with in order to fully harness the strengths of fiber spectrographs. The variation of FRD due to changing stresses on fibers is an important aspect to understanding the PSFs in the spectrograph. However, it is especially important in the Subaru PFS when aiming for its 0.5% sky subtraction residuals.

From the 2D variations of PSFs generated from the PSF's 2D-DRP, the dominating effect of FRD on the PSF was centroid shift. Even when the centroid shift is accounted for, increasing FRD moves flux from the core of the PSF toward the wings. This feature is less prominent at very low FRD, but in the 20–30 mrad range this ring feature dominates the 2D residual.

After investigation of the 2D residuals, 1D boxcars were taken to understand the

effect on spectra. While the absolute variation in PSF is maximized at the center of the line, the largest fractional change in the PSF manifests in the wings 3–5 pixels from the center of the line. 3 mrad FRD changes cause a change on the order of 1% in the boxcar extractions in the wings. Over long or coadded exposures, the FRD will have an effect comparable to the goal of 0.5% sky subtraction.

An extraction algorithm was proposed and briefly tested against simulated PSFs with noise added, returning the model FRDs in 50000-peak-count PSFs with errors of 2 milliradians toward the center of the detector. In future work, using the fact that one fiber will have multiple lines at different wavelengths but with the same intrinsic FRD, the error on FRD can be reduced further.

Chapter 4

NGC 6822 AS A PROBE OF DWARF GALACTIC EVOLUTION

Belland, Brent et al. (Nov. 2020). "NGC 6822 as a Probe of Dwarf Galactic Evolution". In: *Astrophysical Journal* 903.1, 10, p. 10. DOI: 10.3847/1538-4357/abb5f4. arXiv: 2009.04555 [astro-ph.GA].

Abstract

NGC 6822 is the closest isolated dwarf irregular galaxy to the Milky Way. Its proximity and stellar mass ($10^8 M_\odot$, large for a dwarf galaxy) allow for a detailed study of its kinematic properties. The red giant branch (RGB) stars at the galaxy's center are particularly interesting because they are aligned on an axis perpendicular to the galaxy's more extended H I disk. We detected a velocity gradient among the RGB population using spectra from Keck/DEIMOS. This rotation is aligned with the H I disk, but the sense of rotation is about the major axis of the central RGB population. We measured the rotation velocity (v) and velocity dispersion (σ) of the RGB population in five metallicity bins. We found an increase of rotation support (v/σ) with increasing metallicity, driven primarily by decreasing dispersion. We also deduced an increasing radial distance for lower metallicity stars at -0.5 kpc/dex by relating the observed stellar kinematics to position via NGC 6822's H I velocity curve. While the inverted metallicity gradient-like could be interpreted as evidence for an outside-in formation scenario, it may instead indicate that stellar feedback disturbed a centrally star forming galaxy over time.

4.1 Introduction

There is a broad set of morphologies that describe massive galaxies (Sandage, 2005). Perhaps the best known morphology difference is between spiral and elliptical galaxies, as in Hubble's classification system (E. P. Hubble, 1926). This visual distinction informs us about some of the physical properties of these galaxies: spiral galaxies contain neutral and ionized gas, actively form stars, and rotate, whereas elliptical galaxies are old, gas-poor, quiescent, and supported by random motion (i.e., dispersion).

Galaxies obey a morphology density relation (Postman and Geller, 1984). In denser environments, the population fraction of spiral galaxies decreases and the fraction of elliptical galaxies increases. This relation points to the formation mechanism of elliptical galaxies: in denser galactic environments, the spiral galaxies begin to merge. These mergers cause gas loss, star formation, and disruption of the rotation support. The result is the transformation of a spiral galaxy into an elliptical galaxy.

For dwarf galaxies, there is a parallel between the spirals and ellipticals. Dwarf irregulars are analogous to giant spirals because they are gas-rich, rotating, and star-forming. Dwarf spheroidals are analogous to giant ellipticals because they are gas-poor, dispersion-supported, and quenched. Dwarf galaxies also obey their own morphology–density relation. A dwarf galaxy's morphology correlated with the distance to its host galaxy. As found by Spekkens et al. (2014), dwarf galaxies within the Milky Way (MW) viral radius are predominantly gas-poor (i.e., dwarf spheroidal, dSph) while those just outside the MW viral radius are primarily gas-rich (i.e., dwarf irregulars, dIrr).

(Mayer et al., 2001) proposed a mechanism, called tidal stirring, to describe this morphology density relation. Successive pericentric passages near the MW can tidally disturb a dIrr. The ram pressure stripping and tidal influence of the MW cause angular momentum of the galaxy's gas to flow outward. Then, the angular momentum is carried away when the outlying stars and gas are stripped from the galaxy. The loss of rotation and gas thus transitions the dIrr to a dSph and can explain the morphology–density relation.

However, in practice, the "rotation support" (ratio of rotation velocity divided by velocity dispersion) of the old populations in dIrrs is almost uniformly low and consistent with no rotation. This quality holds for both observed galaxies and galaxies simulated by the Feedback in Realistic Environments (FIRE, Hopkins et al., 2014) code (Wheeler et al., 2017). This is not a surprise for the dSphs, which

are dispersion-dominated, but dIrrs are usually presumed to form with rotation. Kaufmann, Wheeler, and Bullock (2007) note that, due to their lower mass, dwarf galaxies are more affected by pressure support from gas temperature, which causes them to be less disky and less rotation-supported than their more massive counterparts. Nonetheless, some dIrrs clearly have rotating gas disks (e.g., Iorio et al., 2017). What removes the rotation support from a dwarf irregular if not tidal stirring?

One of the most accessible dwarf irregular galaxies to study is NGC 6822. NGC 6822 is about 500 kpc from the MW, making it the nearest isolated dIrr. It is relatively massive, with $10^8 M_\odot$ in stars and a similar mass of H I gas (McConnachie, 2012). Its large angular extent (about 1.2°) permits studies at high angular resolution. Spectroscopic studies enjoy the luxury of choosing individual stars and achieving high S/N for each star observed.

NGC 6822 has many interesting properties that contain clues about its history. NGC 6822 has an optically bright center, often referred to as a bar due to its elongated shape (Gallart et al., 1996). As a result, NGC 6822 is classified as an irregular barred dwarf galaxy (G. de Vaucouleurs, A. de Vaucouleurs, and Corwin, 1976). Although the classification of the bar is based simply on the galaxy's visual appearance, Valenzuela et al. (2007) raised the possibility that the central stellar population is a dynamical bar. However, there is also an H I disk that runs normal to this bright optical center de Blok and Walter (2000). Ongoing star formation closely follows the shape of the disk (Komiyama et al., 2003). There also is an older/intermediate-age stellar population associated with NGC 6822 that extends much farther than the bright optical center and does not follow the disk (Letarte et al., 2002; Thompson, Ryan, and Sibbons, 2016).

On top of the stellar population distributions, the H I gas disk has unique properties that are worthy of mention. There is a large H I hole and in the southeast of the galaxy and a H I overdensity in the northwest of the galaxy (de Blok and Walter, 2000). de Blok and Walter (2000) noted that the southwest of NGC 6822 had a tidal arm feature, indicating a previous interaction history. They estimated that the H I hole had a relatively short kinematic age of 100 Myr, which could be correlated to the tidal arm feature if such an interaction increased the star formation rate. Noting the asymmetrically large mass distribution in the northwest of NGC 6822, they calculated a similar interaction timescale of 300 Myr if the overdensity in the northwest were a merger that had disrupted the southeastern hole, leading to a prediction that the northwest cloud was a companion galaxy. de Blok and Walter

(2006) expanded on this interpretation, finding that the cloud was distinguishable from the rest of NGC 6822 in velocity and would have a dynamical mass ratio consistent with a dwarf galaxy merger. However, Cannon et al. (2012) later found that the putative companion had a similar star formation history as the rest of NGC 6822 and no old star overdensity or metallicity difference relative to the expected value from NGC 6822 at its distance. The stellar population was thus inconsistent with dwarf galaxy merger, even though they did not rule out a H I cloud.

This paper addresses the formation history of NGC 6822 by analysis of the kinematics of the old, central population of stars. Section 4.2 presents the already-published spectra and velocity measurements. Section 4.3 gives our measurements of rotation and velocity dispersion in different bins of stellar metallicity. We interpret these trends in Sec 4.4, and we summarize in Section 4.5.

4.2 Data

Kinematic data for NGC 6822 stars comes from the observations of Kirby, Cohen, et al. (2013). 299 stars between two slitmasks were observed in the Keck II telescope's Deep Imaging Multi-Object Spectrograph (DEIMOS, Faber et al., 2003) with total exposure times of 8.7 and 6.0 hours. The color–magnitude diagram of stars in the Kirby, Cohen, et al. data is recreated in Figure 4.1.

Previous analysis of NGC 6822 by Kirby, Bullock, et al. (2014) indicated that rotation might be present in NGC 6822 on the order of 10 km/s, but a definitive detection of rotation was uncertain due to the high velocity dispersion of 23.2 ± 1.2 km/s. Thompson, Ryan, and Sibbons (2016) later found rotation in carbon stars in a more extended population at 11.2 ± 2.1 km/s with a position angle of $26 \pm 13°$. A similar rotation was also found in the gas (for example, see Weldrake, de Blok, and Walter 2003).

The red giant branch star selection was done by selecting stars within a brightness, color, and isochrone cutoff. Target selection was completed using photometry data from Massey, Olsen, et al. (2007). In this paper, the ages of stars are inferred from the metallicity of the stars, which itself is highly correlated with color. Therefore, any color cutoffs used in the star selection will impact the age/metallicity range considered. Stars with extinction-corrected magnitudes between 19.0 and 21.6 were selected based on the expected brightness of red giants at a distance modulus of 23.40 (479 kpc) (Feast et al., 2012). We applied a constant reddening correction of $E(B-V) = 0.25$ (Massey, Olsen, et al., 2007). Stars beyond the colors between

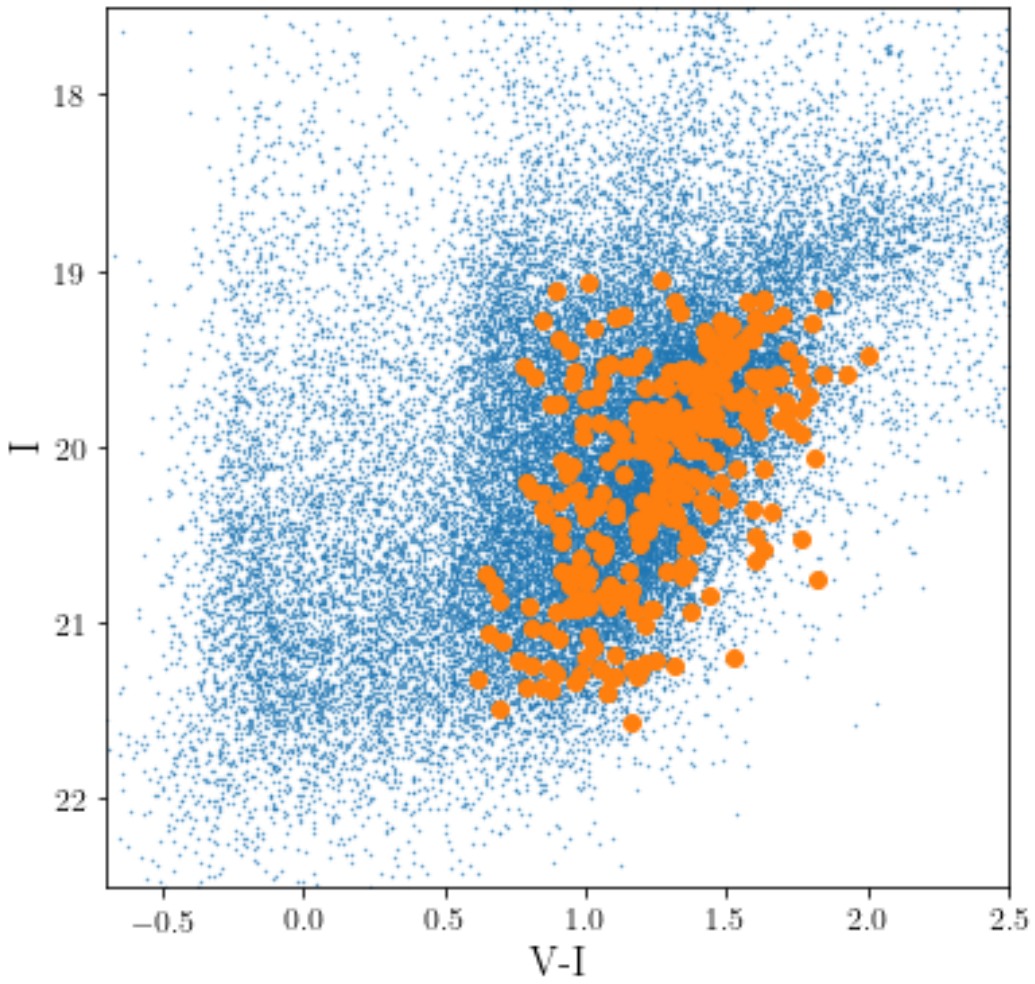

Figure 4.1 Distribution of stars (orange) from Kirby, Cohen, et al. (2013) in color–magnitude space plotted with photometry (blue) from Massey, Olsen, et al. (2007).

$0.6 < (V - I)_0 < 2.5$ were excluded based on the expected colors of red giants. Yonsei–Yale isochrones in V and I filters ranging from the bluest (2 Gyr, $[Fe/H] = -3.76$) to the reddest (14 Gyr, metal-rich $[Fe/H] = +0.05$) bounded the selection in the color–magnitude diagram. In cases where multiple stars competed for the same slit, priority was placed on stars closest to a 6 Gyr, $[Fe/H] = -1.05$ isochrone.

Especially since this study relies on observing stars with a span of metallicity/ages, it is important to determine possible observation bias. The selection of red giant branch stars in (Kirby, Cohen, et al., 2013) was designed to be as inclusive as possible: the large isochrone metallicity range of -3.76 to +0.05 and large isochrone age range of 2-14 Gyr is expected to not reject any red giant branch star, thus not

biasing the metallicity range of the stars in the sample. Due to the priority function increasing towards the intermediate age and metallicity isochrone, however, there may be a slight bias toward observing these intermediate age and metallicity stars. This bias is not expected to significantly affect the analysis in this paper, as while the priority function does complicate analysis of the metallicity bias selection, it only effects the uncommon cases where multiple stars were possible candidates for the same slit.

The stellar kinematics in a galaxy encode an important part of a galaxy's history. Stars are probes of the galactic structure as they travel through the galactic potential over time. Disruptive events such as mergers or substructure such as tidal streams can be tracked by following stellar groups that are distinct in metallicity and velocity space. Rotation is commonly a criterion referenced to distinguish between dwarf spheroidal and dwarf irregular galaxies with dwarf spheroidals expected to have undergone a significant morphological transition (Mayer et al., 2001).

We examine the kinematics of NGC 6822 through existing measurements of the radial velocities of red giants (Kirby, Bullock, et al., 2014). Because Kirby, Bullock, et al. restricted their measurements to red giants, our study is sensitive to stellar populations older than $\sim$ 1 Gyr. Younger stars, like blue and red supergiants and stars on the upper main sequence, are not present in our sample. Furthermore, the sample is restricted to the central region of the galaxy. Specifically, the measurements are confined to an approximately rectangular region with an area of about $8' \times 15'$. The red giant population extends significantly beyond this region (Cannon et al., 2012).

4.3 Results

Prolate rotation

Figure 4.2 presents the map of radial velocities of red giants in the center of NGC 6822. Despite the large scatter in stellar velocities, there is a clear velocity gradient across NGC 6822, which shows that the red giant population is rotating. The magnitude of this rotation is about $\pm$10 km/s, which is about half of the velocity dispersion of these stars (Kirby, Bullock, et al., 2014). The ratio between the rotation velocity and velocity dispersion indicates the balance of different mechanisms that support the galaxy against gravity. This ratio is about 0.5 for these stars but notably greater than zero.

This nontrivial rotation of the old red giant branch (RGB) stars in Figure 4.2 is around the major axis of the innermost RGB stars, as estimated from Figure 8 of

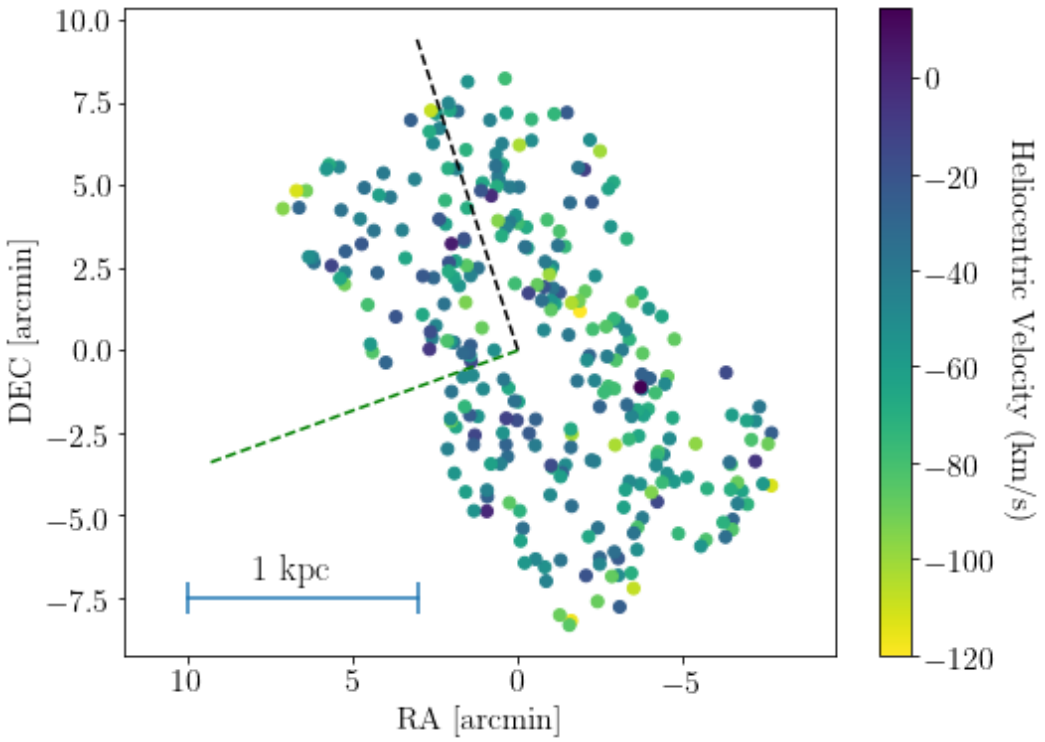

Figure 4.2 Distribution of stars from Kirby, Cohen, et al. (2013), color-coded by heliocentric velocity, with dark blue corresponding to least rapidly approaching and light yellow corresponding to most rapidly approaching. The dotted black line indicates an approximate position angle of the major axis of RGB stars estimated from the RGB isophotes in Figure 8 of Cannon et al. (2012) (18 degrees), while the green line indicates the approximate position angle of the major axis of H I disk from Weldrake, de Blok, and Walter (2003) (110 degrees). The velocity gradient apparent from west to east indicates rotation, prolate in the sense of the RGB stars and oblate in the sense of the H I disk. Coordinates are in units of arcmin relative to the center of NGC 6822 (McConnachie, 2012). The angular size of 1 kpc is shown in the bottom left for reference; NGC 6822 extends 5 kpc in either direction along the H I major axis and about 1 kpc in either direction along the RGB isophote major axis.

Cannon et al. (2012). (Battinelli, Demers, and Kunkel (2006) observed a position angle of about 65° for RGB stars that extend for the entirety of NGC 6822. This angle does not represent the RGB stars in the central core of the galaxy.) Rotation about a major axis is an uncommon phenomenon; most rotation is about a minor axis, such as a spiral galaxy rotating around its minor axis rather than twirling like a flipped coin through space. In fact, prolate rotation is so unusual that it has even been invoked as possible evidence of a merger history for the Andromeda II (Ho

et al., 2012) and Phoenix (Kacharov et al., 2017) dwarf galaxies.

If NGC 6822's RGB stars are prolately rotating, this may thus be evidence that NGC 6822 has experienced a merger in its past. This would not be the first time a merger history has been considered for this galaxy; de Blok and Walter independently proposed a merger history for NGC 6822 due to its morphology and jump in H I disk velocity.

The apparent prolate rotation of the RGB stars is informative even if there was not a merger in NGC 6822's past. If NGC 6822's old population is prolately rotating due to internal processes rather than external mergers, then a dwarf irregular like NGC 6822 could transition into a prolately rotating dwarf spheroidal from just removal of its gas. Wheeler et al. (2017) similarly argued that the low rotation support of the RGB star population in dIrrs could mean that transitioning to dSphs could be done simply by gas removal.

However, the rotation of the RGB stars as seen in Figure 4.2 is not just around their own major axis, but also along the major axis of the H I disk (Weldrake, de Blok, and Walter, 2003). Rotation about the same axis as the H I disk makes sense if the RGB stars initially formed from the gas in the disk. However, as the distribution of the central RGB stars doesn't resemble that of the disk, it is apparent that there is a driver of morphological change between the disk and the central RGB stars.

Understanding this transition will help in understanding how dwarf galaxies like NGC 6822 evolve over time.

Kinematics evolution

There is clearly a change in the kinematic character between the H I disk and the RGB stars, so the galaxy must have evolved over time. However, how does this transition occur? Was it sudden, such as from a quick merger, or an internal process over a long period of time?

One common diagnostic of the kinematic evolution of a galaxy is an age–velocity dispersion relation (AVR) (for an example, see Leaman et al. 2017). In order to approach this problem similarly, we also need to measure the ages and velocity dispersion of our sample of stars.

By classifying stars by age and determining how their kinematics vary as a function thereof, we can probe the transition between the effectively zero-age population of the galaxy (H I gas) and the oldest stellar population of RGBs. One effective method

for characterizing ages of stars is to calculate their metallicities: because galaxies increase in metallicity over time, stars with lower metallicity also tend to have been formed earlier. The correlation between age and metallicity can be complicated by stellar migration, as stars forming in separate regions with differing metallicity growth can be mixed by migration, creating metallicity differences in local populations independent of age. While outside the scope of the paper, determination of alpha-to-iron abundances in stars can disambiguate the formation environment of a star from age evolution, which would reduce uncertainty in this correlation. In the case of NGC 6822, (Wyder, 2001) found that metallicity is very nearly monotonic with age (Figures 19–22), adding reassurance that metallicity as a proxy for age is a valid assumption.

In addition to age, velocity dispersion information must be considered. Perturbations to a star's orbit are encoded in its velocity dispersion, which gives information about the rotational support of the gas these stars formed from. Alternatively, the star's orbit can be shaped by disruptive events (kinematic collisions or mergers) or a disruptive potential of the host galaxy. In order to conserve total energy, dispersion of a population also increases if rotation velocity decreases. Given this relation between dispersion and rotation, the ratio of rotational velocity divided by velocity dispersion can be used to understand how the rotational support changes between the gas and stars.

In order to calculate rotational velocity and velocity dispersion as a function of time, each of the j stars with metallicities within a given range (quintile of [Fe/H]) were grouped together in a bin. Within each of the k bins, velocity dispersion σ within each bin was determined from the line-of-sight velocities v and uncertainties ϵ from finding the maximum of the likelihood function L_k (as in Wheeler et al. 2017):

$$L_k = \prod_{j=1}^{N} \Bigg(\frac{1}{\sqrt{2\pi(\sigma_k^2 + \epsilon_j^2)}} \times \exp\left[-\frac{1}{2} \frac{(v_j - (\bar{v} + v_{rot,k} \cos(\theta_k - \theta_j)))^2}{\sigma_k^2 + \epsilon_j^2} \right] \Bigg), \tag{4.1}$$

where $\bar{v}$ is the mean velocity of all stars in the galaxy, θ_k is the angle of the rotation axis for a bin, v_j is the line-of-sight velocity of star j belonging to bin k, and θ_j is the angle from the center of the galaxy to that star.

From the exponential of equation 4.1, the velocity rotation model adopted for a star is the average velocity plus a constant rotation velocity ($v_{\mathrm{rot},k}$) multiplied by an angular projection from the direction of rotation. Wheeler et al. (2017) found that the constant rotation model with just parameter v_{rot} was preferred to their pseudo-isothermal sphere model and is thus used here.

The product in Equation 4.1 combines all of the fits for each star to maximize simultaneously. The free parameters are the $v_{\mathrm{rot},k}$, σ_k, $\bar{v}$ and θ_k. They were found through maximum likelihood using an MCMC with a Metropolis algorithm and 10^5 links in the chain. A burn-in period of 10^3 links was discarded from the beginning of the chain. This burn-in was found by visual inspection to be sufficient to decouple the chain from the initial choices of free parameters.

With the velocity and metallicity data, plotting the metallicity versus $v_{\mathrm{rot},k}/\sigma_k$ ("rotation support") in each bin results in Figure 4.3. Notably, there in an increase in the rotation support in NGC 6822 with increasing metallicity, which corresponds to an increased rotation support for younger stars. This behavior is expected if the RGB stars were disrupted from a rotationally dominated disk, or if the rotation support grew over time.

4.4 Discussion

The evolution of kinematics with metallicity is a tracer of how the galaxy evolved over time, assuming that metallicity increases monotonically with time. However, separating out separate age populations also has a benefit of probing the gravitational potential of a galaxy with separate populations that have their own kinematic properties. Walker and Peñarrubia (2011) effectively utilized this property by extracting out enclosed mass from two independent chemodynamic populations at two separate radii from the Fornax and Sculptor dwarf spheroidal galaxies. Although the two populations trace the same underlying potential, they have separate velocity dispersions and separate physical sizes. Therefore, these two measurements of enclosed mass reveal the slope of the enclosed mass profile. This mass slope can be used to distinguish between cuspy and cored mass profiles, which itself distinguishes between models of galaxy formation (e.g., Navarro, Frenk, and White, 1996; Navarro, Frenk, and White, 1997; Mashchenko, Wadsley, and Couchman, 2008). Thus, it is clear that the kinematics within multiple-age populations is a powerful probe of galactic evolution.

NGC 6822 has increasing rotation support with increasing metallicity (Figure 4.3).

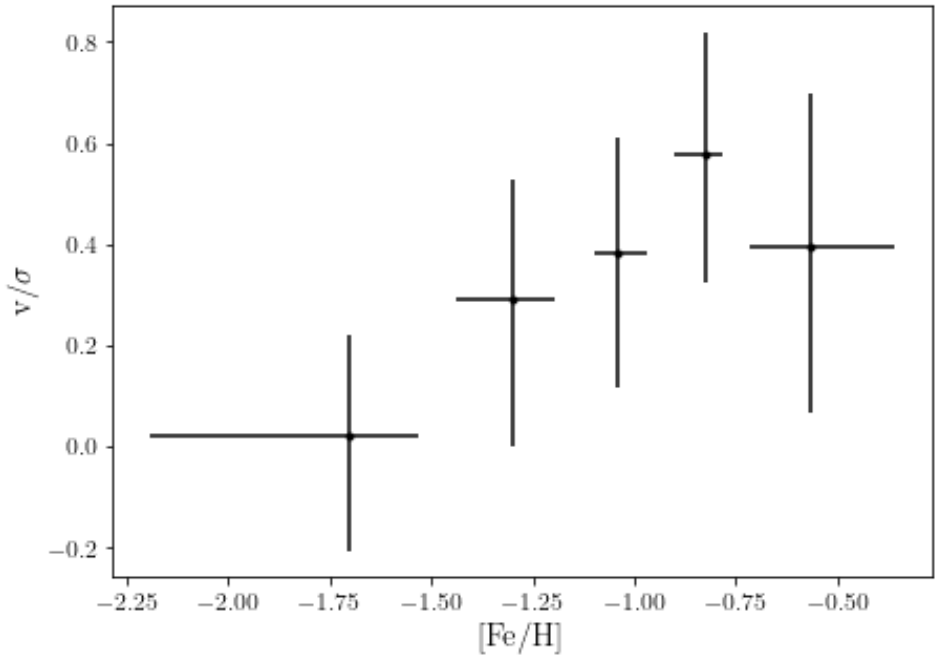

Figure 4.3 Metallicity versus rotation support (rotational velocity divided by velocity dispersion) for stars in NGC 6822 separated into five equal-number bins. The errors bars represent 68% confidence intervals. The upward trend in rotation support with metallicity indicates that younger stars are more rotationally supported in NGC 6822. This information is included in the summary of Table 4.1.

However, the large uncertainties due in part to the weak rotation and the large velocity dispersion obfuscate any detailed structure in the stellar rotation curve. To understand Figure 4.3 and the kinematics of NGC 6822 in more detail, we split the rotation support into contributions from rotation and from dispersion in Figure 4.4. Dispersion notably decreases with increasing metallicity, as noted by Swan et al. (2016). That study separated the galaxy into two populations: metal-rich and metal-poor. Our increased sample size allows us to split the galaxy into five metallicity bins. Our finer view of the evolution of dispersion shows that dispersion steadily decreases across a range of metallicity except for the most metal-rich bin.

The kinetic energy in any metallicity bin is a combination of the energy in rotation and energy in dispersion. We estimated the line-of-sight rotation velocity v_k using the likelihood function in Equation 4.1, but the rotation is in the plane of the galaxy, which is inclined relative to the observer. The in-plane rotation velocity is $\frac{v_k}{\sin i}$, and

rotational energy per unit mass is $\frac{1}{2}\left(\frac{v_k}{\sin i}\right)^2$. The inclination i of NGC 6822 is 60 degrees (Weldrake, de Blok, and Walter, 2003). The line-of-sight dispersion is σ_k also found from the likelihood in Equation 4.1.

Assuming dispersion is isotropic, kinetic energy per unit mass from the 3D velocity dispersion would be $3 \cdot \frac{1}{2}\sigma_k^2$ in a given bin. However, stellar kinematics are more affected by anisotropy for our centrally concentrated sample of stars compared to the whole stellar population. That is, if dispersion were only radial, line-of-sight dispersion at the center of the galaxy would encapsulate all energy in dispersion, which would be $\frac{1}{2}\sigma_k^2$. However, a primarily tangential dispersion would indicate that observations of line-of-sight velocities toward the center of the galaxy vastly underestimate the kinetic energy in the stars. To accommodate this uncertainty, we write kinetic energy in dispersion as $n \cdot \frac{1}{2}\sigma_k^2$, where $n = 1$ corresponds to a purely radial dispersion, $n = 3$ corresponds to isotropic dispersion, and $n > 3$ corresponds to more tangentially dominant dispersion.

For stars distributed over some radius $R_{\mathbf{max}}$, this kinetic energy is associated with the gravitational potential energy at the average radius, on the order of $\frac{1}{2}R_{\mathbf{max}}$. However, the exact value of radius depends on the system configuration and anisotropy. More specifically, Wolf et al. (2010) found that enclosed mass at the half-light radius scales as $3G^{-1}\sigma_k^2 r_{1/2}$. There is an enclosed mass dependence on velocity anisotropy, β which is minimized at the 3D (deprojected) half-light radius. In total, kinetic energy at a given metallicity is given by $\frac{1}{2}\left(\frac{v_k}{\sin i}\right)^2 + \frac{n}{2}\sigma_k^2$. The kinetic energy is plotted in Figure 4.5.

Unsurprisingly, the dispersion component dominates the weak rotation component, so the kinetic energy resembles the dispersion component of Figure 4.4. Since energy must be conserved but kinetic energy decreases with increasing metallicity, the effective potential energy per unit mass $-\frac{GM_{\text{enclosed}}(r)}{r}$ must be increasing with metallicity to balance this effect out. The radius r is measured from the galactic rotation axis, and $M_{\text{enclosed}}(r)$ is the total mass enclosed within this radius.

The total energy per unit mass is

$$\frac{1}{2}\left(\frac{v_k}{\sin i}\right)^2 + \frac{n}{2}\sigma_k^2 - \frac{GM_{\text{enclosed}}(r)}{r} < 0 \tag{4.2}$$

and by the virial theorem, twice the kinetic energy of the stars on average should equal the negative of the potential energy:

$$\left(\frac{v_k}{\sin i}\right)^2 + n\sigma_k^2 - \frac{GM_{\text{enclosed}}(r)}{r} = 0. \tag{4.3}$$

Changes in kinetic energy thus allow measurement of the change in average $-\frac{M_{\text{enclosed}(r)}}{r}$ between metallicity bins. Notably, the increase in $-\frac{GM_{\text{enclosed}(r)}}{r}$ with metallicity indicates that the average r of each population must decrease with increasing metallicity. That is, metal-rich populations are more centrally concentrated. Such a relation was predicted by Swan et al. (2016) and can be seen in the young versus old stellar population distributions of de Blok and Walter (2006).

Alternatively, the enclosed mass divided by radius can be independently determined from the H I gas velocity curve as a function of radius. A pseudo-isothermal velocity curve model used by Weldrake, de Blok, and Walter (2003) to model the H I velocity curve is shown in Figure 4.6. Combined with the enclosed mass vs. metallicity relationship (Figure 4.5), the spatial distribution of the different stellar populations can be probed. The inferred distributions for a purely stellar radial dispersion ($n = 1$) and isotropic dispersion ($n = 3$) are shown in Figures 4.7 and 4.8.

As qualitatively predicted earlier, more metal-rich star populations are found toward the center of NGC 6822, and more metal-poor stellar populations have larger effective radii. These observations are consistent with the outside-in star formation processes found in other dwarf galaxies, where star formation became more centrally concentrated over time. Alternatively, these negative metallicity gradients have been found to form in dwarf galaxies ($M_* \sim 10^{7-9.6}\ M_\odot$) by El-Badry, Wetzel, et al. (2016) and El-Badry, Quataert, et al. (2018) due to feedback from star formation that drives fluctations in the galactic potential. These perturbations cause kpc-scale migrations that cause older stellar populations to migrate outward and generate a negative metallicity gradient. Given that NGC 6822 neatly falls within this mass range, and due to its on-off star formation episodes (Wyder, 2001; Weisz et al., 2014) that correlate to this model, such an inside-out model may be preferred to explain the more radially extended low-metallicity population in NGC 6822.

The radial distribution of stars with metallicity is about −2 kpc/dex in the isotropic case and −0.5 kpc/dex in the radial dispersion case. The lower value is not surprising in the radial case because radial outflows would more efficiently disperse older stars over time. Furthermore, the distances required in the radial dispersion case are more realistic, being more closely confined the the center of the galaxy than in the isotropic case due to less total energy in the stellar populations. In fact, active star

formation histories in the centers of dwarf galaxies have been shown to induce radial anisotropy (El-Badry, Wetzel, et al., 2016). These calculated radii indicate a large radial isotropy consistent with an active star formation history. Such a process will be considered more in the next section.

Note that we averaged populations into metallicity bins, and we found the average radii of these bins. In other words, these measurements with units of kpc/dex indicate how populations at lower metallicities tend to be further away from the center of the galaxy. This quantity differs from a metallicity gradient (dex/kpc), which bins together stars at the same radius and then calculates average metallicity at each bin. That is, while the reciprocals of the calculated values indicate there is a negative metallicity gradient, which is considered in the rest of the analysis of this paper, they cannot be directly compared to metallicity gradients in NGC 6822 (e.g., Swan et al., 2016, who found that metallicity dispersion prevented a precise analysis).

Formation History

We can also consider why the metal-rich, young stars are more centrally concentrated. Unlike in spiral galaxies where star formation occurs in the arms rather than the center, the younger star distribution in NGC 6822 is centrally concentrated. However, many dSphs have been found to have centrally concentrated younger stellar populations.

One possibility for a negative metallicity gradient is that stars in NGC 6822 formed in a disk, but star formation in outer regions of the galaxy decreased more rapidly with time, due to reasons such as ionization of the outer H I disk (Kawata et al., 2006) or merely gas depletion. This can explain why dSphs stop forming stars in their outskirts first, yet the dwarf irregular NGC 6822 still has plenty of gas. This does not explain why the the youngest, most-metal rich stars are at a slightly larger radius than the second most metal-rich bin.

Another possibility is that a merger event occurred, funneling new gas toward the center of the galaxy while also relocating old stellar populations to larger radii. NGC 6822 has been speculated to have a merger event in its history, invoked by de Blok and Walter (2000) to explain NGC 6822's H I velocity curve. Such an event may be expected to bifurcate the stellar population, with separable old and young populations, whereas the observed metallicity gradient in NGC 6822 seems to be more continuous between bins. However, it may be possible for smaller mergers

over time to smooth out such a gradient (Benítez-Llambay et al., 2016).

One possible explanation for the distribution of the RGB stars appearing to rotate in a prolate sense is that these stars trace a dynamical bar along the line of sight. If such a bar existed, it would affect the dynamics of the rest of the galaxy, perhaps in a noticeable way. In a set of simulations by Friedli, Benz, and Kennicutt (1994), abundance gradients in barred galaxies were found to be flattened with a possibly metal-rich center. This prediction does not match with the the observed metallicity gradient for NGC 6822 (e.g. Figure 4.8), indicating that the RGB population may not occupy a bar. However other studies, such as Pérez, Sánchez-Blázquez, and Zurita (2009) and Zhuang et al. (2019), found a more complicated family of possibilities, with positive, zero, and negative metallicity gradients in barred galaxies. The negative metallicity gradients (corresponding to NGC 6822's case) were explained as originating from the disk not having enough time to flatten out. Such negative metallicity gradients also tend to correlate with positive age gradients (younger populations toward the center). This metallicity gradient relation is intriguing, but it does not appear to distinguish between other possible formation scenarios.

Radial migration of stars has also been used to explain metallicity gradients in galaxies: unordered radial migration may dilute an initially strong metallicity gradient. Radial migration can be induced by mergers, perturbations by companion galaxies, or galactic substructures. Loebman et al. (2016) were able to explain the varied metallicity distributions in the Milky Way as a function of radius by following radial migration in simulations. High-metallicity stars formed toward the center of the galaxy but migrated outward, enriching and skewing the outer radial metallicity distributions. In dwarf galaxies, an independent and dominant driver of radial migration may be induced by feedback during bursty star formation histories. El-Badry, Wetzel, et al. (2016) found that in $M_* = 10^{7-9.6}\ M\odot$ dwarf galaxies, feedback disrupting star formation in the center of the galaxy systematically drove out stars toward the galactic edges, creating metallcity gradients similar to that observed in our data for NGC 6822. Notably, such a high central star formation history would induce large, preferentially radial inflows and outflows of stars and gas during star formation bursts, which would also be consistent with the kinematic results of the previous section.

4.5 Summary

In conclusion, NGC 6822 is a promising candidate to study dwarf irregular populations and dynamics due to its mass and proximity. RGB archival data from Kirby, Cohen, et al. (2013) revealed a 10 km/s rotation in the center of the galaxy, approximately half that of the dispersion. This rotation is unusual in that it is prolate relative to the distribution of RGB stars, though it also matches the rotation of the H I disk. Due to the large number of stars and precise metallicity of the data, the rotation and velocity dispersion of the RGB population were measured in five metallicity bins. The kinematics across the bins were compared to the gas, which probes the same potential as the stars, to determine the radial extent of each population. A radial gradient of -0.5 kpc/dex (in the radial case) was found by relating the observed stellar kinematics to position via NGC 6822's H I velocity curve. Negative metallicity gradients are sometimes correlated with outside-in star formation in a galaxy. However, NGC 6822's multiple episodes of star formation may instead indicate that stellar feedback induced migration of preferentially older stars out of the center of the galaxy.

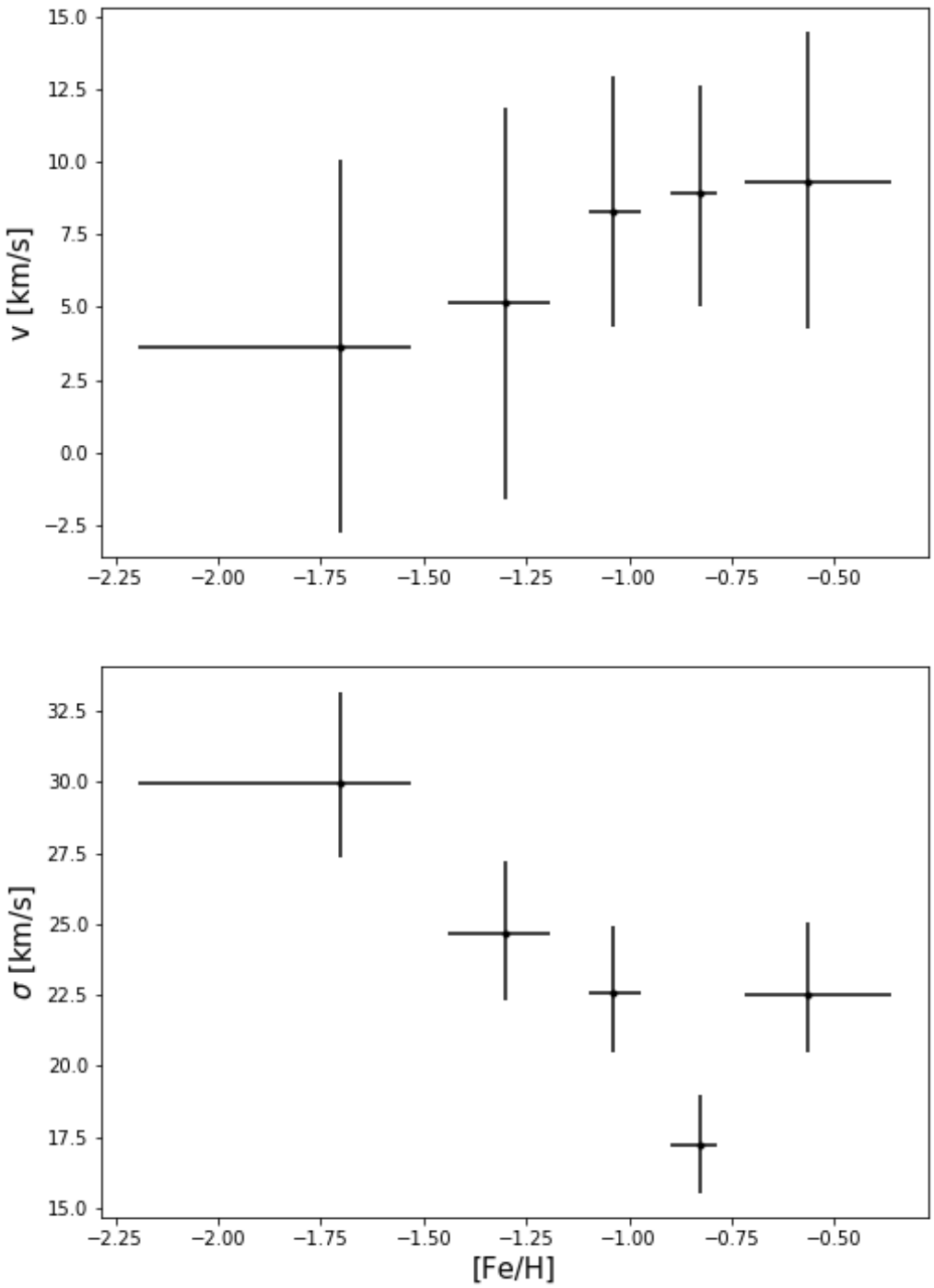

Figure 4.4 Top: Rotation velocity vs. metallicity. Bottom: Velocity dispersion vs. metallicity. Taken together, the rotation velocity and velocity dispersion are the components of Figure 4.3. The velocity dispersion change is more significant than the rotation velocity. The errors bars represent 68% confidence intervals. The upward trend in rotation support with metallicity indicates that more metal-rich, presumably younger stars are more rotationally supported in NGC 6822. This information is included in the summary of Table 4.1.

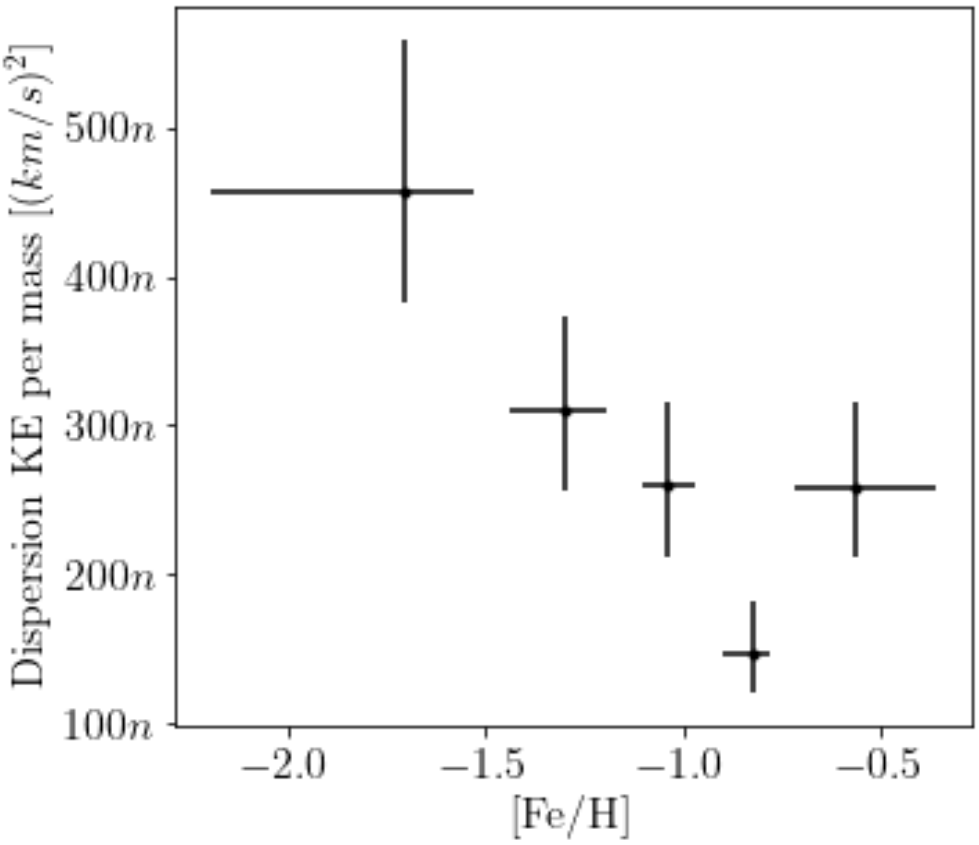

Figure 4.5 Kinetic energy in dispersion per unit mass of stars in each metallicity bin. The kinetic energy trends in the same way as the dispersion (see Figure 4.4) because dispersion dominates over rotation. The variable *n* quantifies uncertainty in anisotropy (see text). Notably, kinetic energy is not constant with metallicity. This information is included in the summary of Table 4.1.

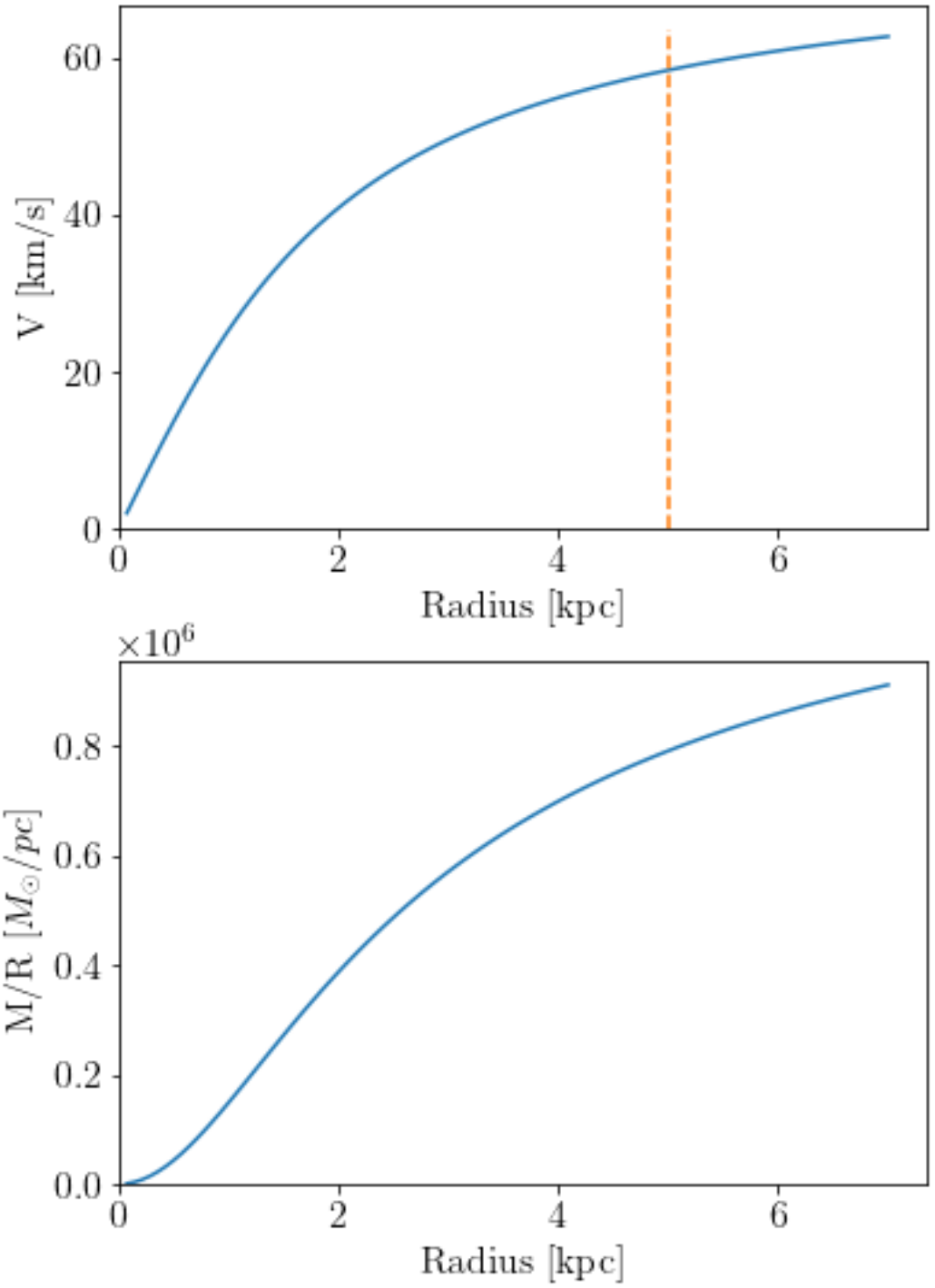

Figure 4.6 Top: Approximate velocity versus radius from the B24 minimum disk model of Weldrake, de Blok, and Walter (2003). The dotted orange line indicates the radial limit of the Weldrake, de Blok, and Walter (2003) data, with an extension from the pseudo-isothermal model in velocity beyond this value. Bottom: Conversion to enclosed mass divided by radius as a function of radius (i.e., Equation 4.3 where $\sigma_k = 0$).

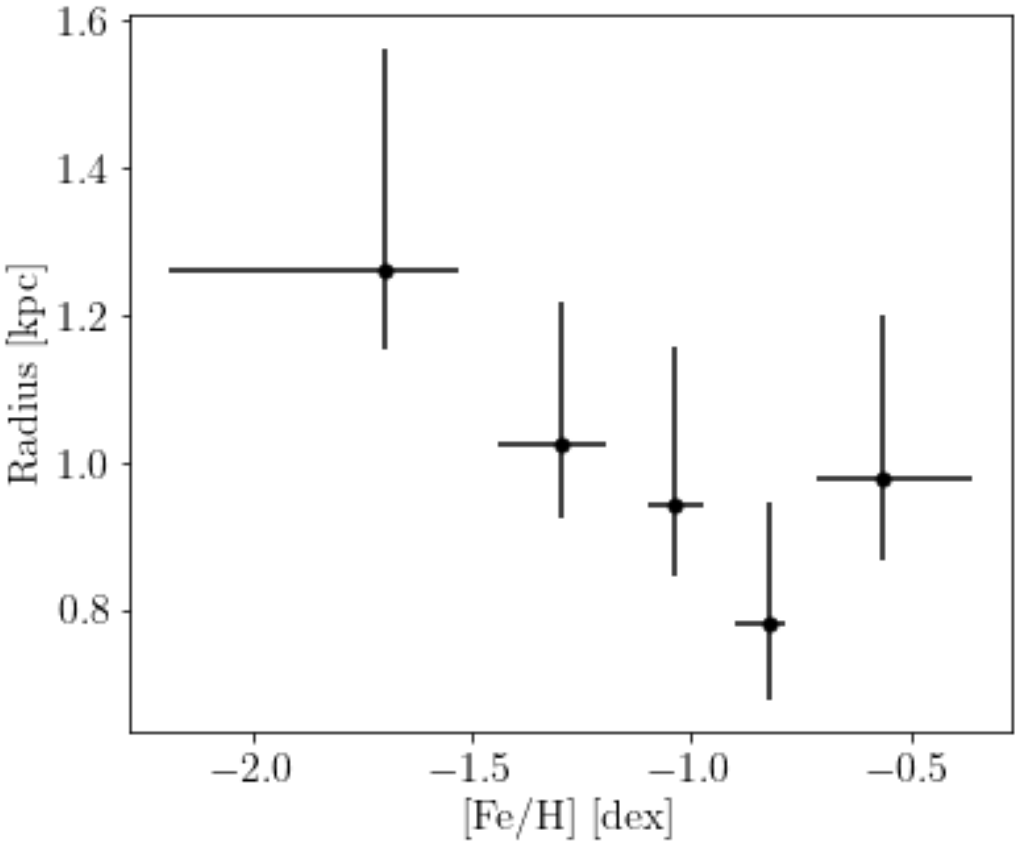

Figure 4.7 Radius vs. Metallicity, combining the enclosed mass vs. metallicity relation (Figure 4.5) with the velocity data of Weldrake, de Blok, and Walter (2003, Fig. 4.6), assuming the stellar dispersion is purely radial. Note that this is not the same as the metallicity gradient (see text). This information is included in the summary of Table 4.1.

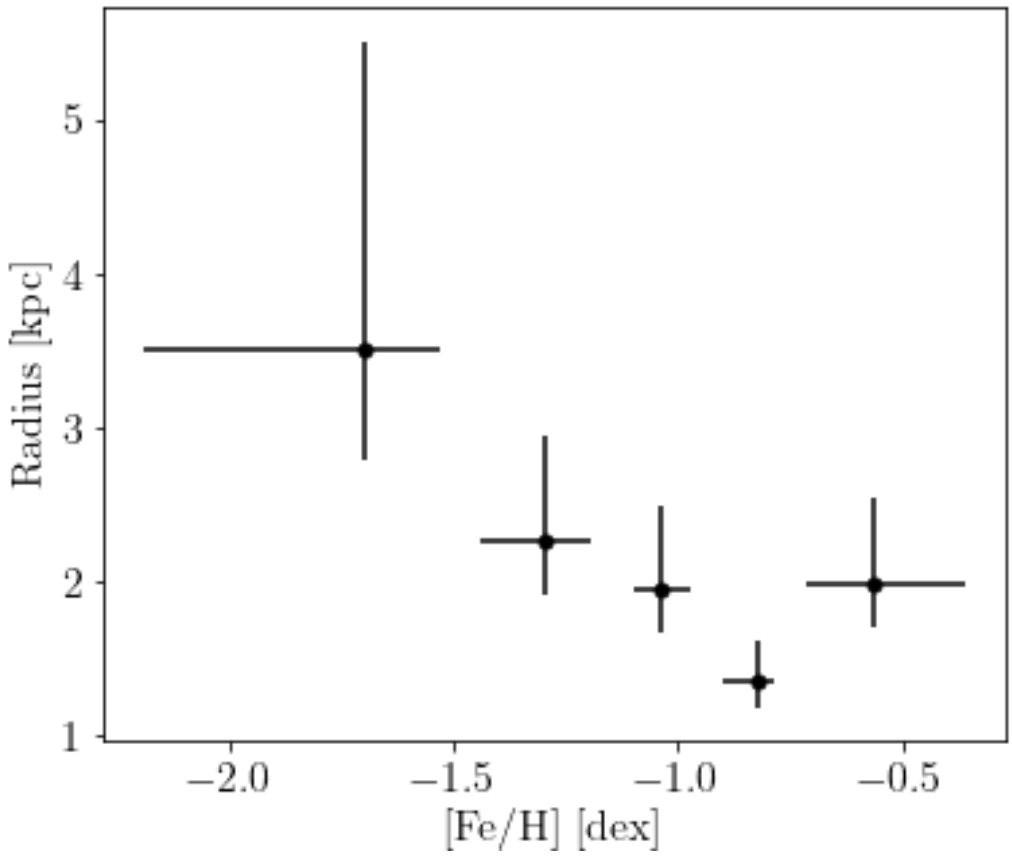

Figure 4.8 Same as figure 4.7 except assuming the stellar dispersion is isotropic. The decreasing velocity curve in H I indicates much further radial distances for metal-poor populations in this case. This information is included in the summary of Table 4.1.

ACKNOWLEDGEMENTS

The authors thank the anonymous referee for their input which improved this paper.

This material is based upon work supported by the National Science Foundation under grant Nos. AST-1636426 and AST-1847909. Evan Kirby gratefully acknowledges support from a Cottrell Scholar award administered by the Research Corporation for Science Advancement as well as funding from generous donors to the California Institute of Technology. Michael Boylan-Kolchin acknowledges support from NSF CAREER award AST-1752913, NSF grant AST-1910346, NASA grant NNX17AG29G, and HST-AR-15006, HST-AR-15809, HST-GO-15658, HST-GO-15901, and HST-GO-15902 from the Space Telescope Science Institute, which is operated by AURA, Inc., under NASA contract NAS5-26555. Support for Coral Wheeler was provided by NASA through the NASA Hubble Fellowship grant HST-HF2-51449.001-A, awarded by the Space Telescope Science Institute, which is operated by the Association of Universities for Research in Astronomy, Inc., for NASA, under contract NAS5-26555.

We are grateful to the many people who have worked to make the Keck Telescope and its instruments a reality and to operate and maintain the Keck Observatory. The authors wish to extend special thanks to those of Hawaiian ancestry on whose sacred mountain we are privileged to be guests. Without their generous hospitality, none of the observations presented herein would have been possible.

Facility: Keck:II (DEIMOS)

[Fe/H] (dex)	Number	v (km/s)	σ (km/s)	K.E./mass $(km/s)^2$	R, $n = 1$ (kpc)	R, $n = 3$ (kpc)
$-1.70^{+0.17}_{-0.49}$	60	3.6 ± 6.4	$30.0^{+3.2}_{-2.6}$	$449n^{+100n}_{-75n}$	$1.3^{+0.3}_{-0.1}$	$3.4^{+1.9}_{-0.7}$
$-1.30^{+0.11}_{-0.14}$	60	5.2 ± 6.7	$24.6^{+2.5}_{-2.3}$	$303n^{+67n}_{-54n}$	$1.0^{+0.2}_{-0.1}$	$2.2^{+0.7}_{-0.3}$
$-1.04^{+0.07}_{-0.06}$	58	$8.3^{+4.7}_{-3.9}$	$22.5^{+2.4}_{-2.1}$	$254n^{+57n}_{-44n}$	$0.95^{+0.18}_{-0.10}$	$1.9^{+0.5}_{-0.3}$
$-0.82^{+0.04}_{-0.08}$	60	$8.9^{+3.9}_{-3.7}$	$17.2^{+1.8}_{-1.6}$	$148n^{+33n}_{-27n}$	$0.75^{+0.15}_{-0.09}$	$1.3^{+0.3}_{-0.2}$
$-0.56^{+0.20}_{-0.15}$	61	$9.3^{+5.0}_{-5.2}$	$22.5^{+2.5}_{-2.1}$	$254n^{+60n}_{-45n}$	$0.97^{+0.21}_{-0.11}$	$2.0^{+0.6}_{-0.3}$

Table 4.1 Table summarizing the stellar binned data in Figures 4.3, 4.4, 4.5, 4.7, and 4.8.

Chapter 5

CONCLUSIONS AND FUTURE WORK

This thesis examines the measurement of focal ratio degradation for fiber positioner systems such as those that will be used for the next generation of fiber-fed multi object spectrographs, with a focus on work done for the Subaru Prime Focus Spectrograph.

Chapter 2 presents work measuring FRD for the Cobra fiber positioner system. The effect of increasing bending and pinching on FRD on a polyimide fiber was tested. With these measurements as a base, the effect of the Cobra fiber positioner system on fiber FRD could be tested. A new illumination apparatus was introduced that allowed for angularly uniform illumination up to a controllable cutoff focal ratio over a small region, allowing for FRD to be tested throughout the patrol region of the Subaru PFS's Cobra fiber positioner without realignment between measurements. Angular misalignments due to the fiber repositioning were extracted using their bimodal two-step drop that uniquely identified it from the more Gaussian-like FRD. We found the Cobra fiber positioner did not induce increased FRD over its patrol region on the fiber indicating low positioning stress, which was reassuring to the Subaru PFS team due to the uncertainties about the stress imposed by the unique piezoelectric-driven theta/phi positioner used in the project. This new apparatus and model similarly has the potential to greatly simplify FRD measurements for upcoming fiber positioners.

While Chapter 2 focuses on measurement of FRD in a test environment, Chapter 3 investigates how FRD manifests in a spectrograph's detector and how to extract FRD from a PSF for modeling purposes. The 2D point spread functions from light focused onto a detector are found to be complicated for signals at low FRD, but in the 20–30 milliradian range that is expected for the fiber routing in the Subaru PFS the 2D point spread function residuals for increasing FRD are found to decrease flux in the center and increase flux toward the outside. This behavior, on top of behaving similarly to how light redistributes in the fiber itself, is regular enough that extraction is feasible. 1D residuals with increasing FRD show the largest fractional effect 3–4 pixels from the center of a line, at between 1–2% of the skyline for a 3 milliradian variation. This finding reaffirms the importance of FRD modeling for data reduction if sky subtraction to the Subaru PFS's goal of 0.5% sky continuum

is to be achieved. Work developing an algorithm to extract FRD is also presented. The algorithm currently can extract FRD to the 2 milliradian level for fibers near the center of the detector.

Chapter 4 focuses on spectroscopic measurements of old red giant branch (RGB) stars in the dwarf irregular galaxy NGC 6822. Given NGC 6822's unique structure and H I hole, its formation history is rather uncertain and quite interesting. In this chapter we noted an additional strange feature apparent in the prolate rotation of the RGB stars in the galaxy. While mergers have been invoked to explain the formation history, the alignment of this rotation with the H I disk of NGC 6822 raises the possibility of other explanations, such as an edge-on bar. While examining this feature, a metallicty gradient of -0.5 kpc/dex was found. Using metallicity as a proxy for age, the metallicity gradient driven by higher dispersion for more metal-poor stars indicated that there may have been a process—possibly burst star formation episodes—that consistently disrupts stars in the center of the galaxy. Nonetheless, there are many unknowns left for this galaxy.

The upcoming Subaru Prime Focus Spectrograph is particularly exciting for answering the questions raised about NGC 6822 in Chapter 4. Fortunately, the Subaru PFS's galactic archaeology strategic plan includes NGC 6822 (Takada et al., 2014), and its wide field-of-view allows for spectra of stars across the galaxy to be collected in a single pointing. The work done in this thesis to quantify FRD will be an important contribution to minimizing noise in the Subaru PFS's spectrographic survey of NGC 6822 among many other projects.

BIBLIOGRAPHY

Allington-Smith, Jeremy et al. (2013). "End effects in optical fibres". In: *Monthly Notices of the Royal Astronomical Society* 436.4, pp. 3492–3499. DOI: 10.1093/mnras/stt1842. eprint: /oup/backfile/content_public/journal/mnras/436/4/10.1093/mnras/stt1842/2/stt1842.pdf. URL: http://dx.doi.org/10.1093/mnras/stt1842.

Angel, J. R. P. et al. (Dec. 1977). "A very large optical telescope array linked with fused silica fibers." In: *Astrophysical Journal* 218, pp. 776–782. DOI: 10.1086/155734.

El-Badry, Kareem, Eliot Quataert, et al. (Jan. 2018). "Gas kinematics, morphology and angular momentum in the FIRE simulations". In: *mnras* 473.2, pp. 1930–1955. DOI: 10.1093/mnras/stx2482. arXiv: 1705.10321 [astro-ph.GA].

El-Badry, Kareem, Andrew Wetzel, et al. (Apr. 2016). "Breathing FIRE: How Stellar Feedback Drives Radial Migration, Rapid Size Fluctuations, and Population Gradients in Low-mass Galaxies". In: *apj* 820.2, 131, p. 131. DOI: 10.3847/0004-637X/820/2/131. arXiv: 1512.01235 [astro-ph.GA].

Bamberg, Eberhard (2006). *Contact Stresses and Deformations*. http://www.mech.utah.edu/~me7960/lectures/Topic7-ContactStressesAndDeformations.pdf.

Barden, Samuel C. (Jan. 1994). "The Use and Benefits of Optical Fibers in Spectroscopy". In: *Optical Astronomy from the Earth and Moon*. Ed. by Diane M. Pyper and Ronald J. Angione. Vol. 55. Astronomical Society of the Pacific Conference Series, pp. 130–138.

– (Jan. 1998). "Review of Fiber-Optic Properties for Astronomical Spectroscopy". In: *Fiber Optics in Astronomy III*. Ed. by S. Arribas, E. Mediavilla, and F. Watson. Vol. 152. Astronomical Society of the Pacific Conference Series, pp. 14–19.

Battinelli, P., S. Demers, and W. E. Kunkel (May 2006). "Photometric survey of the polar ring galaxy NGC 6822". In: *aap* 451.1, pp. 99–108. DOI: 10.1051/0004-6361:20054718. arXiv: astro-ph/0603558 [astro-ph].

Belland, Brent et al. (Jan. 2019). "Focal Ratio Degradation for Fiber Positioner Operation in Astronomical Spectrographs". In: *Journal of Astronomical Instrumentation* 8.3, 1950007, p. 1950007. DOI: 10.1142/S2251171719500077. arXiv: 2006.10902 [astro-ph.IM].

Benítez-Llambay, A. et al. (Feb. 2016). "Mergers and the outside-in formation of dwarf spheroidals". In: *mnras* 456.2, pp. 1185–1194. DOI: 10.1093/mnras/stv2722. arXiv: 1511.06188 [astro-ph.GA].

Bolton, Adam S. and David J. Schlegel (2010). "Spectro-Perfectionism: An Algorithmic Framework for Photon Noise-Limited Extraction of Optical Fiber Spectroscopy". In: *Publications of the Astronomical Society of the Pacific* 122.888, p. 248. URL: http://stacks.iop.org/1538-3873/122/i=888/a=248.

Bunsen, R and G Kirchhoff (1863). "Untersuchungen ueber das Sonnenspektrum und die Spektren der Chemischen Elemente". In: *Abh. kgl. Akad. Wiss*, p. 1861.

Burbidge, E. Margaret et al. (Jan. 1957). "Synthesis of the Elements in Stars". In: *Reviews of Modern Physics* 29.4, pp. 547–650. DOI: 10.1103/RevModPhys.29.547.

Cannon, John M. et al. (Mar. 2012). "On the Origin of the Supergiant H I Shell and Putative Companion in NGC 6822". In: *apj* 747.2, 122, p. 122. DOI: 10.1088/0004-637X/747/2/122. arXiv: 1201.3149 [astro-ph.CO].

Cirasuolo, M. et al. (Sept. 2011). "MOONS: The Multi-Object Optical and Near-infrared Spectrograph". In: *The Messenger* 145, pp. 11–13.

Clayton, C. A. (Apr. 1989). "The implications of image scrambling and focal ratio degradation in fibre optics on the design of astronomical instrumentation". In: *Astronomy and Astrophysics* 213, pp. 502–515.

Dalton, G. et al. (Sept. 2012). "WEAVE: the next generation wide-field spectroscopy facility for the William Herschel Telescope". In: *Ground-based and Airborne Instrumentation for Astronomy IV*. Vol. 8446. procspie, 84460P. DOI: 10.1117/12.925950.

de Blok, W. J. G. and F. Walter (July 2000). "Evidence for Tidal Interaction and a Supergiant H I Shell in the Local Group Dwarf Galaxy NGC 6822". In: *apjl* 537.2, pp. L95–L98. DOI: 10.1086/312777. arXiv: astro-ph/0005473 [astro-ph].

– (Jan. 2006). "The Stellar Population and Interstellar Medium in NGC 6822". In: *aj* 131.1, pp. 343–362. DOI: 10.1086/497829. arXiv: astro-ph/0508018 [astro-ph].

de Jong, R. S. et al. (Sept. 2012). "4MOST: 4-metre multi-object spectroscopic telescope". In: *Ground-based and Airborne Instrumentation for Astronomy IV*. Vol. 8446. procspie, 84460T. DOI: 10.1117/12.926239. arXiv: 1206.6885 [astro-ph.IM].

de Vaucouleurs, Gerard, Antoinette de Vaucouleurs, and Harold G. Corwin (1976). *2nd reference catalogue of bright galaxies containing information on 4364 galaxies with reference to papers published between 1964 and 1975*. University of Texas Press.

dos Santos, J. B. et al. (July 2014). "Studying focal ratio degradation of optical fibers for Subaru's Prime Focus Spectrograph". In: *Advances in Optical and Mechanical Technologies for Telescopes and Instrumentation*. Vol. 9151. procspie, p. 915150. DOI: 10.1117/12.2056460.

Faber, Sandra M. et al. (Mar. 2003). "The DEIMOS spectrograph for the Keck II Telescope: integration and testing". In: *procspie*. Ed. by Masanori Iye and Alan F. M. Moorwood. Vol. 4841. Society of Photo-Optical Instrumentation Engineers (SPIE) Conference Series, pp. 1657–1669. DOI: 10.1117/12.460346.

Feast, Michael W. et al. (Apr. 2012). "The Cepheid distance to the Local Group galaxy NGC 6822". In: *mnras* 421.4, pp. 2998–3003. DOI: 10.1111/j.1365-2966.2012.20525.x. arXiv: 1201.1987 [astro-ph.GA].

Finstad, Daniel et al. (Sept. 2016). "Collimated focal ratio degradation testing for highly multiplexed fiber systems—an improvement to a standard test". In: *Appl. Opt.* 55.25, pp. 6829–6831. DOI: 10.1364/AO.55.006829. URL: http://ao.osa.org/abstract.cfm?URI=ao-55-25-6829.

Fisher, C. et al. (July 2014). "Developing engineering model Cobra fiber positioners for the Subaru Telescope's prime focus spectrometer". In: *Advances in Optical and Mechanical Technologies for Telescopes and Instrumentation*. Vol. 9151. procspie, 91511Y. DOI: 10.1117/12.2054700. arXiv: 1408.2833 [astro-ph.IM].

Flaugher, B. and C. Bebek (July 2014). "The Dark Energy Spectroscopic Instrument (DESI)". In: *Ground-based and Airborne Instrumentation for Astronomy V*. Vol. 9147. procspie, 91470S. DOI: 10.1117/12.2057105.

Fraunhofer, J (1817). *Gilbert's Ann*.

Friedli, D., W. Benz, and R. Kennicutt (Aug. 1994). "On the Influence of Bars and Star Formation on Galactic Abundance Gradients". In: *apjl* 430, p. L105. DOI: 10.1086/187449.

Gallart, C. et al. (Dec. 1996). "The Local Group Dwarf Irregular Galaxy NGC 6822.III. The Recent Star Formation History". In: *aj* 112, p. 2596. DOI: 10.1086/118205.

Gambling, W. A., D. N. Payne, and H. Matsumura (July 1975). "Mode conversion coefficients in optical fibers". In: *Applied Optics* 14, pp. 1538–1542. DOI: 10.1364/AO.14.001538.

Gloge, D. (Oct. 1972). "Optical power flow in multimode fibers". In: *The Bell System Technical Journal* 51.8, pp. 1767–1783. ISSN: 0005-8580. DOI: 10.10012/j.1538-7305.1972.tb02682.x.

Haynes, D. M. et al. (2011). "Relative contributions of scattering, diffraction and modal diffusion to focal ratio degradation in optical fibres". In: *Monthly Notices of the Royal Astronomical Society* 414.1, pp. 253–263. DOI: 10.1111/j.1365-2966.2011.18385.x. eprint: /oup/backfile/content_public/journal/mnras/414/1/10.1111/j.1365-2966.2011.18385.x/2/mnras0414-0253.pdf. URL: +%20http://dx.doi.org/10.1111/j.1365-2966.2011.18385.x.

Hefferon, James E. (1987). *Calculating Bend and Twist Stress in Optical Fibers*. DOI: 10.1117/12.937652. URL: https://doi.org/10.1117/12.937652.

Hill, J. M. (Jan. 1988). "The History of Multiobject Fiber Spectroscopy". In: *Fiber Optics in Astronomy*. Ed. by Samuel C. Barden. Vol. 3. Astronomical Society of the Pacific Conference Series, p. 77.

Hill, J. M. et al. (Dec. 1980). "Multiple object spectroscopy: the medusa spectrograph." In: *Astrophysical Journal Letters* 242, pp. L69–L72. DOI: 10.1086/183405.

Ho, Nhung et al. (Oct. 2012). "Stellar Kinematics of the Andromeda II Dwarf Spheroidal Galaxy". In: *apj* 758.2, 124, p. 124. DOI: 10.1088/0004-637X/758/2/124. arXiv: 1209.2116 [astro-ph.CO].

Hopkins, Philip F. et al. (Nov. 2014). "Galaxies on FIRE (Feedback In Realistic Environments): stellar feedback explains cosmologically inefficient star formation". In: *mnras* 445.1, pp. 581–603. DOI: 10.1093/mnras/stu1738. arXiv: 1311.2073 [astro-ph.CO].

Hubble, E. P. (Dec. 1926). "Extragalactic nebulae." In: *apj* 64, pp. 321–369. DOI: 10.1086/143018.

Hubble, Edwin (Mar. 1929). "A Relation between Distance and Radial Velocity among Extra-Galactic Nebulae". In: *Proceedings of the National Academy of Science* 15.3, pp. 168–173. DOI: 10.1073/pnas.15.3.168.

Hunter, Todd R. and Lawrence W. Ramsey (Dec. 1992). "Scrambling Properties of Optical Fibers and the Performance of a Double Scrambler". In: *Publications of the Astronomical Society of the Pacific* 104, p. 1244. DOI: 10.1086/133115.

Iorio, G. et al. (Apr. 2017). "LITTLE THINGS in 3D: robust determination of the circular velocity of dwarf irregular galaxies". In: *mnras* 466.4, pp. 4159–4192. DOI: 10.1093/mnras/stw3285. arXiv: 1611.03865 [astro-ph.GA].

Kacharov, Nikolay et al. (Apr. 2017). "Prolate rotation and metallicity gradient in the transforming dwarf galaxy Phoenix". In: *mnras* 466.2, pp. 2006–2023. DOI: 10.1093/mnras/stw3188. arXiv: 1612.01560 [astro-ph.GA].

Kaufmann, Tobias, Coral Wheeler, and James S. Bullock (Dec. 2007). "On the morphologies, gas fractions, and star formation rates of small galaxies". In: *mnras* 382.3, pp. 1187–1195. DOI: 10.1111/j.1365-2966.2007.12436.x. arXiv: 0706.0210 [astro-ph].

Kawata, Daisuke et al. (Apr. 2006). "Origin of Two Distinct Populations in Dwarf Spheroidal Galaxies". In: *apj* 641.2, pp. 785–794. DOI: 10.1086/500633. arXiv: astro-ph/0509402 [astro-ph].

Kirby, Evan N., James S. Bullock, et al. (Mar. 2014). "The dynamics of isolated Local Group galaxies". In: *mnras* 439.1, pp. 1015–1027. DOI: 10.1093/mnras/stu025. arXiv: 1401.1208 [astro-ph.GA].

Kirby, Evan N., Judith G. Cohen, et al. (Dec. 2013). "The Universal Stellar Mass-Stellar Metallicity Relation for Dwarf Galaxies". In: *apj* 779.2, 102, p. 102. DOI: 10.1088/0004-637X/779/2/102. arXiv: 1310.0814 [astro-ph.GA].

Kirby, Evan N., Gustavo A. Lanfranchi, et al. (Feb. 2011). "Multi-element Abundance Measurements from Medium-resolution Spectra. III. Metallicity Distributions of Milky Way Dwarf Satellite Galaxies". In: *Astrophysical Journal* 727.2, 78, p. 78. DOI: 10.1088/0004-637X/727/2/78. arXiv: 1011.4937 [astro-ph.GA].

Komiyama, Yutaka et al. (June 2003). "Discovery of Latent Star Formation in the Extended H I Gas around the Local Group Dwarf Irregular Galaxy NGC 6822". In: *apjl* 590.1, pp. L17–L20. DOI: 10.1086/376551.

Leaman, Ryan et al. (Dec. 2017). "A unified model for age-velocity dispersion relations in Local Group galaxies: disentangling ISM turbulence and latent dynamical heating". In: *mnras* 472.2, pp. 1879–1896. DOI: 10.1093/mnras/stx2014. arXiv: 1710.01317 [astro-ph.GA].

Lesser, Michael (Nov. 2015). "A Summary of Charge-Coupled Devices for Astronomy". In: *Publications of the Astronomical Society of the Pacific* 127.957, p. 1097. DOI: 10.1086/684054.

Letarte, Bruno et al. (Feb. 2002). "The Extent of NGC 6822 Revealed by Its C Star Population". In: *aj* 123.2, pp. 832–839. DOI: 10.1086/338319. arXiv: astro-ph/0110026 [astro-ph].

Lewis, I. J. et al. (June 2002). "The Anglo-Australian Observatory 2dF facility". In: *mnras* 333, pp. 279–299. DOI: 10.1046/j.1365-8711.2002.05333.x. eprint: astro-ph/0202175.

Lissandrini, C., S. Cristiani, and F. La Franca (Nov. 1994). "Sky Subtraction with Fiber-Spectrographs". In: *Publications of the Astronomical Society of the Pacific* 106, p. 1157. DOI: 10.1086/133493. arXiv: astro-ph/9408085 [astro-ph].

Loebman, Sarah R. et al. (Feb. 2016). "Imprints of Radial Migration on the Milky Way's Metallicity Distribution Functions". In: *apjl* 818.1, L6, p. L6. DOI: 10.3847/2041-8205/818/1/L6. arXiv: 1511.06369 [astro-ph.GA].

Lupton, Robert (2021). "2D-DRP + Processing of data from SM1 and SuNSS". In: PFS 12th collaboration meeting (Mar. 9–10, 2021).

Mashchenko, Sergey, James Wadsley, and H. M. P. Couchman (Jan. 2008). "Stellar Feedback in Dwarf Galaxy Formation". In: *Science* 319.5860, p. 174. DOI: 10.1126/science.1148666. arXiv: 0711.4803 [astro-ph].

Massey, Philip and Margaret M. Hanson (2013). "Astronomical Spectroscopy". In: *Planets, Stars and Stellar Systems. Volume 2: Astronomical Techniques, Software and Data*. Ed. by Terry D. Oswalt and Howard E. Bond, p. 35. DOI: 10.1007/978-94-007-5618-2_2.

Massey, Philip, K. A. G. Olsen, et al. (May 2007). "A Survey of Local Group Galaxies Currently Forming Stars. II. UBVRI Photometry of Stars in Seven Dwarfs and a Comparison of the Entire Sample". In: *aj* 133.5, pp. 2393–2417. DOI: 10.1086/513319. arXiv: astro-ph/0702236 [astro-ph].

Mayer, Lucio et al. (Oct. 2001). "The Metamorphosis of Tidally Stirred Dwarf Galaxies". In: *apj* 559.2, pp. 754–784. DOI: 10.1086/322356. arXiv: astro-ph/0103430 [astro-ph].

McConnachie, Alan W. (July 2012). "The Observed Properties of Dwarf Galaxies in and around the Local Group". In: *aj* 144.1, 4, p. 4. DOI: 10.1088/0004-6256/144/1/4. arXiv: 1204.1562 [astro-ph.CO].

Meyers, Josh (2018). *DMTN-064: Hyper Suprime-Cam donut analysis*. https://dmtn-064.lsst.io.

Miyazaki, Satoshi et al. (Sept. 2012). "Hyper Suprime-Cam". In: *Ground-based and Airborne Instrumentation for Astronomy IV*. Ed. by Ian S. McLean, Suzanne K. Ramsay, and Hideki Takami. Vol. 8446. Society of Photo-Optical Instrumentation Engineers (SPIE) Conference Series, 84460Z. DOI: 10.1117/12.926844.

Murphy, J. D. et al. (July 2008). "Focal ratio degradation and transmission in VIRUS-P optical fibers". In: *Advanced Optical and Mechanical Technologies in Telescopes and Instrumentation*. Vol. 7018. procspie, 70182T. DOI: 10.1117/12.788411.

Navarro, Julio F., Carlos S. Frenk, and Simon D. M. White (May 1996). "The Structure of Cold Dark Matter Halos". In: *apj* 462, p. 563. DOI: 10.1086/177173. arXiv: astro-ph/9508025 [astro-ph].

– (Dec. 1997). "A Universal Density Profile from Hierarchical Clustering". In: *apj* 490.2, pp. 493–508. DOI: 10.1086/304888. arXiv: astro-ph/9611107 [astro-ph].

Oliveira, A. C., L. S. de Oliveira, and J. B. dos Santos (Jan. 2005). "Studying focal ratio degradation of optical fibres with a core size of 50 μm for astronomy". In: *mnras* 356, pp. 1079–1087. DOI: 10.1111/j.1365-2966.2004.08536.x.

Pérez, I., P. Sánchez-Blázquez, and A. Zurita (Mar. 2009). "Study of the stellar line-strength indices and kinematics along bars. I. Bar age and metallicity gradients". In: *aap* 495.3, pp. 775–794. DOI: 10.1051/0004-6361:200811084. arXiv: 0812.2586 [astro-ph].

Perlmutter, S. et al. (June 1999). "Measurements of Ω and Λ from 42 High-Redshift Supernovae". In: *Astrophysical Journal* 517.2, pp. 565–586. DOI: 10.1086/307221. arXiv: astro-ph/9812133 [astro-ph].

Poppett, C. L. and J. R. Allington-Smith (July 2007). "Fibre systems for future astronomy: anomalous wavelength-temperature effects". In: *Monthly Notices of the Royal Astronomical Society* 379, pp. 143–150. DOI: 10.1111/j.1365-2966.2007.11922.x.

Poppett, Claire et al. (July 2018). "The DESI fiber system". In: *Ground-based and Airborne Instrumentation for Astronomy VII*. Ed. by Christopher J. Evans, Luc Simard, and Hideki Takami. Vol. 10702. Society of Photo-Optical Instrumentation Engineers (SPIE) Conference Series, 107027O. DOI: 10.1117/12.2312176.

Poppett, Claire L. et al. (Aug. 2014). "Focal ratio degradation performance of fiber positioning technology used in the Dark Energy Spectroscopic Instrument (DESI)". In: *Ground-based and Airborne Instrumentation for Astronomy V*. Ed. by Suzanne K. Ramsay, Ian S. McLean, and Hideki Takami. Vol. 9147. Society of Photo-Optical Instrumentation Engineers (SPIE) Conference Series, p. 914763. DOI: 10.1117/12.2054454.

Postman, M. and M. J. Geller (June 1984). "The morphology-density relation - The group connection." In: *apj* 281, pp. 95–99. DOI: 10.1086/162078.

Racine, René (Jan. 2004). "The Historical Growth of Telescope Aperture". In: *Publications of the Astronomical Society of the Pacific* 116.815, pp. 77–83. DOI: 10.1086/380955.

Ramsey, L. W. (1988). "Focal ratio degradation in optical fibers of astronomical interest". In: *Fiber Optics in Astronomy*. Ed. by S. C. Barden. Vol. 3. Astronomical Society of the Pacific Conference Series, pp. 26–39.

Rubin, Vera C. and Jr. Ford W. Kent (Feb. 1970). "Rotation of the Andromeda Nebula from a Spectroscopic Survey of Emission Regions". In: *Astrophysical Journal* 159, p. 379. DOI: 10.1086/150317.

Sandage, Allan (Sept. 2005). "The Classification of Galaxies: Early History and Ongoing Developments". In: *araa* 43.1, pp. 581–624. DOI: 10.1146/annurev.astro.43.112904.104839.

Schmidt, Brian P. et al. (Nov. 1998). "The High-Z Supernova Search: Measuring Cosmic Deceleration and Global Curvature of the Universe Using Type IA Supernovae". In: *Astrophysical Journal* 507.1, pp. 46–63. DOI: 10.1086/306308. arXiv: astro-ph/9805200 [astro-ph].

Smee, S. A. et al. (Aug. 2013). "The Multi-object, Fiber-fed Spectrographs for the Sloan Digital Sky Survey and the Baryon Oscillation Spectroscopic Survey". In: *The Astronomical Journal* 146, 32, p. 32. DOI: 10.1088/0004-6256/146/2/32. arXiv: 1208.2233 [astro-ph.IM].

Spekkens, Kristine et al. (Nov. 2014). "The Dearth of Neutral Hydrogen in Galactic Dwarf Spheroidal Galaxies". In: *apjl* 795.1, L5, p. L5. DOI: 10.1088/2041-8205/795/1/L5. arXiv: 1410.0028 [astro-ph.GA].

Sugai, H. et al. (July 2015). "Prime Focus Spectrograph for the Subaru telescope: massively multiplexed optical and near-infrared fiber spectrograph". In: *Journal of Astronomical Telescopes, Instruments, and Systems* 1.3, 035001, p. 035001. DOI: 10.1117/1.JATIS.1.3.035001. arXiv: 1507.00725 [astro-ph.IM].

Swan, J. et al. (Mar. 2016). "Ca II triplet spectroscopy of RGB stars in NGC 6822: kinematics and metallicities". In: *mnras* 456.4, pp. 4315–4327. DOI: 10.1093/mnras/stv2774. arXiv: 1602.01897 [astro-ph.GA].

Takada, Masahiro et al. (2014). "Extragalactic science, cosmology, and Galactic archaeology with the Subaru Prime Focus Spectrograph". In: *Publications of the Astronomical Society of Japan* 66.1, R1. DOI: 10.1093/pasj/pst019. eprint: /oup/backfile/content_public/journal/pasj/66/1/10.1093/pasj/pst019/2/pst019.pdf. URL: +%20http://dx.doi.org/10.1093/pasj/pst019.

Tamura, N. et al. (Aug. 2016). "Prime Focus Spectrograph (PFS) for the Subaru telescope: overview, recent progress, and future perspectives". In: *Ground-based and Airborne Instrumentation for Astronomy VI*. Vol. 9908. procspie, p. 99081M. DOI: 10.1117/12.2232103. arXiv: 1608.01075 [astro-ph.IM].

Thompson, Graham P., Sean G. Ryan, and Lisette F. Sibbons (Nov. 2016). "The rotation of the halo of NGC 6822 from the radial velocities of carbon stars". In: *mnras* 462.3, pp. 3376–3385. DOI: 10.1093/mnras/stw1193. arXiv: 1605.05582 [astro-ph.GA].

Valenzuela, Octavio et al. (Mar. 2007). "Is There Evidence for Flat Cores in the Halos of Dwarf Galaxies? The Case of NGC 3109 and NGC 6822". In: *apj* 657.2, pp. 773–789. DOI: 10.1086/508674. arXiv: astro-ph/0509644 [astro-ph].

Walker, Matthew G. and Jorge Peñarrubia (Nov. 2011). "A Method for Measuring (Slopes of) the Mass Profiles of Dwarf Spheroidal Galaxies". In: *apj* 742.1, 20, p. 20. DOI: 10.1088/0004-637X/742/1/20. arXiv: 1108.2404 [astro-ph.CO].

Weisz, Daniel R. et al. (July 2014). "The Star Formation Histories of Local Group Dwarf Galaxies. I. Hubble Space Telescope/Wide Field Planetary Camera 2 Observations". In: *apj* 789.2, 147, p. 147. DOI: 10.1088/0004-637X/789/2/147. arXiv: 1404.7144 [astro-ph.GA].

Weldrake, D. T. F., W. J. G. de Blok, and F. Walter (Mar. 2003). "A high-resolution rotation curve of NGC 6822: a test-case for cold dark matter". In: *mnras* 340.1, pp. 12–28. DOI: 10.1046/j.1365-8711.2003.06170.x. arXiv: astro-ph/0210568 [astro-ph].

Wheeler, Coral et al. (Feb. 2017). "The no-spin zone: rotation versus dispersion support in observed and simulated dwarf galaxies". In: *mnras* 465.2, pp. 2420–2431. DOI: 10.1093/mnras/stw2583. arXiv: 1511.01095 [astro-ph.GA].

Wolf, Joe et al. (Aug. 2010). "Accurate masses for dispersion-supported galaxies". In: *mnras* 406.2, pp. 1220–1237. DOI: 10.1111/j.1365-2966.2010.16753.x. arXiv: 0908.2995 [astro-ph.CO].

Wyder, Ted K. (Nov. 2001). "The Star Formation History of NGC 6822". In: *aj* 122.5, pp. 2490–2523. DOI: 10.1086/323706. arXiv: astro-ph/0107603 [astro-ph].

Yan, Yunxiang et al. (2018). “DEEM, a versatile platform of FRD measurement for highly multiplexed fibre systems in astronomy”. In: *Monthly Notices of the Royal Astronomical Society* 476.4, pp. 4279–4314. DOI: 10.1093/mnras/sty461. eprint: /oup/backfile/content_public/journal/mnras/476/4/10.1093_mnras_sty461/1/sty461.pdf. URL: http://dx.doi.org/10.1093/mnras/sty461.

Zhuang, Yulong et al. (Feb. 2019). “A dynamical view on stellar metallicity gradient diversity across the Hubble sequence with CALIFA”. In: *mnras* 483.2, pp. 1862–1880. DOI: 10.1093/mnras/sty2916. arXiv: 1810.12223 [astro-ph.GA].

Zwicky, F. (Jan. 1933). “Die Rotverschiebung von extragalaktischen Nebeln”. In: *Helvetica Physica Acta* 6, pp. 110–127.